eScience 5 (2025) 100333

Contents lists available at ScienceDirect

eScience

journal homepage: www.keaipublishing.com/en/journals/escience

Review

# Advancements in electrochemical synthesis: Expanding from water electrolysis to dual-value-added products

Genxiang Wang [a,b], Ao Chen [b,e], Yao Chen [b,e], Fen Qiao [a], Junfeng Wang [a], Nianjun Yang [c,*], Hao Zhang [d,*], Zhenhai Wen [b,*]

[a] School of Energy and Power Engineering, Jiangsu University, Zhenjiang 212013, China
[b] CAS Key Laboratory of Design and Assembly of Functional Nanostructures, and Fujian Provincial Key Laboratory of Materials and Techniques Toward Hydrogen Energy, Fujian Institute of Research on the Structure of Matter, Chinese Academy of Sciences, Fuzhou 350002, China
[c] Department of Chemistry & IMO-IMOMEC, Hasselt University, Diepenbeek 3590, Belgium
[d] Department of Chemical Engineering, Massachusetts Institute of Technology, Cambridge, MA 02139, USA
[e] University of Chinese Academy of Science, Beijing 100049, China

## HIGHLIGHTS

- The electrochemical hybrid systems pairing value-added OER alternatives with reduction reactions beyond HER are reviewed.
- The catalytic mechanism of developed catalysts and electrochemical performance of these systems are particularly analyzed.
- The challenges encountered by these integrated electrochemical systems and a perspective on future directions are delineated.

## GRAPHICAL ABSTRACT

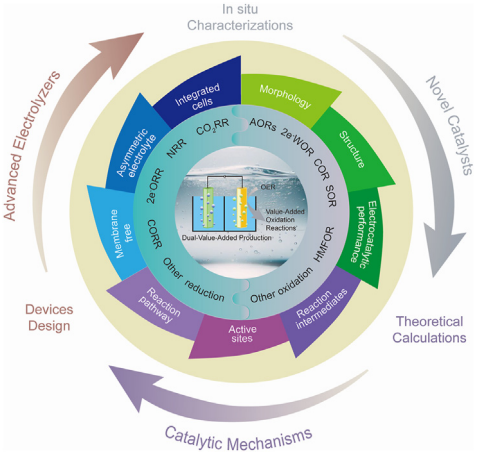


## ARTICLE INFO

*Keywords:*
Electrosynthesis
Electrochemical hybrid systems
Oxygen evolution reaction alternatives
Reduction reactions

## ABSTRACT

The application of electrochemical technologies for chemical and fuel synthesis offers a significantly more eco-friendly method than traditional industrial practice. However, electrochemical synthesis in aqueous solutions often involves a sluggish oxygen evolution reaction (OER) at the anode, yielding products that are less economically viable and leading to inefficient energy use. This challenge has prompted extensive research into replacing the OER with fast, value-added oxidation reactions (OER alternatives) in electrolysis systems. In this review, we summarize the latest research progress in coupled electrochemical systems that integrate OER alternatives with reduction reactions, beyond hydrogen evolution reactions, in aqueous solutions to synthesize dual value-added products. After providing a general overview, we start by introducing two key factors: (i) electrolytic

* Corresponding authors.
*E-mail addresses:* nianjun.yang@uhasselt.be (N. Yang), hzhchem@mit.edu (H. Zhang), wen@fjirsm.ac.cn (Z. Wen).
Peer review under the responsibility of Editorial Board of eScience.

https://doi.org/10.1016/j.esci.2024.100333
Received 25 June 2024; Received in revised form 12 September 2024; Accepted 7 November 2024
Available online 16 November 2024

devices and (ii) advanced characterization techniques for mechanism investigation. The focus then shifts to catalysts developed so far and their corresponding catalytic mechanisms, and to the electrochemical performance of these hybrid electrolysis systems. Finally, we outline and discuss the challenges and prospects for these integrated electrochemical systems to offer insights into future research directions and applications. We envision that this review will provide a panorama of electrolysis systems for dual value-added products, thereby fostering the development of green synthesis with zero carbon emissions.

## 1. Introduction

For nearly two centuries, fossil fuels have been the dominant source of primary energy consumption around the world, accounting for over 80% of the total consumed energy (Fig. 1a). The fossil fuel-based chemical industry plays a crucial role in the large-scale production of fuels, chemicals, pharmaceuticals, and more [1,2]. However, substantial dependence on fossil fuels has brought about significant challenges in the form of energy and environmental crises, exacerbated by a rapid rise in $CO_2$ emissions, which have seen an increase of more than 40% over the past two decades. This situation necessitates the urgent development of low-carbon, green production methods that align with achieving the "net-zero" goal. As investment in clean energy surges, rising from $1.07 trillion in 2015 to $1.74 trillion in 2023, and the availability of electricity from renewable sources grows, increasing from 0.72% in 2000 to 7.48% in 2022 (Figs. 1b and c), [2–4], electrochemistry powered by renewable energy has sparked sustained interest and gained prominence as a favored method for synthesizing chemicals and fuels [1,5].

Electrochemical synthesis is a process in which electricity drives chemical reactions to obtain specific desired products. Its history can be traced back to the early 1800s when Sir Humphry Davy discovered electrolysis, laying the foundation for electrochemical synthesis (Fig. 2) [6]. Throughout the 20th century, electrochemical synthesis has made significant progress and received widespread attention [5,7]. A notable breakthrough was the development of the chlor-alkali process in the late 19th century, which enabled the large-scale production of chlorine, sodium hydroxide, and hydrogen through the electrolysis of saltwater [8]. In recent decades, electrochemical synthesis has experienced a boom in research investment due to its potential for sustainable, green chemistry, resulting in a large number of scientific discoveries, technological advances, and the development of more sustainable chemical processes [9–11].

Among these processes, the electrochemical conversion of several abundant molecules and compounds (e.g., $H_2O$, $O_2$, $CO_2$, $N_2$, nitrates, as well as other organics and inorganics) into valuable chemical feedstocks in aqueous solutions offers prominent advantages, including mild reaction conditions, rich raw materials, feasible large-scale production, and green renewability. This aligns perfectly with the global emphasis on sustainable practices and the urgent need to reduce carbon emissions [11–15]. In an aqueous solution, the oxygen evolution reaction (OER), with a thermodynamic equilibrium potential of 1.23 $V_{RHE}$ (vs. the reversible hydrogen electrode (RHE)), is commonly paired with the aforementioned reduction reactions in these electrochemical conversion systems as the anode reaction. However, the OER process has problems, such as its sluggish kinetics and the low economic value of oxidative products, which greatly reduce electrolysis efficiency and economic benefits [16]. To address these issues, it has been suggested that the OER be replaced with thermodynamically and kinetically favorable oxidation

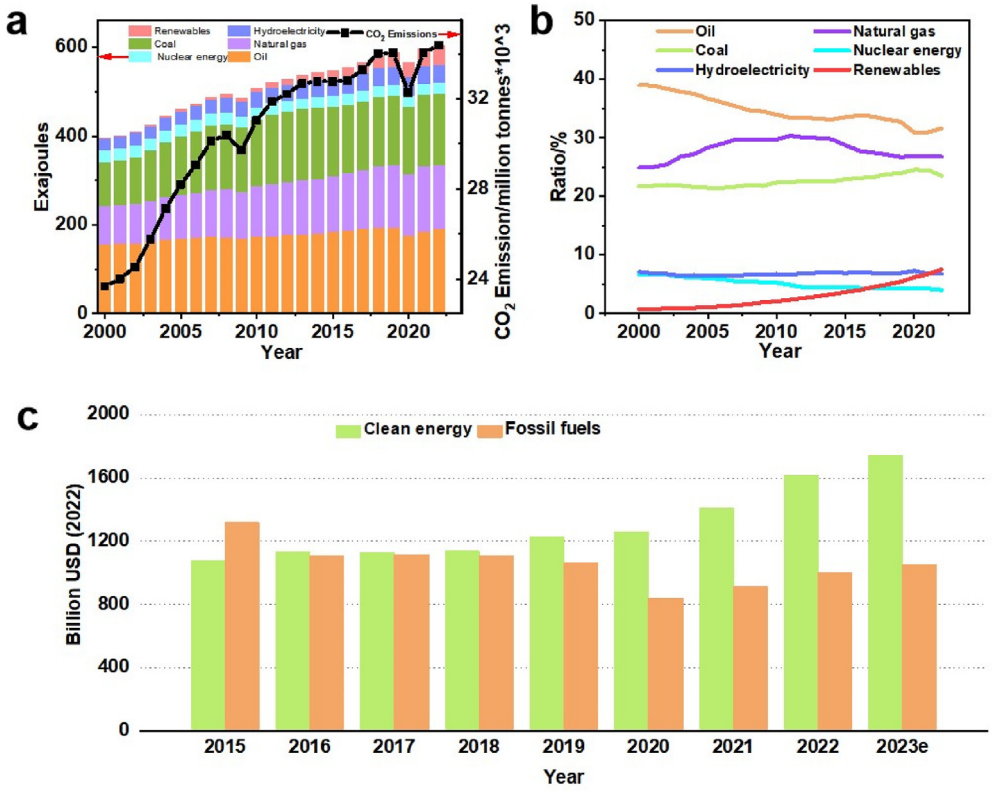


**Fig. 1.** World primary energy consumption and $CO_2$ emissions (a) and the shares of global primary energy by years (b). The data were obtained from the International Renewable Energy Agency [2]. (c) Global energy investment in clean energy and fossil fuels by years (IEA, 2023); 2023e = estimated values for 2023 [4].

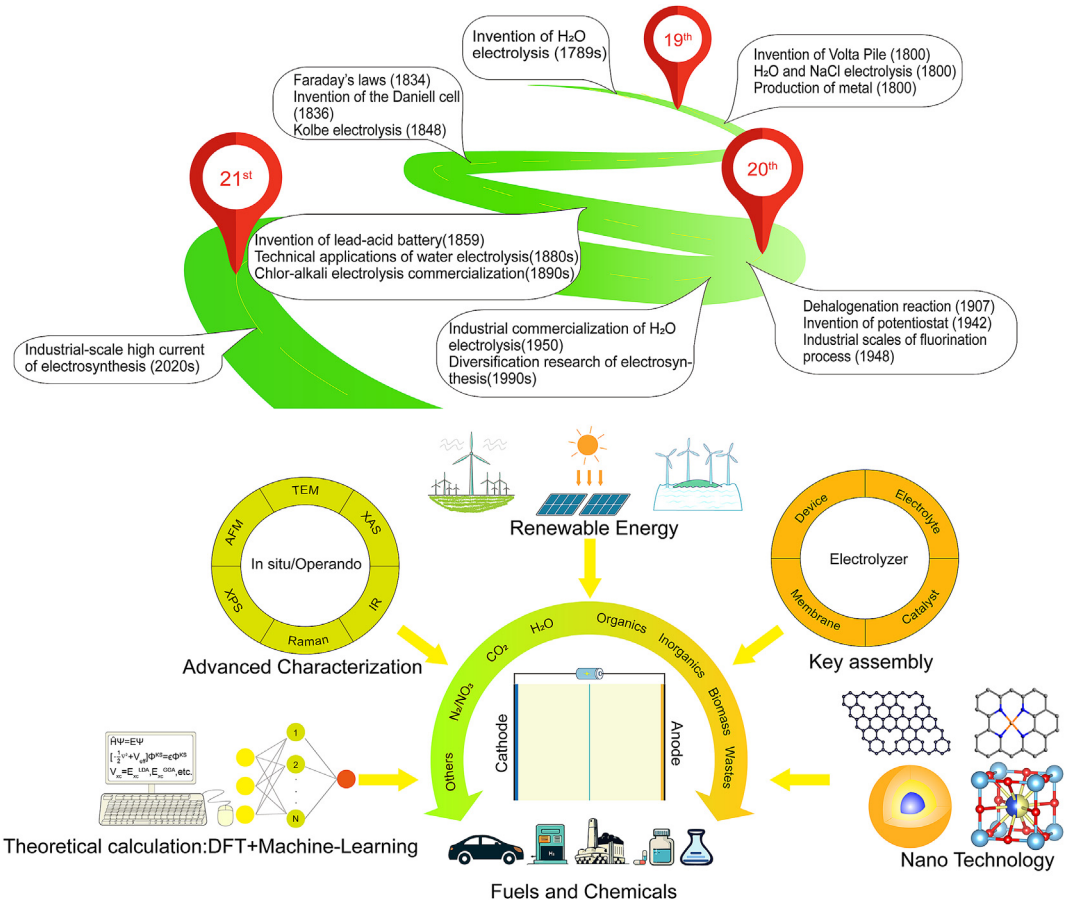


**Fig. 2.** The history of electrosynthesis is marked by these important milestones and the development of methods for electrochemically converting energetic molecules into value-added products.

reactions. Such alternatives typically have more negative oxidation potentials and yield more valuable oxidation products, or they are ecologically beneficial [17]. The generally used OER alternatives include inorganic synthesis, organic synthesis, waste reforming, and other reactions according to the functional classification of substitutes (Table 1) [18–26]. The addition of these alternative reactions not only greatly reduces the power consumption during overall electrolysis but also promotes the formation of cathode products and upgrades the anode reaction.

Among the recently published work on electrosynthesis assisted by OER alternatives, the coupling of OER alternatives in water splitting for $H_2$ production remains the most advanced, especially in the past three years. This progress is mainly driven by two crucial factors. On the one hand, as highlighted in the International Energy Agency's Global Hydrogen Review, hydrogen serves as a clean fuel and raw material in industrial production and daily life, playing a key role in decarbonizing the energy system; however, over 95% of the hydrogen consumed for industrial refinement, ammonia production, methanol production, and iron and steel manufacturing is produced from fossil fuels owing to the significantly lower production cost compared with water electrolysis (Fig. 3) [27,28]. Thus, it is essential to develop clean hydrogen production and enhance its cost competitiveness quickly, to increase the proportion of green hydrogen (produced using renewable energy sources through water electrolysis) relative to brown hydrogen (derived from coal gasification), grey hydrogen (produced by steam methane reforming of natural gas), and blue hydrogen (which follows the same production pathway as grey hydrogen but incorporates a $CO_2$ capture step using carbon capture and storage technologies) [28]. On the other hand, extensive study of the traditional water splitting method has elucidated the reaction mechanisms and defined the reaction products at the cathode, and experimental techniques to study these hybrid systems are now widely available [18,21,29–33]. Statistical analysis of hybrid water electrolysis studies indicates that the most attention has been focused on oxidation reactions with explicit products and ultralow potential, such as the oxidation of urea, hydrazine, methanol, and sodium borohydride/amine borane (Fig. 4) [23,34–36]. Notably, these processes, which yield value-added products, are particularly sought-after because they are more economical than processes that produce carbon dioxide or nitrogen, although more complex analytical and separation procedures are required. Among the coupling electrolysis systems thus far constructed, great attention has been paid to exploring catalysts and reaction mechanisms in various electrolytes and optimized electrolyzers, and exploring new OER alternatives to optimize the performance of electrochemical hydrogen production systems [9,18,31,37–41]. Nanomaterial synthesis technology has made available many cost-effective and active catalysts in powdered and self-supporting forms for the cathodic hydrogen evolution reaction (HER) and anodic OER alternatives [18,21]. Advanced theoretical calculations along with *in situ* and *operando* electrochemical characterization techniques enable the precise determination of reaction pathways and active sites [38,42]. In addition, hybrid electrolyzer designs now typically include both single and dual chambers, catering to the specific requirements of the electrolytes on both sides and their associated oxidation reactions [23,43,44]. Notably, the dual-chamber design has evolved from H-type cells to flow cells over the past three years, significantly improving the current density [17,38]. Among these key factors, electrocatalysts consistently occupy a central position in research aimed at improving conversion efficiency, especially OER alternatives [23,29,31]. The production of widely studied OER alternatives in water electrolysis for hydrogen production provides valuable

**Table 1**
List of the commonly used OER alternatives.

| Species | Reactant | Oxide products | Potential (V vs. SHE) | Advantages as OER alternatives |
|---|---|---|---|---|
| Inorganic synthesis | $Cl^-$ | $Cl_2/ClO^-$ | 1.36 | Diversifies the application of the chlor-alkali process |
| | $I^-$ | $I_2$ | 0.54 | Low oxidation potential, valuable $I_2$, and concomitant NaOH |
| | $H_2O$ | $H_2O_2$ | 1.78 | Highly valuable products, green synthesis method, high sustainability |
| Organic synthesis | Methanol | Formic acid | −0.258 | Value-added product, abundant raw materials, far lower oxidation potential, and green synthesis |
| | Ethanol | Acetic acid | −0.334 | |
| | Isopropanol | Acetone | 0.054 | |
| | Glycerol | Glyceraldehyde | 0.35 | |
| | | Dihydroxyacetone | 0.33 | |
| | | Formic acid | 0.276 | |
| | | Lactic acid | 0.041 | |
| | Benzyl alcohol | Benzyl acid | 0.48 $V_{RHE}$ | |
| | Glucose | Gluconic acid | 0.05 $V_{RHE}$ | |
| | Ethylene glycol | Oxalic acid | −0.455 | |
| | | Formic acid | / | |
| | | Glycolic acid | −0.334 | |
| | HMF | FDCA | −0.78 | |
| | Furfural | 2-Furoic acid | −1.27 | |
| | Formaldehyde | Formate and $H_2$ | −0.224 $V_{RHE}$ | |
| | Ascorbic acid | Dehydroascorbic acid | 0.48 $V_{RHE}$ | |
| Waste reforming | Urea | $N_2$+$CO_2$ | −0.46 | Low oxidation potential, pollution mitigation, and value-added product recycling |
| | Hydrazine | $N_2$+$H_2O$ | −1.16 | |
| | $SO_3^{2-}$ | $SO_4^{2-}$ | 0.10 | |
| | $S^{2-}$ | S | −0.48 | |
| Others | $NH_3$ | $N_2$ | 0.06 $V_{RHE}$ | Ultralow oxidation potential |
| | $NaBH_4$ | $NaBO_2$ | −1.24 | |
| | $NH_3BH_3$ | $NH_4BO_2$ | −1.216 | |

insights into the selection of anode catalysts and the design of electrolyzers for other electrolysis systems.

Inspired by hybrid water electrolysis, a plethora of alternative electrolysis systems have been developed, such as the two-electron oxygen reduction reaction (2e⁻ORR), the $CO_2$ reduction reaction ($CO_2$RR), the CO reduction reaction (CORR), the $N_2$ and nitrate reduction reaction (NRR), and various organic reduction reactions. This surge has been fueled by advancements in innovative catalyst development, the exploration of catalytic mechanisms using sophisticated *in situ* characterization techniques and theoretical calculation methods, and the meticulous optimization of electrolysis apparatuses [45–49].

As research into electrosynthesis with OER alternatives continues to develop, a timely review of newly developed electrolytic earth-abundant molecules assisted by OER alternatives for energy-efficient electrosynthesis is crucial for researchers to stay abreast of the cutting-edge developments in this field. As a series of reviews have extensively summarized OER alternatives for assisting hydrogen production [18,21,29,31–33,39], this review mainly focuses on outlining recent achievements in the electrosynthesis of dual value-added chemicals beyond $H_2$ production. Specifically, we start with an overview of the key factors for electrochemical synthesis devices evolved from water-splitting reactors. Then we review the development of advanced characterization techniques for investigating reaction mechanisms to deepen our understanding of electrolysis modes and reaction processes. Subsequently, we focus on electrolytically rich chemicals (e.g., $O_2$, $CO_2$, CO, $N_2$, nitrate, and some organics), assisted by alternative oxygen reactions in aqueous media. To provide greater specificity, the progression of these integrated electrolysis systems for OER alternatives will be classified based on cathodic reactions, namely the $CO_2$RR, CORR, 2e⁻ORR, NRR, and other reduction reactions. Our goal is to impart a comprehensive understanding of how the optimization of electrosynthesis systems is pursued, with particular attention given to an analysis of the catalysts developed, the relationship between structure and performance based on theoretical calculations and *in situ* characterizations, and the overall performance of the proposed electrolysis system, aiming to provide guidance for constructing electrolysis systems in terms of catalyst design and device optimization. Finally, we will summarize the challenges encountered by these integrated electrochemical systems and share some forward-looking insights into the future development of electrochemical synthesis reactions through the use of pairing reactions, electrocatalysts, electrolysis devices, and other possibilities.

## 2. The key factors for electrolytic synthesis devices

The electrochemical performance of the coupling system relies primarily on three key components: the catalyst electrode, the electrolyte, and the electrolyzer. Catalyst electrodes hold a longstanding prominence in electrolytic synthesis because they reduce the activation energy necessary for specific reactions. By offering an alternative reaction pathway demanding less energy, these electrodes expedite reactions while minimizing energy consumption. The choice of components and the structure of the catalyst materials is contingent upon the species of catalytic reaction, as different catalysts have distinct affinities for specific reactions [48,50]. The advent of nanotechnology has revolutionized the preparation of numerous nanocatalysts via alloying, decorating, doping, anchoring, shaping, introducing defects, constructing core–shell structures, and so on, all of which have propelled great improvements in the performance of electrolysis reactions [38,49,51–53]. Catalyst electrodes generally encompass the catalyst-supported electrode, self-supported electrode, and gas diffusion variants when classified by the electrode structure and the combination of current collector and active component. Catalyst-supported electrodes typically entail the application of powdery nanocatalysts onto current collectors, aided by polymeric binders that may have limited active sites, large resistance, and electrode instability. Conversely, self-supported electrodes involve the *in situ* growth of catalysts on diverse current collectors with more active constituents. This method streamlines electrode preparation, curtails expenses, and generally yields swifter reaction rates, heightened electrochemical activity, and superior stability compared to catalyst-supported electrodes. Consequently, a significant surge in the development of self-supported electrodes for various electrocatalytic reactions has ensued in recent years, markedly enhancing the performance of electrolysis systems [54,55]. Gas-diffusion electrodes (GDEs), which are essential for reactions involving gas reactants, play a pivotal role in achieving rapid conversion. GDEs facilitate the construction of the gas–liquid–solid three-phase interface that is crucial for catalytic reactions, efficiently addressing the mass transport limitation caused by low gas solubility and significantly enhancing the reaction rate. In the $CO_2$RR and CORR, the

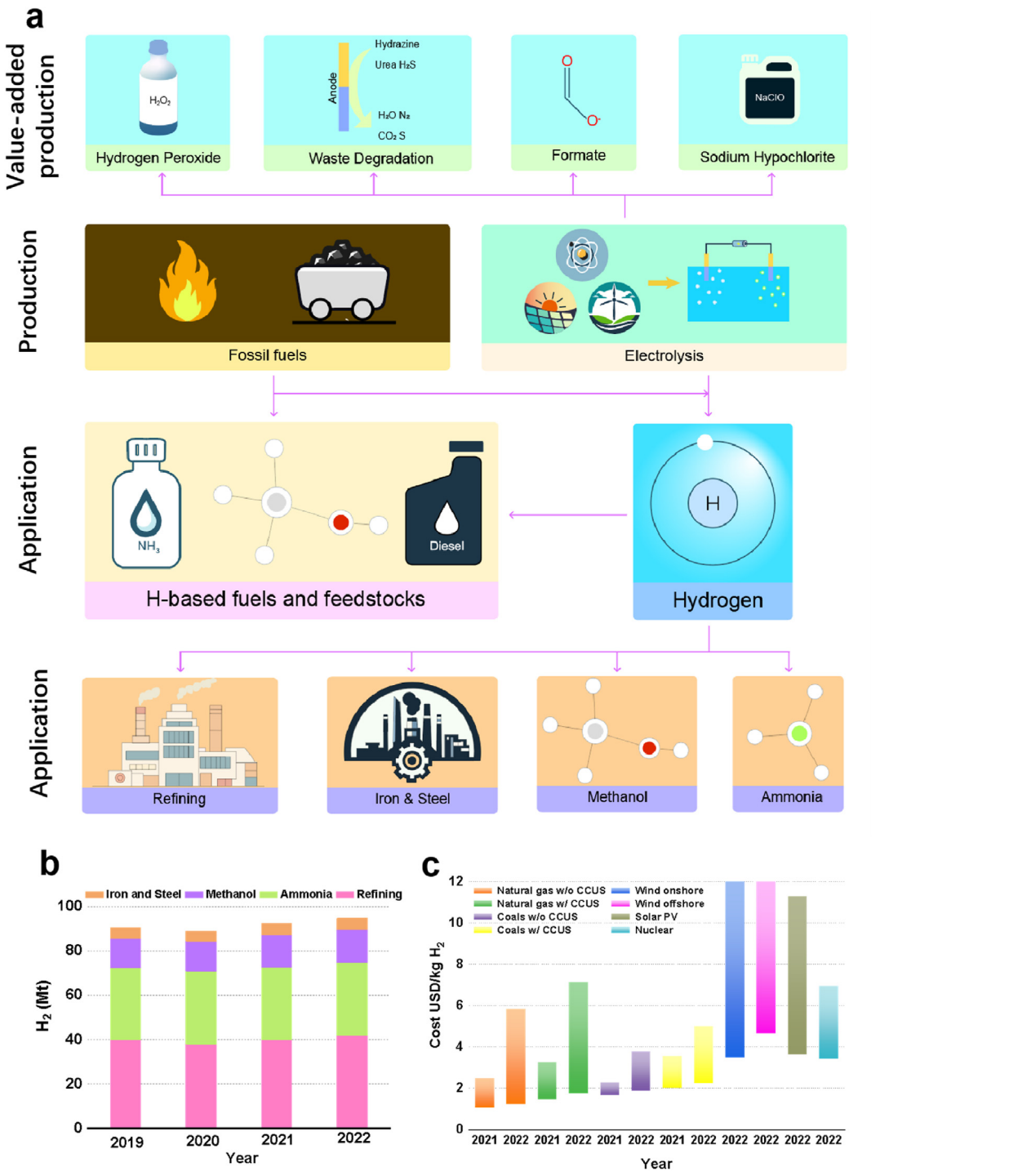


**Fig. 3.** (a) A schematic illustration of the hydrogen production and application chain under different scenarios and (b) statistical data on industrial consumption of hydrogen during the years 2019–2022. (c) Levelized cost of hydrogen production by technology in 2021 and 2022. w/o = without, w = with, CCUS = carbon capture, utilization, and storage, PV = photovoltaic. Solar PV, wind, and nuclear refer to the electricity supply used to power the electrolysis process. Data for (b) and (c) are derived from the Global Hydrogen Review 2023, International Energy Agency [27].

employment of well-designed GDE structures has enabled the attainment of industrial current densities [56,57]. However, challenges such as water flooding and salt precipitation swiftly undermine the performance of GDEs, leading to unsatisfactory stability. It is therefore imperative to optimize the structure of GDEs and fine-tune the balance between hydrophilicity and hydrophobicity in the gas diffusion layer and catalytic layer to maintain long-term electrolysis stability.

Electrolytes are essential for supporting electrochemical reactions by facilitating ion flow, upholding electrical neutrality, and enabling efficient electron transfer. The electrochemical performance of a reaction is intricately tied to factors like the type, concentration, temperature, and pH of the electrolyte [12]. Consequently, research efforts primarily focus on optimizing the electrolyte environment by studying these crucial elements. Typically categorized by their pH, acidic, alkaline, and neutral electrolytes serve as the standard media for converting small energetic molecules. Notably, most of the OER alternative reactions have been performed in alkaline solutions because more non-noble catalysts are available, and hydroxyl ions play a key role in promoting the oxidation of

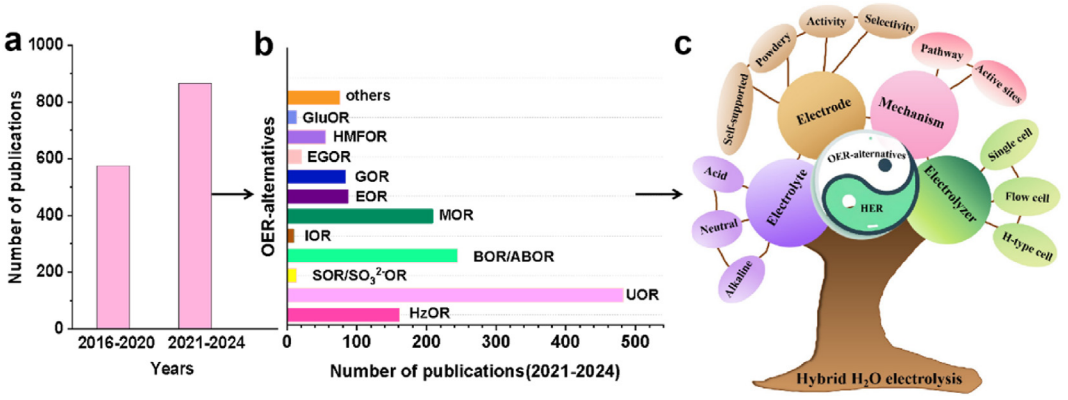


**Fig. 4.** Statistical data on publications related to hybrid $H_2O$ electrolysis since 2016 (a), the species and number of OER alternatives since 2021 (b), and the research focus on hybrid $H_2O$ electrolysis (c). The abbreviations for the OER alternatives are: HzOR = hydrazine oxidation reaction; UOR = urea oxidation reaction; SOR/$SO_3^{2-}$OR=$S^{2-}$/$SO_3^{2-}$ oxidation reaction; BOR/ABOR = sodium borohydride/amine borane oxidation reaction; IOR=$I^-$ oxidation reaction; MOR = methanol oxidation reaction; EOR = ethanol oxidation reaction; HMFOR = 5-hydroxymethylfurfural oxidation reaction; and GluOR = glucose oxidation reaction. The statistical data were obtained from the "Web of Science," retrieved by searching for the topics water electrolysis, water splitting, and hydrogen in association with the keywords "hydrogen evolution" and "OER alternatives."

small molecules [39]. In short, the selection of electrolyte mainly depends on the reaction type and the corresponding catalytic electrode.

Having evolved from common water-splitting applications, electrolyzers used in electrolysis systems with OER alternatives typically fall into two categories: the single-chamber (non-divided) electrolyzer (Fig. 5a) and the double-chamber (divided) electrolyzer (Figs. 5b–g). The commonly used electrolyzer species for full electrolysis are listed in Table 2. The selection hinges on the specific reactions required. A single-chamber cell suits scenarios where one electrolyte accommodates both cathode and anode reactions, and the introduced reactants, intermediates, and resulting products do not adversely affect the opposite electrode's reaction. Most water-splitting related studies have utilized single-chamber cells, thereby circumventing issues arising from membrane utilization [58–60]. The double-chamber cell has a separator (i.e., cation exchange membrane (CEM), anion exchange membrane (AEM), or bipolar membrane (BPM)) that allows reactions at both sides to occur within their respective favorable environments, free of interference from counter-electrode reactions. However, membrane utilization poses great challenges, leading to poor stability and high resistance. For instance, alkaline–acid hybrid electrolytes featuring different pH values for the catholyte and anolyte have been employed in numerous coupling electrochemical systems with OER alternatives, ensuring high reaction efficiencies under respectively favorable reaction conditions while also reducing the input voltage for electrolysis via harvesting electrochemical neutralization energy [38,61]. Presently, the growing diversity of paired reactions makes the double-chamber cell more adaptable to electrolysis systems with OER alternatives. Optimizing the architecture of the double-chamber cell is now crucial for advancing electrolysis efficiency. The commonly used H-type cell (Figs. 5b and c) can be further redesigned into a flow cell (Figs. 5d–g) with a very short distance between cathode and anode, significantly mitigating mass transfer limitations and achieving industry-scalable current density. The flow cell in Fig. 5e is appropriate for hybrid electrolysis with soluble reactants at both the cathode and the anode, such as by coupling $NO_3^-$RR and electrocatalytic hydrogenation organics with small-molecule oxidation reactions [62]. A flow cell involving a gas diffusion layer (GDL) is suitable for electrolysis with gas reactants or products. The electrolyzer in Fig. 5f is used extensively in $CO_2$RR/CORR electrolysis systems, which can be further optimized into the structure shown in Fig. 5g by employing a membrane electrode assembly (MEA). For example, in a hybrid system coupling $CO_2$RR with the formaldehyde oxidation reaction (FOR), the potential required to reach 100 mA $cm^{-2}$ was reduced from 1.21 V in a GDL-involved flow cell to 0.86 V in a MEA electrolyzer, greatly improving electrolysis efficiency [63]. Nevertheless, the stability of these two types of electrolyzers remains a challenging issue for hybrid

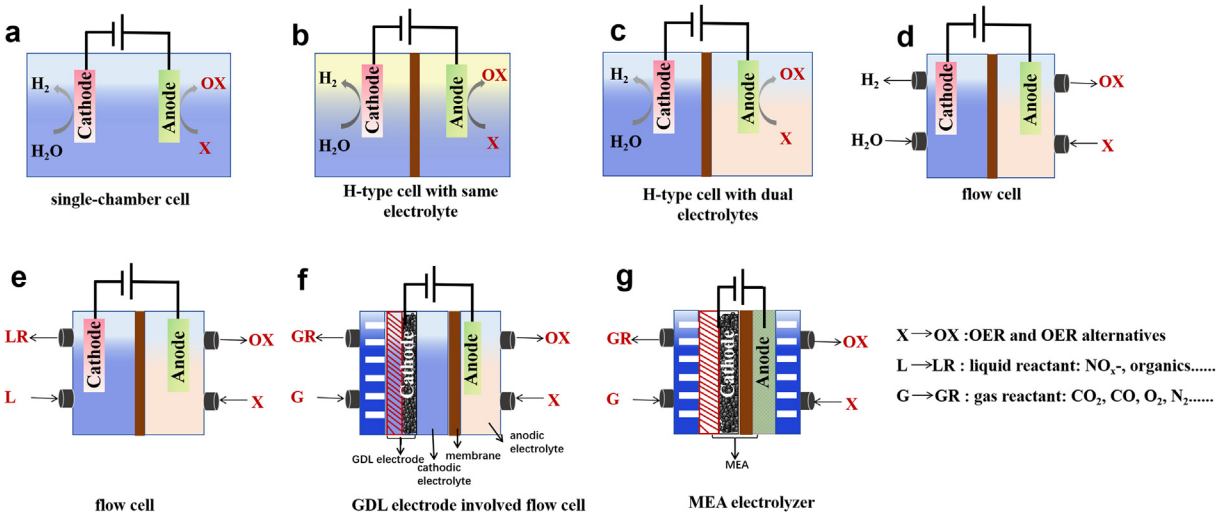


**Fig. 5.** Diagrams of various types of electrolyzers for hydrogen production from water splitting (a–d) and their derivative cells for dual value-added production (e–g).

**Table 2**
Electrolyzer species for full electrolysis.

| Electrolyzer type | Constituents | Application | Advantages | Disadvantages |
|---|---|---|---|---|
| Single-chamber cell | One chamber, electrolyte, and electrodes | One electrolyte accommodates both cathodic and anodic reactions | 1. Simple device<br>2. Circumvents issues from membrane utilization | 1. Extra separation cost from mixing products<br>2. Limited mass transfer and low reaction rate |
| H-type cell | Two chambers, electrolytes, electrodes, membrane (BPM, AEM, or CEM) | Reactions need separated reaction environment | Allows reactions to occur within their respective favorable environments | 1. Issues caused by membrane utilization, like increased resistance and instability<br>2. Limited mass transfer and low reaction rate |
| Flow cell | Two chambers, running electrolytes, electrodes, membrane (BPM, AEM, or CEM), liquid pumps | Reactions need separated reaction environment | Mitigates mass transfer limitations and achieves high reaction rate | 1. Issues caused by membrane utilization<br>2. Increased energy for electrolyte transport |
| GDL-involved flow cell | Two chambers, running electrolytes, GDL-involved electrodes, membrane (BPM, AEM, or CEM), liquid pumps, gas passage | Reactions with gas reactants or products | Mitigates mass transfer limitations and achieves high reaction rate | 1. Issues caused by membrane utilization<br>2. Increased energy for electrolyte transport.<br>3. GDE-induced instability |
| MEA electrolyzer | GDL-involved electrodes, membrane (BPM, AEM, or CEM), gas passage | Reactions with gas reactants or products | Greatly mitigates mass transfer limitations and promotes reaction rate | 1. Issues caused by membrane utilization<br>2. Increased energy for electrolyte transport.<br>3. GDE-induced instability |

electrolysis systems, closely related to the catalyst, electrode, electrolyte, and electrolyzer structure. The above types of electrolyzers are basic devices, which can be endowed with more functions by introducing light and heat [64,65] or detectors [66], modifying the membrane structure [57,67], increasing the chambers [68], and so on. In all, the holistic enhancement of these critical factors deserves increased attention in the study of these hybrid electrolysis systems.

## 3. Advanced characterization techniques for investigating reaction mechanisms

Hybrid electrosynthesis systems involve a complex array of reactions. Investigating reaction mechanisms is crucial for understanding each reaction, clarifying the structure–property relationships, and designing efficient catalysts for specific reactions. During the last decade, numerous techniques have been developed to investigate mechanisms in depth via gathering important information on reaction pathways, key intermediates, catalytic surface structure, and active sites. These techniques can be grouped into two types: *in situ/operando* electrochemical characterizations and theoretical calculations (Fig. 6). In this section, the function of these techniques and methods in the mechanistic investigation of electrolytic reactions will be introduced.

### 3.1. Advanced in situ/operando characterization techniques

The *in situ/operando* electrochemical characterization techniques, which commonly couple a tailor-made electrochemical cell with a physical property characterization technique, can provide important experimental evidence to identify catalytic mechanisms. Numerous *in situ/operando* electrochemical techniques have been developed for studying the mechanisms of electrocatalytic reactions, especially the $CO_2$RR, including vibrational characterization techniques like infrared (IR) spectroscopy [69], Raman spectroscopy [70] and ultraviolet–visible (UV–vis) spectroscopy [62], as well as X-ray characterization techniques like X-ray absorption spectroscopy (XAS) [71] and X-ray photoelectron spectroscopy (XPS) [72]; others include imaging characterization techniques like scanning electrochemical microscopy (SECM) [73], scanning tunnelling microscopy (STM) [74], atomic force microscopy (AFM) [75], scanning electron microscopy (SEM) [76], and transmission electron microscopy (TEM) [77], plus additional techniques like *in situ* nuclear magnetic resonance spectroscopy (NMR) [78,79] and online electrochemical–mass spectroscopy (EC-MS) [80,81]. These characterization techniques perform their own functions in

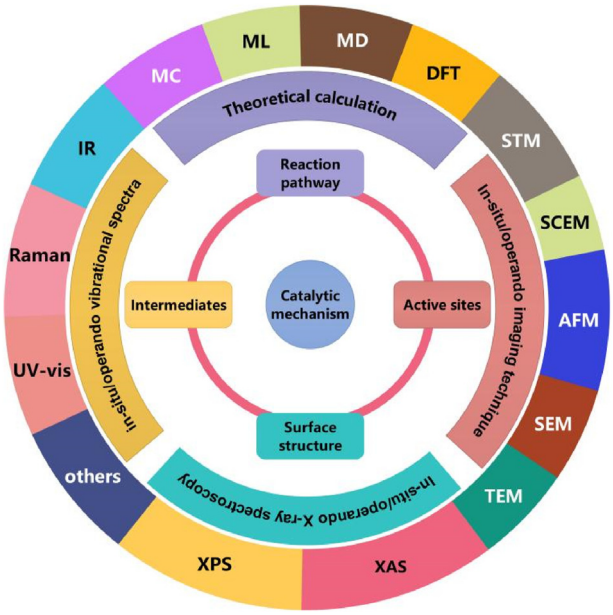


**Fig. 6.** Scheme of various *in situ/operando* electrochemical characterizations and theoretical calculations for investigating catalytic mechanisms. IR: Infrared, UV–vis: ultraviolet–visible, XPS: X-ray photoelectron spectroscopy, XAS: X-ray absorption spectroscopy, TEM: transmission electron microscopy, SEM: scanning electron microscopy, AFM: atomic force microscopy, SCEM: scanning electrochemical microscopy, STM: scanning tunneling microscopy, DFT: density functional theory, MD: molecular dynamics, ML: machine learning, MC: Monte Carlo.

revealing reaction mechanisms, and a combination of multiple techniques is generally required to ensure the validity of the proposed mechanisms.

As non-destructive vibrational spectrum techniques, IR spectroscopy and Raman spectroscopy have become mainstream tools for investigating catalytic mechanisms due to their ease of accessibility. IR spectroscopy can monitor adsorbed intermediates on the catalyst surface by analyzing their vibrational frequencies. The *in situ* attenuated total reflection (ATR) IR mode, with high surface sensitivity and minimal electrolyte layer interference, is used extensively to study the catalytic mechanisms of various reactions. The absorption signal can be further enhanced by depositing a thin metallic layer atop the reflecting crystal, a technique

known as surface-enhanced infrared absorption spectroscopy (SEIRAS) [82]. Employing the *in situ* ATR-SEIRAS technique, intermediates like *CO, the dimer intermediate *OCCO, and *CHO have been observed during the $CO_2$ reaction process; detection of these plays a key role in clarifying the reaction pathway for forming multicarbon products [69,83]. Aside from the $CO_2$RR, reaction processes like the $N_2$RR [84] and alcohol molecule oxidation [38,85] have also been investigated in-depth using this technique. For instance, the key intermediates of the glycerol oxidation reaction, like glyceraldehyde and glycolate, were detected by analyzing the vibration bond information, which helped with speculating about the reaction pathway [38]. Raman spectroscopy reveals molecular vibrational and rotational modes by detecting inelastically scattered light. This allows for the identification and characterization of molecular structures, compositions, and interactions, as each molecule has unique modes [10,86]. Though both Raman and IR spectroscopy offer insights into molecular vibrations, they each detect distinctive vibrational transitions. Raman spectroscopy is particularly useful for analyzing non-polar bonds and symmetric vibrations, and it excels in capturing vibrational signals in the low-wavenumber range, which can be a limitation for IR spectroscopy. In this way, Raman spectroscopy serves as a valuable complement to IR spectroscopy. An additional benefit of Raman spectroscopy compared to IR spectroscopy is the low Raman scattering cross-section character of water, which allows its use as a solvent without significantly disturbing the surface signal. This characteristic is vital for *in situ* Raman measurements. By employing *in situ* Raman spectroscopy, both adsorbed intermediates and changes in the catalyst's surface can be monitored. For instance, time-resolved surface-enhanced Raman spectroscopy (TR-SERS) monitored the dynamics of $CO_2$RR intermediates and a Cu surface with sub-second time resolution, which revealed the occurrence of surface reconstruction and nanostructure formation within the first 7 s after the onset of cathodic bias, followed by the formation of a stable Cu–OH surface in an increasingly alkaline local environment [87].

Apart from the benefits of identifying surface-adsorbed intermediates, studying catalyst reconstruction processes is crucial for building a clear understanding of structure–property relationships. Numerous *in situ/operando* imaging characterization techniques, including AFM, STM, SCEM, TEM, and SEM, have been used to study real-time changes in surface structure, catalyst morphology, size, phase, and environmental effect during operation. These techniques have been used extensively to resolve controversies about the dynamic morphology of Cu catalysts during the $CO_2$RR by combining them with *in situ/operando* X-ray techniques. Among these, AFM is a non-destructive scanning probe technique, wherein a mechanically sharp tip is attached to a flexible cantilever, and tiny deflections on the cantilever caused by the force between the tip and the substrate (conductive or non-conductive) are detected and kept constant, generating a topographic image of the substrate [88]. *In situ/operando* AFM can provide high-resolution nanoscale imaging of the surface in real time, offering advantages for identification and surface sensitivity over *in situ* IR and electron microscopy. Using *in situ* electrochemical AFM, Simon et al. observed phase formation, morphological transformation, and structural reconstructions over a model Cu(100) electrocatalyst during the $CO_2$RR process at the atomic scale, providing valuable information for revealing the structure–property relationships of a Cu electrode for the $CO_2$RR [75]. Electron-based microscopy techniques such as *in situ* SEM and TEM have also been used to characterize immediate changes in catalysts during reaction processes. *In situ* electrochemical SEM allows researchers to observe the surface morphology and dynamics of materials in real time during electrochemical reactions [76]. *In situ* electrochemical TEM enables real-time observation of electrochemical processes at the atomic or nanoscale level, providing extensive structural information like size, shape, surface structure, and crystalline texture at the nanoscale. For instance, the reconstruction of a Cu catalyst during the $CO_2$RR was revealed by *in situ* TEM, which showed that instead of coalescing, the Cu nanoparticles underwent dissolution, followed by redeposition [77].

Vibrational spectrum and imaging techniques are limited to detecting surface information. This can be addressed by the X-ray technique, which provides access to structural information down to minute changes in lattice parameters. *In situ* XAS is a highly sensitive analytical technique that characterizes the active sites and structural evolution of crystalline or amorphous nanostructured catalytic materials under reaction conditions by analyzing the electronic and geometrical structure of absorbing atoms. An XAS spectrum can be divided into three regions: the pre-edge, the X-ray absorption near edge structure (XANES), and the extended X-ray absorption fine structure (EXAFS) [88]. XANES can identify the electronic structure and local geometry around the atom that absorbs the X-ray radiation, providing information on the oxidation states and local coordination chemistry of the absorbing atoms. For instance, the reduction of $Cu_2O$ into metallic Cu during the $CO_2$RR was observed by *in situ* XANES [77]. EXAFS spectroscopy provides quantitative structural information about details such as the coordination environment and coordination number of metals and metal ions. For example, *in situ* EXAFS revealed changes in the coordination structure of metal-$N_4$ moieties during the ORR, whereby the Cl–Co–$N_4$ moiety was reconstructed into an unsaturated Cl–Co–$N_2$ structure via dynamically releasing two N coordinations at the early reaction state. The Cl–Co–$N_2$ thus formed served as the true active site for the ORR [71]. Another advanced *in situ* X-ray technique is XPS, which can provide immediate information on the surface element composition, chemical states, and electronic state within a few nanometers' depth of catalysts under catalytic conditions. For instance, *quasi-in situ* XPS applied to the $CO_2$RR revealed the rapid formation of a metallic Ag surface in the near-surface region of the catalyst within 3 min, though TEM and *operando* EXAFS confirmed that oxygen remained in the bulk of the catalyst after 1 h of reaction [72].

Apart from the advanced techniques mentioned above, other *in situ/operando/*online methods have also been employed to provide information on molecular reconstruction, intermediates, and pathways. These include *in situ* electrochemical UV–vis spectroscopy [62], online EC-MS and isotope techniques [80,81], and *in situ* NMR [78,89]. For example, Jiao et al. revealed the CORR reaction mechanism over a polycrystalline Cu GDL electrode using a flow electrolyzer mass spectrometry (FEMS) technique they developed, which enabled the monitoring of reactive intermediates at a current density greater than 100 mA $cm^{-2}$. By combining this with isotope techniques, it was observed that the oxygen in the as-formed acetaldehyde intermediate originates from the CO feed, while the oxygen in ethanol and n-propanol primarily comes from the solvent [81]. The above advanced techniques significantly enhance our understanding of the catalytic mechanisms involved in heterogeneous electrochemical catalysis. However, most of these *in situ* techniques necessitate harsh operating conditions, expensive instrumentation and maintenance, as well as highly specialized knowledge for data analysis, like the *in situ* XAS technique, which limits their accessibility and wide application. In the future, there is a need to develop *in situ* techniques that can monitor electrosynthesis under industrial-scale working conditions, so that more practical issues will be discovered and solved.

### 3.2. Advanced theoretical calculations

Over the past few decades, theoretical calculations/simulations have made great contributions to estimating catalytic mechanisms and predicting catalyst performance. Four main methods—molecular dynamics (MD) simulations, density functional theory (DFT), Monte Carlo (MC) simulation, and machine learning (ML)—are extensively used in the field of electrocatalysis. MD simulations, which rely on classical Newtonian mechanics, analyze the behavior and interactions of reactants at catalyst interfaces, focusing on adsorption and activation dynamics at the molecular level [90,91]. Conversely, DFT, a quantum-mechanical approach at the atomic level, is utilized to investigate the electronic structures of multiple-electron systems and is particularly effective for analyzing the free energy and electronic structure of reactions in electrolysis [92].

Gu et al. [93] recently investigated metal-free B-doped graphene as a catalyst in the electrochemical advanced oxidation process (EAOP), using

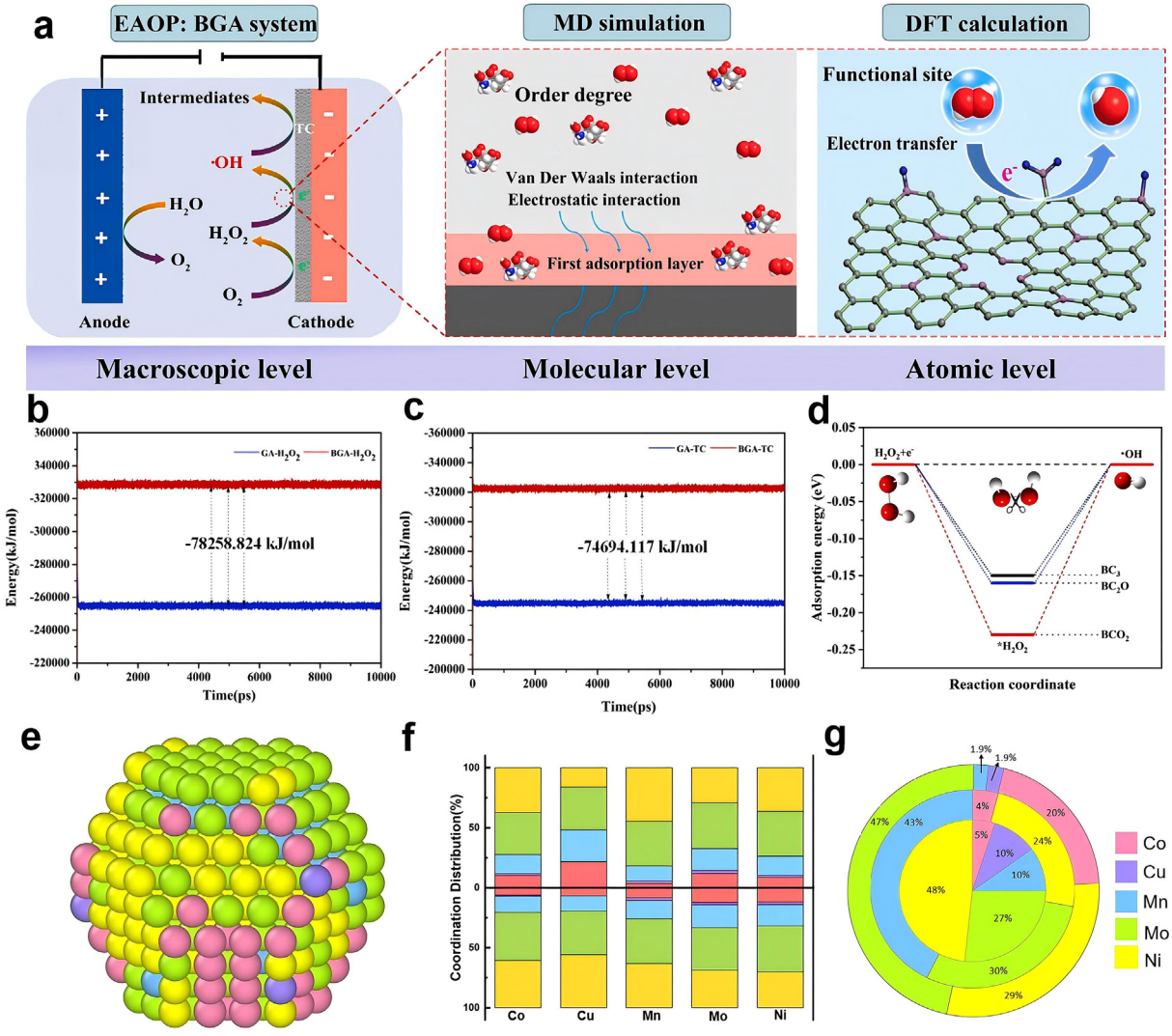


**Fig. 7.** (a) Schematic of investigating the oxidation mechanism of B-doped graphene aerogel via experiments, molecular dynamics simulations, and DFT. The interaction energy between catalysts and $H_2O_2$ (b) or TC (c). (d) Adsorption energies of each B-doped site to $H_2O_2$. Reproduced with permission from Ref. [93]. Copyright 2022, Elsevier. (e) Optimized structures achieved by the end of AIMC, (f) catalyst-dependent distribution fractions of the surface atoms, and (c) layer-dependent fraction of elements corresponding to CoNiCuMnMo-NPs. Reproduced with permission from Ref. [38]. Copyright 2022, American Chemical Society.

a combination of MD simulation and DFT (Fig. 7a). To describe interatomic interactions and calculate forces, the molecular force field OPLS-AA (optimized potentials for liquid simulations all-atom) [91,94] was employed in the MD simulation to evaluate interaction energies, including Coulombic interaction and Lennard–Jones potential, between the catalysts and reactants like $H_2O_2$ (Fig. 7b) and tetracycline (Fig. 7c), represented as BGA (B-doped graphene aerogel) and GA (graphene aerogel). These simulations revealed that $H_2O_2$ was activated at the active sites on the catalyst surface, leading to the production of highly energetic free radicals, with BGA showing superior activation potential compared to GA. Further DFT calculations clarified the activation mechanisms of $H_2O_2$ on three B-doped types (–$BC_2O$, –$BCO_2$, –$BC_3$), highlighting –$BCO_2$ as a key site for •OH radical production, while the –$BC_2O$ and –$BC_3$ structures enhance early-stage $H_2O_2$ yield (Fig. 7d). The overall results confirmed that •OH radical formation primarily occurs through O–O bond breakage, while the activation ability can be enhanced by additional binding sites provided by the –$BC_2O$ structure.

Monte Carlo (MC) simulation, a stochastic method that utilizes probability and statistical theory, is another prevalent computational technique alongside MD simulation. MC simulations employ random numbers to address various computational challenges through probabilistic modeling and statistical sampling to approximate solutions. While akin to MD in requiring molecular force fields, pinpointing an accurate force field for specific system, especially large-scale systems, remains challenging. In response, machine learning potentials (MLPs) have emerged as a cost-effective and accurate alternative to traditional force fields [95]. Our group reported on a high-entropy alloy, CoNiCuMnMo (HEA-CoNiCuMnMo), which demonstrates promising electrochemical activity for the glycerol oxidation reaction (GOR) [38]. Unraveling the catalytic mechanism involves accurately determining surface atomic configurations, a task that is infeasible for HEAs ranging from 2 nm to 400 atoms in size when employing Nørskov's method [96]. To address this challenge, we developed an algorithm that translates DFT results into MLPs, enabling the application of MLP-based *ab initio* MC (AIMC) simulations on a macroscopic scale for HEAs. Figs. 7e–g display the simulation outcomes for CoNiCuMnMo-NPs, elucidating the theoretical GOR volcano and the coordination of the most active site and thereby advancing our understanding of the catalytic mechanism and the identification of active sites.

Theoretical calculations play an indispensable role in electrochemistry, including for advancing our understanding of catalytic mechanisms and designing efficient catalyst systems. Techniques such as MD, MC simulations, and DFT, particularly when augmented with MLPs, offer profound insights into the atomic details of electrochemical reactions. These

computational tools allow for the exploration of complex reaction dynamics and catalyst structures that are otherwise challenging to probe experimentally. Looking ahead, the future of electrochemical research will likely focus on overcoming more barriers through the development of more sophisticated and tailored computational strategies. Enhanced algorithms and the incorporation of more advanced machine learning models promise to improve the accuracy and efficiency of simulations. Furthermore, as computational power increases and new methodologies emerge, the potential to simulate larger systems over longer timescales will become a reality, offering even deeper insights into the fundamental processes governing electrochemistry. This progression will undoubtedly facilitate the discovery and optimization of next-generation materials and catalysts, driving forward the fields of energy conversion and storage.

## 4. Hybrid electrolysis systems by coupling $CO_2$RR/CORR/$2e^-$ORR/NRR/others with OER alternatives

Prompted by the developed water-splitting hybrid systems as well as these aforementioned techniques, more complex hybrid electrosynthesis systems have been proposed to produce dual value-added products. Over the last decade, numerous new hybrid electrolytic systems have emerged, expanding beyond water electrolysis. This section provides an overview of the development of hybrid electrolysis systems that produce dual value-added products by coupling $CO_2$RR, CORR, $2e^-$ORR, NRR, and other reduction reactions in the cathode with various upgraded OER alternatives in the anode in aqueous solution (Fig. 8). The focus is primarily on the catalysts developed and the corresponding catalytic mechanisms, as well as on the electrochemical performance of these hybrid electrolysis systems, with the aim of providing a comprehensive understanding of how to optimize these electrosynthesis systems.

### 4.1. Coupling the $CO_2$RR with OER alternatives

Developing $CO_2$ conversion technologies that harness $CO_2$ as a resource is critical to slow down the rapidly escalating atmospheric $CO_2$ concentration [12,97,98]. Electrochemical $CO_2$ reduction in aqueous solution stands out among various techniques due to its numerous merits, including environmentally friendly, renewable driving force, mild reaction conditions, adjustable product outputs, and versatile device configurations [12]. However, the inherent inertness of $CO_2$ and the diversity of potential reduced products (e.g., CO, $CH_4$, HCOOH, $C_2H_4$, $C_2H_5OH$, etc.) are significant challenges to achieving promising conversion efficiency. The pursuit of efficient electrocatalysts for the $CO_2$RR has been a primary focus. Over the last decade, research on the $CO_2$RR has witnessed exponential growth, buoyed by advancements in nanotechnology, *in situ* characterization techniques, and computational modeling. Remarkable advancements have been made in designing catalysts, elucidating molecular-level reaction pathways, and developing scalable electrochemical systems [12,99]. However, despite these strides, $CO_2$ electrolysis still grapples with the challenge of a relatively high electrical energy requirement, over 80% of which is attributed to the energy-intensive anodic OER [98]. Thus, strategies from hybrid water electrolysis are being adopted. Reported OER alternatives to $CO_2$ electrolysis that can yield valuable products at the anode include the oxidation of chloride [100], $H_2O$ [101], sulfides [45], alcohols [98,102], and some other organics [63,103], which can be grouped into inorganic oxidation and organic oxidation according to the reactants. This section will delve into the latest advancements in $CO_2$ electrolysis coupled with OER alternatives, categorized by the types of OER alternatives employed. The performance of designed catalysts, the corresponding catalytic mechanism, and the overall electrolytic performance will be presented. To obtain a better overview, the electrochemical performance values of these excellent hybrid systems are listed in Table 3.

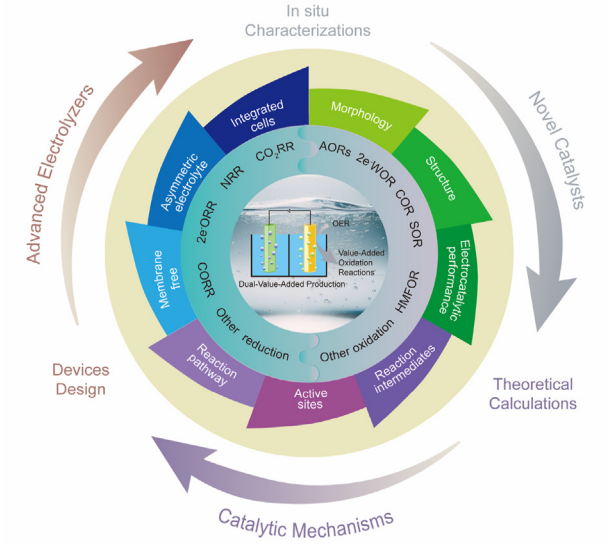


**Fig. 8.** Overview of hybrid systems with OER alternatives beyond water electrolysis.

#### 4.1.1. Coupling the $CO_2$RR with inorganic oxidation reactions

*4.1.1.1. Coupling the $CO_2$RR with the chloride ion oxidation reaction.* Coupling the cathodic $CO_2$RR with the chloride ion oxidation reaction ($CO_2$RR||COR), allows for the chlor-alkali process and the conversion of $CO_2$ into value-added products to occur simultaneously. Moreover, the coupling system offers the potential to leverage seawater, a vast resource, so it has garnered significant interest within the research community [24,100,104–106]. A pioneering electrolysis setup was facilitated using commercially available $RuO_2$/Ti for the anodic COR, with cathodic $CO_2$ reduction into CO catalyzed by single iron atoms immobilized on nitrogen-doped carbon (Fe–SAs/N–C) [106]. The Fe–SAs/N–C demonstrated remarkable selectivity toward CO production, because the individual Fe atoms greatly reduced the energy demand in the rate-determining step, resulting in excellent $CO_2$RR performance. Capitalizing on the good activity of the prepared catalyst, the proposed electrolysis system achieved a commendable energy efficiency of 82% at a cell voltage of 2.0 V in an H-type cell configuration. In a separate study, the performance of the $CO_2$RR||COR electrolysis system was significantly enhanced through the utilization of meticulously engineered catalysts on both sides (Fig. 9a) [105]. On the anode side, an ordered mesoporous $Co_3O_4$ (OMP-$Co_3O_4$) catalyst was synthesized as the active COR catalyst, achieving an impressive $FE_{ClO^-}$ of 81% at 1.9 $V_{RHE}$ in a 2 M KCl medium, far beyond those of large accumulated mesopores (AMP-$Co_3O_4$) and nonporous $Co_3O_4$ (NP–$Co_3O_4$) (Figs. 9b–d). Meanwhile, on the cathode side, an ordered mesoporous nickel and nitrogen co-doped carbon (OMP-Ni-N-C) was prepared for catalyzing the $CO_2$RR and maintained a peak $FE_{CO}$ of 99% at −0.6 $V_{RHE}$ in a 2 M KCl aqueous solution (Fig. 9e). The superior performances of these catalysts can be attributed to the unique ordered mesoporous structures, which expose a higher number of active sites. Configured with the aforementioned dual electrodes within a single-chamber cell, the integrated $CO_2$RR||COR electrolysis system exhibited impressive efficiency, yielding a remarkable $FE_{CO}$ of 97% at the cathode and a $FE_{ClO^-}$ of 87% at a cell voltage of 2.5 V. This notably reduced the cell voltage by 1.8 V and resulted in a 40% increase in energy efficiency compared to the $CO_2$RR||OER electrolysis system (Fig. 9f).

The performance of $CO_2$RR||COR electrolysis in actual seawater has also been studied to bring it closer to requirements for practical applications. Qiu et al. conducted direct $CO_2$ electrolysis in seawater, with the cathodic $CO_2$RR facilitated by CoPc molecule-implanted graphitic carbon nitride nanosheets (CoPc/g-$C_3N_4$) as the electrocatalyst (Fig. 9g) [24].

**Table 3**
Coupling the $CO_2$RR/CORR with OER-alternative oxidation reactions.

| Catalysts (cathode/anode) | Catholyte\|\|anolyte | Products (cathode (FE)/anode (FE)) | Cell potential (V) | Current density (mA $cm^{-2}$) | Cell type | Tested long-term stability (h) | Ref. |
|---|---|---|---|---|---|---|---|
| Fe–SAs/N–C\|\|$RuO_2$/Ti | 0.5 M NaCl\|\|0.5 M NaC | CO(93 %)/$ClO^-$(92%) | 2.0 | NG | H-type | 3 | [106] |
| Ni-CB\|\|$RuO_2$–$IrO_2$–$TiO_2$ DSA mesh | 2 M $KHCO_3$\|\|saturated KCl (pH = 2) | CO(~98.5%)/$Cl_2$ (~80%) | 3.8 | 100 | GDE involved flow cell | 5 | [104] |
| CoPc/g-$C_3N_4$\|\|commercial electrode | 0.6 M NaCl\|\|saturated M NaCl | CO(98.1%)/$Cl_2$(NG) | 3.0 | 12.9 | H-type | 25 | [24] |
| OMP-Ni-N-C\|\|OMP-$Co_3O_4$ | 2 M KCl\|\|2 M KCl | CO(97%)/$ClO^-$(87%) | 2.5 | 20 | Single-chamber cell | 24 | [105] |
| Cu/GDL\|\|DSA anode | 0.5 M KOH+ 1.5 M sea salt+1 mg/mL EDTA\|\|0.5 M KOH | $C_2H_4$(47%)/$ClO^-$(85%) | NG | 100 | GDE involved flow cell | 1000 s | [100] |
| Zn/$SnO_2$\|\|Zn/$SnO_2$ | 2 M $K_2CO_3$\|\|2 M $K_2CO_3$ | Formate (85.7%)/$H_2O_2$ (72.8%) | 4.2 | ~150 | GDE involved flow cell | 60 | [101] |
| Cu/Vulcan GDE\|\|BDD | 1 M KOH+2 M KI\|\|4 M $K_2CO_3$ | $C_2H_4$(~60%)/$H_2O_2$(~60%) | ~5 | 200 | GDE involved flow cell | 50 | [109] |
| Bi-ene\|\|Ni–NF-Af | $CO_2$-saturated 0.5 M $KHCO_3$\|\| Ar-saturated 1.0 M KOH with 0.5 M methanol | Formate (~100%)/formate (~100%) | 2.13 | 10 | H-type cell | 0.66 | [114] |
| Ni&NiNC\|\|Ni-MOFs@350 | 1 M KOH\|\|1 MKOH with 1 M methanol | CO(over 90%)/formate (~90%) | 2.74<br>2.4 | 100<br>500 | GDE involved flow cell<br>MEA-equipped reactor | 8<br>8 | [115] |
| CuSn-4\|\|CuSn-4 | $CO_2$-saturated 0.5 M $KHCO_3$\|\| Ar-saturated 1 M KOH with 1 M methanol | Formate (90.6%)/format (96.5%) | 3.32 | 100 | H-type cell | 5 | [121] |
| HOD-Cu\|\|HOD-CuO | $CO_2$-saturated 0.5 M $KHCO_3$\|\| 1 M KOH with 1 M methanol | NG | 2.18 | 10 | H-type cell | 30 | [65] |
| | $CO_2$-saturated 0.5 M $KHCO_3$\|\| 1 M KOH with 1 M methanol | formate (58%)/formate (88%) | Solar-driven | 10 | Solar-driven GaInP/GaAs/Ge triple-junction solar H-type cell | 12 | |
| 3D Bi-ene-A/CM\|\|Ni$(OH)_2$/NF | $CO_2$-saturated 0.5 M $KHCO_3$\|\| 1 M KOH with 0.5 M methanol | Formate (above 90%)/ formate (90%) | 2.303 | 10 | GDE involved flow cell | 1 | [137] |
| m$SnO_2$/CC\|\|CuONS/CF | $CO_2$-saturated 1 M $KHCO_3$\|\|1 M KOH with 1 M methanol | Formic acid (80.5%)/formic acid (91.3%) | 1.22 | 20 | H-type cell | NG | [102] |
| PCN-601\|\|PCN-601 | $CO_2$-saturated 0.5 M $KHCO_3$\|\| 1 M KOH with 0.1 M methanol | CO(above 80%)/formic acid (above 75%) | 1.99 | 5 | H-type cell | 7 | [138] |
| Ni-2CBpy$^{2+}$ -COF\|\|Ni-2CBpy$^{2+}$ -COF | $CO_2$-saturated 0.5 M $KHCO_3$\|\| 1 M KOH with 1 M methanol | CO(above 80%)/formic acid (94%) | 1.9 | 12.65 | H-type cell | 5 | [64] |
| InS\|\|np-$Ni_3P$ | $CO_2$-saturated 0.5 M $KHCO_3$\|\| 1 M KOH with 0.5 M methanol | Formate (~90%)/formate (above 90%) | 2.286 | 50 | GDE involved flow cell | 30 | [119] |
| A/c-BiB NAs/CF\|\|NiO/CN/NF | $CO_2$-saturated 0.5 M$KHCO_3$\|\| 1 MKOH with 1 M methanol | Formate (98.5%)/formate (93.3%) | 2.0 | ~7.5 | H-type cell | 12 | [139] |
| NiPc-MPor COFs\|\|NiPc-MPor COFs | $CO_2$-saturated 0.5 M $KHCO_3$\|\| 1 M KOH with 1 M methanol | CO(98.12%)/formic acid (93.75%) | 2.1 | ~6.2 | H-type cell | 8.5 | [122] |
| NiSAs/FN-CNSs/CP\|\|$CoSe_2$/CC | $CO_2$-saturated 2.0 M $KHCO_3$\|\| 2.0 M glycerol solution in 2.0 M KOH | CO (over 90%)/formate (over 90%) | 1.97 | 100 | GDE involved flow cell | 400 | [112] |
| Cu/PTFE\|\|Au-ND/NiF | $CO_2$-saturated 1 M $K_2CO_3$\|\|3 M KOH with 0.5 M glycerol | $C_2H_4$(~50%)/GA + FA (~50%) | 3.95 | 175 | GDL involved flow cell | 10 | [113] |
| BiOBr-GDE\|\|$Ni_xB$ | $CO_2$-saturated 1 M KOH\|\|1 M KOH + 1 M glycerol | Formate (96%)/formate (57%) | 4.33 | 100 | GDL involved flow cell | 2 | [117] |
| $N_3$NiPc–CNT\|\|$N_3$NiPc–CNT | $CO_2$-saturated 0.5 M $KHCO_3$\|\| $CO_2$-saturated 0.5 M $KHCO_3$ + 1 mmol L-DOPA | CO(100%)/poly-L-DOPA(NG) | 2.25 | 10 | H-type cell | NG | [103] |
| $BiO_x$\|\|NiO NPs | $CO_2$-saturated 0.5 M $KHCO_3$\|\| $CO_2$-saturated 0.5 M $KHCO_3$ with HMF | Formate (81%)/FDCA (36%) | 2.5 | 2 | H-type cell | 3 | [128] |

(*continued on next page*)

**Table 3** (*continued*)

| Catalysts (cathode/anode) | Catholyte\|\|anolyte | Products (cathode (FE)/anode (FE)) | Cell potential (V) | Current density (mA $cm^{-2}$) | Cell type | Tested long-term stability (h) | Ref. |
|---|---|---|---|---|---|---|---|
| InOOH-$O_V$\|\|InOOH-$O_V$ | $CO_2$-saturated 0.1 M $KHCO_3$\|\| Ar-saturated 1 M KOH + 10 mM HMF | Formate (above 90%)/FDCA (NG) | 2.27 | ~10 | H-type cell | NG | [53] |
| Cu1Bi/GDL\|\|NiCoLDH/NF | $CO_2$-saturated 1 M KOH\|\|1 M KOH with 0.1 M HMF | Formate (90%)/FDCA (85%) | 2.35 | 150 | MEA involved flow reactor | 10 | [131] |
| $Cu_2O$/CuNF@GDL\|\|CuO–NF@Cu | $CO_2$-saturated 0.5 M KCl\|\|2 M KOH with 10 mM HMF | $C_2H_4$(~71%)/FDCA (~93%) | 2.75 | ~190 | GDL involved flow cell | 5 | [132] |
| $SnO_2$\|\|$NiCo_2O_4$ | $CO_2$-saturated 1 M $NaHCO_3$\|\| 0.1 M PET hydrolysate | Formic acid (70%)/formic acid (~85%) | 1.9 | 20 | H-type cell | NG | [123] |
| BOC@rGO\|\|CuCoO@rGO | $CO_2$-saturated 1 M $KHCO_3$\|\|1 M KOH with 42 mM EG in PET hydrolysate solution | Formic acid (~70%)/formic acid (~80%) | 1.9 | 10 | H-type cell | 0.97 | [124] |
| Bi/$Bi_2O_3$\|\|Ni$(OH)_2$-VO | NG | Formic acid (~90%)/formic acid (~90%) | 2.7 | 100 | Solar-driven MEA involved flow reactor | 4.17 | [92] |
| p-Bi NSs\|\|Co–S NSs | 1 M KOH\|\|1 M KOH + 0.1 M $S^{2-}$ | Formate (above 90%)/sulfur (92.9%) | ~1.5 | 100 | H-type cell | 70 | [45] |
| V12e\|\|CAT-1@NF | $CO_2$-saturated 0.5 M $KHCO_3$\|\| $CO_2$-saturated 0.5 M $KHCO_3$ with 5 mM MTDQ | Formic acid (83.6%)/MDDQ (above 70%) | 2.52 | 10 | H-type cell | 8 | [136] |
| BiOCl\|\|$Cu_2O$ | $CO_2$-saturated 0.5 M $KHCO_3$\|\| 1 M KOH with 0.1 M HCOH | Formate (93.83%)/formate (93.67%) | 1.05 | 10.6 | H-type cell | 2 | [63] |
| | $CO_2$-saturated 2 M KOH\|\|2 M KOH with 0.1 M HCOH | Formate (92.6%)/formate (92.6%) | 1.2 | 100 | GDL involved flow cell | 0.5 | |
| | $CO_2$-saturated 1 M KOH\|\|1 M KOH with 0.1 M HCOH | Formate (93.04%)/formate (93.04%) | 1.0 | 126.9 | MEA involved flow reactor | 10 | |
| Cu@Sn NWs\|\|$MnO_2$/CP | $CO_2$-saturated 0.1 M $KHCO_3$\|\| 0.1 M $Na_2SO_4$ with 5 mM HCHO | CO(~93%)/formic acid (NG) | 2.5 | −2.72 | H-type cell | 6 | [133] |
| Cu@GDL\|\|Pt-CC | Humidified CO\|\|2.0 M KOH with 4.0 M glycerol | $C_{2+}$($C_2H_4$, $C_2H_6O$, $C_3H_8O$, 71%)/$C_3$(Lactic acid, glyceric acid, 75%) | 1.34 | 180 | MEA involved flow cell | 50 | [140] |
| Cu@GDL\|\|$NiFeO_x$ @NF | CO in 3 M KOH\|\|3 M KOH with alcohols | $C_{2+}$ (NG)/Acetate (~50%), Ethylene (~30%) | 2.15–2.23 | 200 | MEA involved flow cell | 120 | [57] |

NG: Not given.

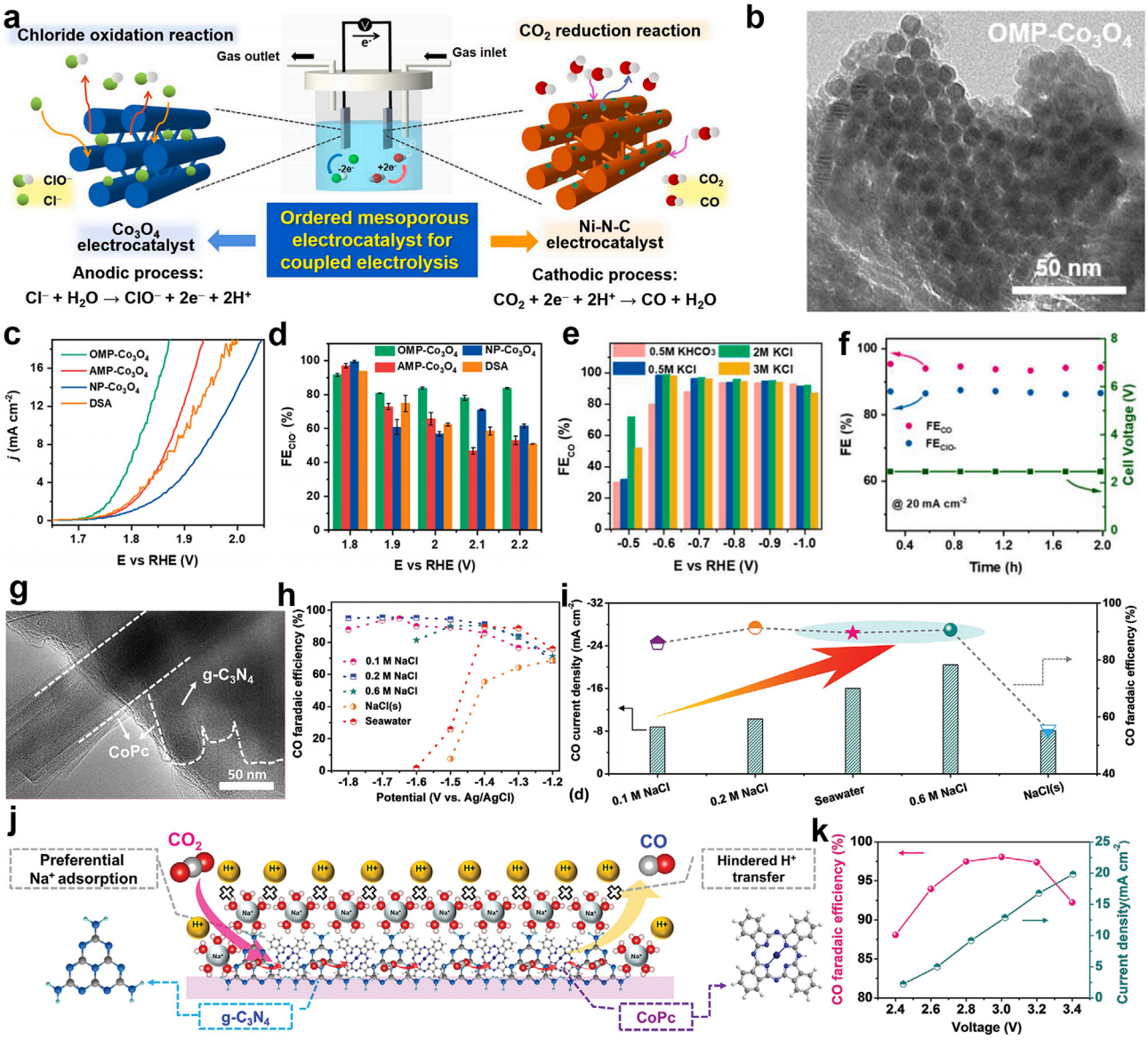


**Fig. 9.** (a) Hexagonally ordered mesoporous electrocatalysts for the coupled $CO_2RR||COR$ electrolysis system. (b) TEM images of OMP-$Co_3O_4$, viewed from the [001] direction. (c) LSV curves for the COR. Faradaic efficiency of $ClO^-$ (d) and CO (e). (f) Cell voltage, $FE_{CO}$, and $FE_{ClO^-}$ as functions of time for OMP-Ni-N-C||OMP-$Co_3O_4$ when the system was operated at 20 mA $cm^{-2}$ in a single-chamber electrolyzer. Reproduced with permission from Ref. [105]. Copyright 2022, Elsevier. (g) TEM image of CoPc/g-$C_3N_4$, (h) CO FEs at different potentials, (i) comparison of $FE_{CO}$ and CO current densities at −1.4 V vs. Ag/AgCl, (j) a schematic of preferential adsorption for $Na^+$ and hindered $H^+$ transfer on the electrode surface, and (k) $FE_{CO}$ and current density of overall $CO_2$ splitting in the $CO_2RR$-seawater system. Reproduced with permission from Ref. [24] Copyright 2021, Wiley-VCH.

Notably, the CoPc/g-$C_3N_4$ in natural seawater performed as well as in calculated seawater, yielding a similar $FE_{CO}$ of ~90% (Figs. 9h and i). The exceptional performance of CoPc/g-$C_3N_4$ stems from its negatively charged CoPc surface, robust electron interactions, and enhanced surface capacitive effects, along with its high N content, which was beneficial for suppressing the HER by preferentially adsorbing the $Na^+$ in the electrolyte, thereby fostering better $CO_2$ reduction activity (Fig. 9j). The $CO_2RR||COR$ electrolysis setup assembled with CoPc/g-$C_3N_4$ for the $CO_2RR$ in simulated seawater and a commercial electrode for the COR in saturated NaCl aqueous solution attained a peak $FE_{CO}$ of 98.1% at a cell voltage of 3 V (Fig. 9k). This study presents a viable technical pathway for the direct simultaneous production of CO and $Cl_2$ from seawater. In these reported $CO_2RR||COR$ electrolysis systems, CO emerges as the primary cathodic product, but converting $CO_2$ into higher-value multicarbon products would be more desirable [100,107]. Kang et al. achieved a breakthrough by co-producing $C_2H_4$ and hypochlorite in seawater [100]. Their innovative system involved the synthesis of a cathodic Cu catalyst through the *in situ* electrodeposition of Cu in a sea salt electrolyte containing EDTA. The introduced EDTA proved instrumental in generating abundant active sites by triggering intense Cu dissolution and deposition on the electrode surface within a $Cl^-$ rich environment. Additionally, EDTA's role in chelating free ions of Fe, Ni, and Zn in seawater helped prevent the formation of other metal impurities. The *in situ* formed Cu/GDL catalyst achieved a $FE_{C_2H_4}$ of 52% even at a high current density of 160 mA $cm^{-2}$. Assembled with the developed cathode and a commercial anode, the combined system successfully achieved the co-production of $C_2H_4$ with a FE of 47% and $ClO^-$ with a FE of 85%. This study offers an informative strategy for catalyst preparation and outlines a feasible blueprint for the application of coupled $CO_2RR$ electrolysis in seawater. Beyond their dual economic benefits, $CO_2RR||COR$ electrolysis systems have been explored for additional functionalities, such as producing $KHCO_3$ and degrading wastes via the formation of $ClO^-$ [104,108].

For the $CO_2$RR||CER electrolysis systems discussed above, research efforts have primarily concentrated on developing cathodic catalysts for the $CO_2$RR, with less emphasis placed on anodic catalysts. Furthermore, evaluations of these electrolysis systems have predominantly focused on basic electrochemical performance metrics, underscoring the necessity for additional exploration and the refinement of key parameters. Notably, the iodide ($I^-$) oxidation reaction—which is characterized by a lower anodic potential, produces valuable $I_2$, and has been shown to be feasible in hybrid water electrolysis—may also be adapted for $CO_2$ electrolysis.

*4.1.1.2. Coupling the $CO_2$RR with other inorganic oxidation reactions.* In addition to the well-known chlor-alkali process, other inorganic electrosynthesis reactions have been incorporated into $CO_2$ electrolysis [45, 101,109]. Despite the drawback of high thermodynamic potential in the two-electron water oxidation reaction (2e⁻WOR), coupling it with $CO_2$ electrolysis can eliminate the need for extra reactants, thus simplifying the electrolysis system. More importantly, this integration allows the production of highly valuable $H_2O_2$ at the anode. The co-production of formate at the cathode and $H_2O_2$ at the anode was first achieved in a $CO_2$RR||2e⁻WOR electrolytic system catalyzed by well-designed bifunctional Zn-doped $SnO_2$ nanodot catalysts (Figs. 10a and b) [101]. Based on experimental and theoretical findings, the doped Zn was confirmed to play a key role in modulating the electronic structure of the $SnO_2$, which promoted the coupling of *OH intermediates in $H_2O_2$ formation and also benefited the adsorption of *OCHO intermediates for formate generation, thus enhancing activity and selectivity. Equipped with the bifunctional catalysts within a flow cell, the $CO_2$RR||2e⁻WOR electrolytic system demonstrated favorable selectivity across a broad current density range of 50–300 mA $cm^{-2}$, with a peak $FE_{H_2O_2}$ of 80.65% and $FE_{formate}$ of 92.2%. The electrolyzer also maintained constant electrolysis at 4.2 V for more than 60 h at around 150 mA $cm^{-2}$ with a $FE_{H_2O_2}$ of 72.8% and $FE_{formate}$ of 85.7% in a 2 M $K_2CO_3$ aqueous solution (Figs. 10c and d). The innovative paired electrosynthesis presented in this study holds promise for extension to other electrolysis systems. Nevertheless, the relatively high potential required to drive the 2e⁻WOR may mitigate some of its substitution advantages. Future research endeavors should aim to develop additional active catalysts for the 2e⁻WOR within the $CO_2$RR||2e⁻WOR electrolytic system to match the current density of both reactions and further lower the cell voltage.

The electrochemical oxidation of industrial wastes into value-added products also presents a promising alternative to the OER in $CO_2$ electrolysis owing to its eco-friendliness and success in double-value-added production. Sulfides, a group of environmentally hazardous by-products in fossil fuels refining and coal-based chemical industries, and sulfide ions ($S^{2-}$) can easily be oxidized into S at a significantly lower thermodynamic potential compared to the OER. Thus, replacing the OER with the anodic oxidation of $S^{2-}$ (SOR) in $CO_2$ electrolysis ($CO_2$RR||SOR) offers the potential for dual-value-added production at ultra-low cell voltages. The initial conceptual validation of the $CO_2$RR||SOR electrolysis system was conducted by Ma et al., where the cathodic $CO_2$RR was converted into CO over a graphene-encapsulated zinc oxide catalyst, and the anodic $H_2S$ oxidation into S was mediated by EDTA-$Fe^{2+}$/EDTA-$Fe^{3+}$ redox couples on a graphene catalyst [110]. The system's performance was recently enhanced by Teng et al. [45] (Fig. 10e). In their study, two highly efficient catalysts were developed for the $CO_2$RR and SOR. The p-Bi nanosheets (p-Bi NSs) demonstrated exceptional catalytic $CO_2$ conversion into formate, with a FE of over 90% across a potential range of −0.6 V to −1.1 $V_{RHE}$, which was ascribed to the substantial electrochemical active surface area and rich Bi active sites within the p-Bi NSs. The Co–S nanosheets (Co–S NSs) presented remarkable SOR performance, with an onset potential of only 0.2 $V_{RHE}$ and a high FE for S generation of 98.2% at 0.7 $V_{RHE}$. Using the two developed catalysts

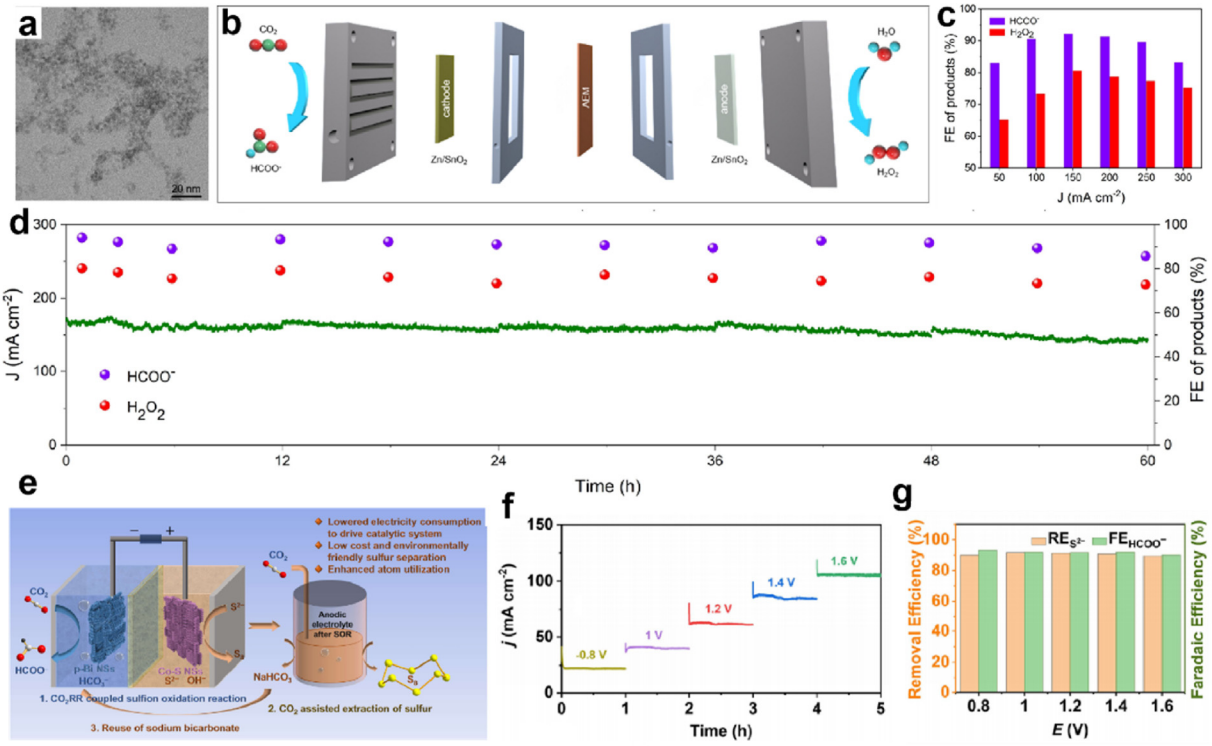


**Fig. 10.** (a) TEM image of $Zn/SnO_2$. (b) Schematic of an anion exchange membrane (AEM)-separated two-chamber flow electrolyzer. (c) FE of products over a $Zn/SnO_2$ couple under different current densities. (d) The chronoamperometric curve of the $Zn/SnO_2$ couple at a cell voltage of 4.2 V. Reproduced with permission from Ref. [101]. Copyright 2023, Wiley-VCH. (e) Schematic illustration of the $CO_2$RR||SOR system, followed by $CO_2$-assisted sulfur separation from the anodic electrolyte after the SOR. (f) Constant potential electrolysis. (g) $FE_{formate}$ and removal rate of sulfur in a potential range of 0.8–1.6 V. Reproduced with permission from Ref. [45]. Copyright 2024, Wiley-VCH.

within a flow cell, the electrolysis process was initiated at an exceptionally low cell voltage of 0.25 V. Across a potential range from 0.8 to 1.6 V, the system achieved both S removal efficiencies and $FE_{formate}$ exceeding 90%, with the highest current density surpassing 100 mA $cm^{-2}$ (Figs. 10f and g), demonstrating significantly lower electricity consumption compared with a conventional $CO_2$RR system. Moreover, they confirmed the availability of an efficient and environmentally friendly sulfur extraction technique achieved by aerating $CO_2$ into the anolyte after the SOR, the only by-product being $NaHCO_3$, which could be recycled as the catholyte for the $CO_2$RR.

#### 4.1.2. Coupling the $CO_2$RR with organic oxidation reactions

*4.1.2.1. Coupling the $CO_2$RR with alcohol oxidation reactions.* The alcohol oxidation reactions (AORs) represent a pivotal set of organic processes with extensive applications in fine chemistry, biomass upgrading, synthetic chemistry, and direct fuel cells [66,98,102,111]. The resulting valuable aldehydes and organic acids, characterized by their notably low thermodynamic oxidation potentials, position them as suitable candidates for integration in $CO_2$ electrolysis, facilitating energy-efficient $CO_2$ conversion and achieving dual-value-added production. Over the years, several types of AOR have successfully functioned as alternatives to the anodic OER in $CO_2$ electrolysis, underscoring the significance of designing active electrocatalysts and controlling the selectivity of oxidative products to ensure the high-yield production of valuable products at the anode [66,102,112]. The inaugural instance of a $CO_2$RR||AOR was initially documented by Bevilacqua et al. in 2014 [66], at a juncture when $CO_2$RR research was in its nascent stages, with ample room for improving selectivity and activity. They introduced a hybrid electrolysis system combining the $CO_2$RR with the ethanol oxidation reaction (EOR), in which a cathodic copper phthalocyanine-modified gas diffusion electrode (CuPc@GDE) facilitated the conversion of $CO_2$ into $CH_4$, $C_2H_4$, and formate, and anodic Pd nanoparticles supported on a sintered titanium web substrate ($Pd@Ti_{web}$) catalyzed ethanol conversion into acetate. Despite the relatively low selectivity of the $CO_2$RR (less than 20%) observed in this system, the work provided valuable insights for energy-efficient $CO_2$ electrolysis. With advancements in $CO_2$RR studies over the last five years, attaining high selectivity and activity across various catalysts has become achievable [102,112–115]. This shift in focus has prompted greater attention being paid to $CO_2$RR||AOR coupling systems, with the aim of reducing operating voltage while concurrently obtaining value-added products on both sides of the electrolysis cell. In 2019, Verma et al. explored hybrid $CO_2$ electrolysis systems incorporating cost-effective industrial by-product oxidation reactions, particularly the GOR, by combining experimental approaches and technoeconomic evaluation [98]. Their $CO_2$RR||GOR electrolysis system ($CO_2$RR||GOR), utilizing a cathodic Ag nanoparticles-supported GDL electrode and an anodic $IrO_2$-supported GDL electrode, featured a 53% reduction in electricity consumption compared to conventional $CO_2$ electrolysis. This study established glycerol as a promising feedstock for anodic oxidation reactions. Inspired by their work, several groups conducted a series of studies on co-electrolysis $CO_2$ and glycerol to further optimize the performance of this system [112,113,116–118]. In these $CO_2$RR||GOR electrolysis systems, flow cell devices incorporating cathodic GDEs were utilized to attain high current densities. Depending on the specific electrocatalysts employed, $CO_2$ reduction at the cathode occurred, yielding CO on carbon-based catalysts [112], formate on Bi-based catalysts [117,118], and multicarbons on Cu-based electrodes [113]. Concurrently, the GOR at the anode led to formate production on non-noble metal catalysts [112,116], and glycolic acid (GA) and dihydroxyacetone on noble metal-based catalysts [113,118]. Driven by relentless efforts, these co-electrolysis systems have attained significantly high selectivity on both sides when operated at current densities exceeding 100 mA $cm^{-2}$, rendering them promising candidates for practical applications. For instance, our group is devoted to optimizing the $CO_2$RR||GOR electrolysis system by designing catalysts that prioritize low cost, high selectivity, and excellent stability for both reactions [112]. Atomically dispersed Ni–N single sites on F, N co-doped carbon nanosheets (NiSAs/FN-CNSs) showcased exceptional $CO_2$RR performance with near unity $FE_{CO}$, while the interconnected $CoSe_2$ nanostructure grown *in situ* on carbon cloth ($CoSe_2$/CC) for the GOR achieved a high $FE_{formate}$ of over 90% across a potential range from 1.22 to 1.48 $V_{RHE}$. With these well-designed electrodes, the co-electrolysis of $CO_2$ and glycerol, conducted in a flow cell, commenced electrolysis at a notably low onset potential of 1.05 V and achieved a current density of 100 mA $cm^{-2}$ at 1.97 V, resulting in approximately 20% energy savings compared to conventional OER coupled systems (Fig. 11a). Moreover, the assembled co-electrolysis system exhibited sustained electrolysis performance over 10 days, maintaining a current density exceeding 100 mA $cm^{-2}$ and product FEs of over 90% on both sides at 2.2 V, suggesting the robust stability of these prepared catalysts (Fig. 11b). This work underscores the practical potential for energy-saving and dual-value-added chemical production within the $CO_2$RR||GOR electrolysis system.

In addition to the GOR, coupling the $CO_2$RR with the MOR ($CO_2$RR||MOR) has been investigated extensively because MOR has low oxidation potential, a well-defined reaction pathway, predictable product formation, and a feasible way to achieve high selectivity for formate [64,65,102,114,115]. In these formate co-production electrolysis systems, the anodic MOR garners as much attention as the cathodic $CO_2$RR. In the initial phase of the proposed electrolysis system, Bi- and In-based cathodes and non-noble metal-based anodes were typically designed for the co-valorization of $CO_2$ and methanol in membrane-separated H-cells [102,114,119]. For instance, leveraging the unique characteristics of 2D materials, Cao et al. engineered two MOF-derived 2D catalysts for the $CO_2$RR||MOR. Their Ni-based MOF nanosheet arrays (Ni–NF-Af) designed for the MOR attained 100 mA $cm^{-2}$ at only 1.345 $V_{RHE}$, with a nearly 100% $FE_{formate}$ thanks to extensive coverage of the $Ni^{2+}/Ni^{3+}$ redox couple and faster proton diffusion capability. Additionally, their Bi-MOF-derived ultrathin bismuthenes (Bi-ene) for the $CO_2$RR exhibited a $FE_{formate}$ exceeding 96% at −0.9 $V_{RHE}$ [114]. Subsequently, a bipolar membrane-separated H-type cell was constructed with the two prepared electrodes, requiring only 2.13 V to drive 10 mA $cm^{-2}$ and achieving nearly 100% $FE_{formate}$ on both sides. This device demonstrated the feasibility of electrochemical formate production through coupling the $CO_2$RR with the MOR. Continuing along this trajectory, the performance of the $CO_2$RR||MOR electrolysis system has been further enhanced by subsequent endeavors in catalyst development and electrolyzer optimization [115,120]. Xia's research group, for example, refined the anodic MOR catalyst through the partial deligandation of Ni-MOF at 350 °C (Ni-MOF@350) [115]. This process preserved the porous structure, providing more accessible nickel sites for efficient mass transfer and conversion. The resulting catalyst delivered 100 mA $cm^{-2}$ with a $FE_{formate}$ of 98.4% thanks to the formation of Ni–OOH sites. Integrated with the Ni-MOF@350 for the MOR and Ni-MOF-derived Ni nanoparticles and single atoms anchored on N-doped carbon nanosheets (Ni&NiNC) for the $CO_2$RR in a zero-gap MEA device, an industry-scale current density of 500 mA $cm^{-2}$ was obtained at only 2.4 V and achieved superior selectivity, with $FE_{formate}$ and $FE_{CO}$ values above 90% in a voltage range from 1.7 to 2.2 V (Figs. 11c and d).

In the endeavor to minimize catalytic costs and streamline electrolysis devices, the utilization of bifunctional electrocatalysts has emerged as a promising approach for $CO_2$RR||MOR systems [64,121,122]. Illustratively, a CuSn alloy bifunctional catalyst showcased remarkable $CO_2$RR and methanol performance (Fig. 11e) [121]. On the cathode side, it demonstrated a formate formation rate of 2623 μmol $h^{-1}$ $cm^{-2}$ and an optimal $FE_{formate}$ of 87.3 % at −1.4 $V_{RHE}$. Simultaneously, on the anode side, the catalyst delivered 200 mA $cm^{-2}$ at 1.47 $V_{RHE}$, maintaining nearly 100% $FE_{formate}$ within the potential range of 1.4–2.0 $V_{RHE}$. The superior electrocatalytic performance was assigned to the unique hierarchical structure and synergistic contributions of the alloy components.

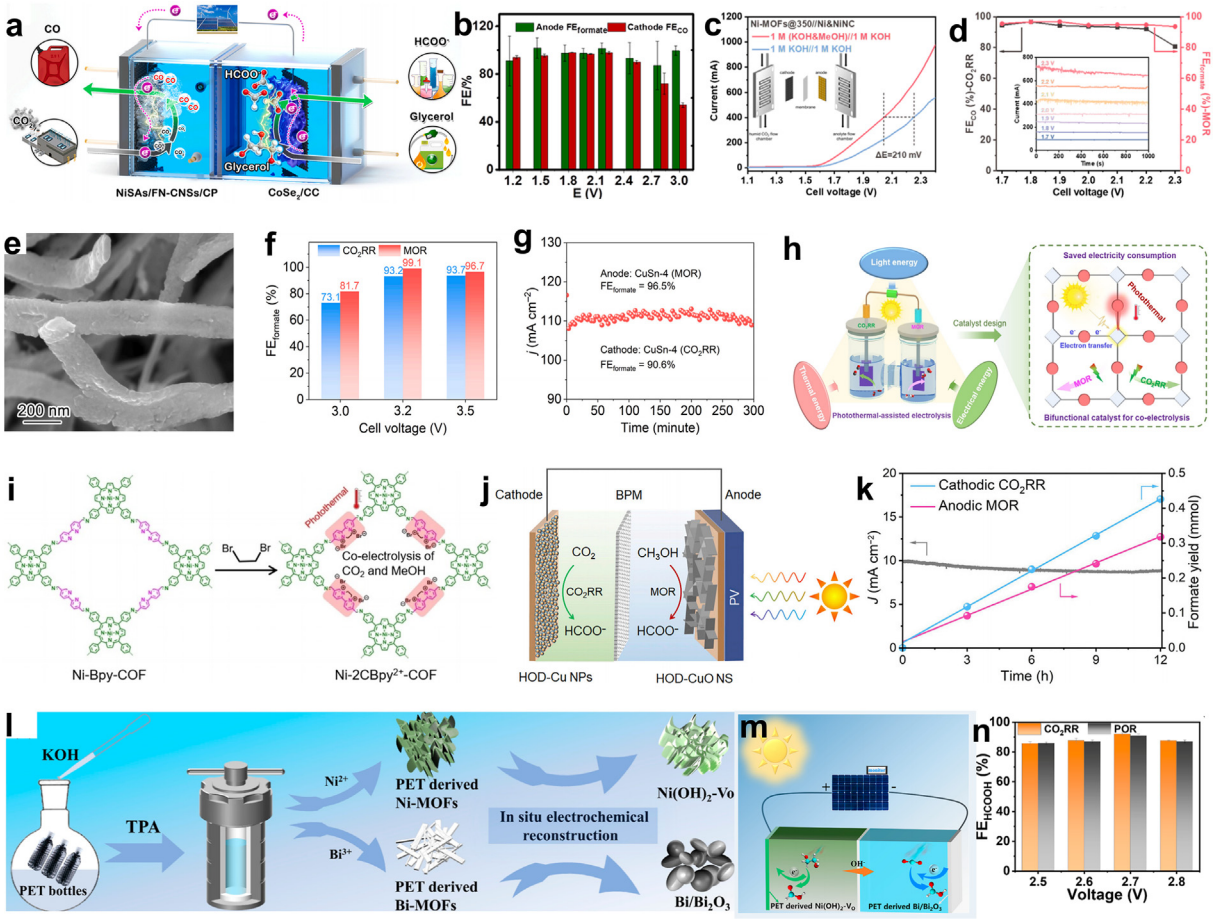


**Fig. 11.** (a) Schematic illustration of the $CO_2RR||GOR$ electrolysis system; (b) the $FE_{CO}$ and $FE_{formate}$ recorded at various cell potentials. Reproduced with permission from Ref. [112], Copyright 2022, Elsevier. (c) Polarization curves (IR-free; inset: MEA reactor) and (d) voltage-dependent selectivity of the $CO_2RR||MOR$ electrolysis system. Reproduced with permission from Ref. [115], Copyright 2023, American Chemical Society. (e) SEM images of CuSn-4 alloy nanowire. (f) Corresponding $FE_{formate}$ for $CO_2RR||MOR$ couple under different cell voltages. (g) Stability test of $CO_2RR$-MOR couple under a cell voltage of 3.2 V. Reproduced with permission from Ref. [121], Copyright 2022, Elsevier. (h) Schematic illustration of photothermal-assisted co-electrolysis of $CO_2$ and methanol. (i) Schematic of the preparation of Ni-2CBpy$^{2+}$-COF. Reproduced with permission from Ref. [64], Copyright 2022, Wiley-VCH. (j) Schematic of the solar-driven $CO_2RR||MOR$ device. (k) The stability of the bias-free solar-driven system and the corresponding formate yield with a reaction time of 12 h. Reproduced with permission from Ref. [65], Copyright 2022, Cell Press. (l) Schematic illustration of PET-derived catalysts. (m) Schematic of solar-powered $CO_2$ electrolysis coupled with PET upcycling. (n) $FE_{HCOOH}$ of PET-derived ethylene glycol oxidation reaction (POR) and $CO_2RR$ at different voltages. Reproduced with permission from Ref. [92], Copyright 2023, American Chemical Society.

Moreover, when the electrolysis system was equipped with the bifunctional electrode in a two-electrode setup for overall $CO_2$ and methanol co-valorization, it reached 100 mA cm$^{-2}$ at 3.32 V and maintained stable electrolysis for 300 min at a current density of over 110 mA cm$^{-2}$, with a $FE_{formate}$ of 90.6% and 96.5% towards the $CO_2RR$ and MOR, respectively (Figs. 11f and g). Elsewhere, a newly prepared bifunctional viologen-containing covalent organic framework (Ni-2CBpy$^{2+}$-COF) for $CO_2RR||MOR$ systems harvested photothermal energy to further reduce the overall electricity consumption for co-producing CO in the cathode and formate in the anode (Figs. 11h and i) [64]. The remarkable specificity of the catalyst derived from its cyclic diquats (2CBpy$^{2+}$), which had a viologen nature that accelerated charge transfer between the catalyst and immediate species, thereby generating a robust photothermal effect ($\Delta T = 49.1$ °C). This effect significantly enhanced the overall reaction kinetics. Such work provides an unusual strategy for these hybrid systems. Beyond catalyst optimization, concurrent advancements in electrolyzer design and the incorporation of auxiliary energy sources like light and heat have been reported to efficiently facilitate the co-electrolysis of $CO_2$ and methanol. A Cu-based electrocatalyst-catalyzed $CO_2RR||MOR$ electrolysis system showcased bias-free formate production on both sides by integrating the electrolyzer with a triple-junction GaInP/GaAs/Ge photovoltaic (PV) cell (Fig. 11j) [65]. The solar-assisted system achieved a short-circuit current of 10.8 mA cm$^{-2}$ and an open-circuit voltage of 2.48 V, resulting in a solar-to-formate (STF) conversion efficiency of 3.63%. Moreover, after a 12-h stability test at over 9 mA cm$^{-2}$, the $FE_{formate}$ values were 88% and 58% for the MOR and $CO_2RR$, respectively (Fig. 11k). Though still far from the requirements for practical application, these novel strategies provide valuable insights and reference points for the development of hybrid systems.

Aside from the widely investigated MOR and GOR, a series of studies confirmed the feasibility of integrating the upgrading of hydrolyzed ethylene glycol (EG) derived from poly(ethylene terephthalate) (PET) plastics into $CO_2$ electrolysis [92,123,124]. In these studies, Co- and Ni-based nanocatalysts were employed for the oxidation of EG, while Sn- and Bi-based nanocatalysts were utilized for the $CO_2RR$. This approach facilitated energy-efficient $CO_2$ electrolysis and the upcycling of PET plastics, resulting in concurrent formate production on both sides. Remarkably, in a recent study, both PET hydrolysates, namely terephthalic acid (TPA) and EG monomers, were fully used in a $CO_2$ hybrid electrolysis system [92]. In this system, PET-derived TPA served as the ligand for catalyst preparation on both sides, while EG acted as the reactant for the anodic upgrading reaction (Fig. 11l). The electrochemically restructured $Bi/Bi_2O_3$ obtained from PET-derived Bi-MOFs exhibited exceptional activity and selectivity for formate generation, achieving an impressive $FE_{formate}$ of 91% and a current density of −272 mA cm$^{-2}$ at

−1.4 $V_{RHE}$. The superior $CO_2RR$ performance was attributed to the interface electron transfer from $Bi_2O_3$ to Bi, which stabilized the high valence of Bi sites and optimized the adsorption of the OCHO* intermediate. Simultaneously, the oxygen-vacancy-rich $Ni(OH)_2$-$V_O$ obtained from PET-derived Ni-MOFs attained 300 mA $cm^{-2}$ at 1.6 $V_{RHE}$ with a $FE_{formate}$ of 86% in a PET hydralysate-containing KOH solution. This performance was assigned to the rich oxygen vacancy sites that facilitated the formation of $Ni^{3+}$ sites for the EG oxidation reaction. Furthermore, a solar-powered flow reactor equipped with the above two prepared electrodes reached approximately 100 mA $cm^{-2}$, with a total $FE_{formate}$ of 181% at 2.7 V (Figs. 11m and n). This endeavor fully utilizes renewable electricity and solar energy for the recycling of PET plastics and $CO_2$, serving as valuable guidance for subsequent research on electrocatalysts and related electrolytic devices.

The above remarkable progress in alcohol oxidation presents opportunities for practical applications and potentially industrial-scale implementation. However, it should be acknowledged that though the reported performance in laboratory settings seems to approach the requirements for industrial application, issues of unsatisfactory long-term stability, the rather large overpotentials of AORs, and the over-oxidation of alcohols into $CO_2$ at large current densities still need more in-depth studies, rather than researchers simply chasing novel catalysts that commonly present no obvious breakthrough in catalytic performance. Moreover, we need systematic studies to simulate industrial electrolysis and objectively demonstrate the feasibility of $CO_2RR||AOR$ electrolytic systems. In these electrolytic systems, the most cost-effective GOR may be selected as an OER alternative, and the cathodic reaction converting $CO_2$ into CO or formate may be the best because high-performance catalysts, electrode structures, and electrolyzers are readily available. With an explicit electrolytic system, industrial practice issues—including electrolytic effects, long-term stability, energy supply, production purification, economic feasibility, and other practical considerations—can then be explored one by one.

*4.1.2.2. Coupling the $CO_2RR$ with aldehyde oxidation reactions.* Aldehydes possessing an active aldehyde group exhibit comparatively low theoretical oxidation potentials and are readily converted into their corresponding acids [53,63,125]. When contemplating the economic advantages of both reactants and products holistically, integrating certain aldehyde oxidation reactions with the $CO_2RR$ can effectively accomplish the objective of dual-value-added production with reduced energy consumption. Biomass-derived 5-hydroxymethylfurfural (HMF) is one of the most important renewable platform chemicals, and it can be used to prepare numerous fine chemicals [125]. Thus, converting HMF into the top-value biobased molecule 2,5-furandicarboxylic acid (FDCA) via the electrochemical HMF oxidation reaction (HMFOR) has attracted enormous interest for its green synthesis pathway, highly valuable products, and rather low theoretical oxidation potential for FDCA production, which was extensively integrated into water splitting to achieve $H_2$ production and biomass valorization [31,125,126]. The HMFOR is currently the hottest focus of biomass molecule oxidation reaction studies in water hybrid systems, and several studies have also confirmed the feasibility of coupling the HMFOR with a $CO_2$ electrolysis system ($CO_2RR||HMFOR$). Efforts related to these coupled systems have been devoted to developing catalysts for efficient HMF conversion into FDCA and satisfactory selectivity of the $CO_2RR$. Catalysts tailored for the system comprise anodic Ni-based materials for the HMFOR [127–130], cathodic single-atom-based catalysts, molecular catalysts facilitating both reactions [127,131], and bifunctional catalysts proficient in both reaction pathways [53,132]. The reaction mechanism of Ni-based catalysts for the HMFOR was carefully investigated in a near-neutral electrolyte to match the cathodic $CO_2$ reaction environment [128]. In a $CO_2$-saturated 0.5 M $KHCO_3$ electrolyte, prepared 5 nm nickel oxide nanoparticles (NiO NPs) initiated the HMFOR at 1.53 $V_{RHE}$ with a $FE_{FDCA}$ of approximately 30%. The HFMOR occurred through the 2,5-diformylfuran (DFF) intermediate formation pathway, accompanied by the redox-active cycle between $Ni(OH)_2$ and NiOOH on the surface of the NiO NPs. The conceptual $CO_2RR||HMFOR$ assembled in near-neutral electrolytes confirmed its feasibility for co-producing valuable products (biomass conversion FE of 36% and $FE_{formate}$ of 81% at 2 mA $cm^{-2}$).

The subpar performance of the above electrolysis system prompted a sequence of studies aimed at optimization. Subsequently, a paired electrolysis system was developed, incorporating a highly active single Cu atom-doped Bi ($Cu_1Bi$) catalyst for the $CO_2RR$ and NiCo layer-doubled hydroxides (NiCo LDHs) for HMFOR. This optimized configuration demonstrated remarkable co-production of FDCA (with a $FE_{FDCA}$ of ~80%) and formate (with a $FE_{formate}$ of ~90%) at a voltage of 2.7 V and a current density of 237 mA $cm^{-2}$ (Figs. 12a and b) [131]. Significantly, this voltage was 0.8 V lower than that required for conventional $CO_2$ electrolysis, reducing the electricity input for formate production by 22.9%. The exceptional $CO_2RR$ performance of $Cu_1Bi$ can be attributed to the doped Cu single atoms, which efficiently sped up the water dissociation process and facilitated the protonation step for formate generation (Fig. 12c). Bifunctional catalysts without active Ni components were also found to be suitable for this paired system [53]. Zhang et al. engineered an oxygen-vacancy-rich indium oxyhydroxide (InOOH-$O_V$) bifunctional catalyst that demonstrated remarkable selectivity in both reactions, achieving a $FE_{formate}$ of 92.6% for $CO_2$-to-formate and a $FE_{FDCA}$ of 90.7% for the HMFOR. An integrated cell using InOOH-$O_V$ as both cathode and anode produced an anodic FDCA yield of 87.5% and a cathodic $FE_{formate}$ of around 90.0% at 2.27 V (Figs. 12d and e). The charge redistribution and lattice distortion caused by the introduced $O_V$ sites in InOOH-$O_V$ optimized adsorption and the activation of the reaction processes, thereby leading to superior bifunctional activities (Fig. 12f).

Researchers are constantly chasing the goal of high selectivity for multicarbon products via $CO_2$ electrolysis at low potentials. The recently proposed $CO_2RR||HMFOR$ electrolytic system achieves highly efficient co-production of multicarbon products and FDCA catalyzed by a bifunctional Cu-based electrode (Fig. 12g) [132]. The Cu-based electrode was prepared by chemically oxidizing the Cu foam surface into a CuO nanoflower, and the surface CuO nanoflower then underwent quick reduction, forming the final CuO–NF@Cu electrode (Fig. 12h). The prepared catalyst for $CO_2$ conversion into $C_2H_4$ attained a $FE_{C_2H_4}$ of 70% with a current density of 104.5 mA $cm^{-2}$ at −0.95 $V_{RHE}$, and simultaneously delivered a $FE_{FDCA}$ of 99.3% for the HMFOR at 1.62 $V_{RHE}$. In a setup with the bifunctional CuO–NF@Cu catalyst, the coupled system delivered 188.8 mA $cm^{-2}$ at 2.75 V, with impressive results for the $FE_{C_2H_4}$ (96.6%) and $FE_{FDCA}$ (74.5%) during 5 h of testing (Fig. 12i). The above research indicates that the performance of $CO_2RR||HMFOR$ electrolytic systems can be greatly improved via catalyst design; however, the stability of this kind of system requires more attention because of the instability of the HMF and its FDCA products in an alkaline environment.

In addition to the well-known HMFOR, the single-electron transfer formaldehyde oxidation reaction (FOR) with concurrent formate and $H_2$ production, which has rather low thermodynamic equilibrium potential, has been incorporated into $CO_2$ hybrid electrolysis [63,133]. In these systems, various catalysts have achieved the anodic production of formate and $H_2$ alongside the cathodic production of CO or formate. Impressively, the co-production of formate with an overall $FE_{formate}$ exceeding 180% at a fairly low cell potential (1.05 V) was achieved in a hybrid system equipped with a well-designed BiOCl cathode for the $CO_2RR$ and a $Cu_2O$ electrode for the anodic FOR in a H-type cell [63]. The cell voltage and current density were further improved when the reactions took place in a flow cell or MEA cell. In the MEA cell, 100 mA $cm^{-2}$ was achieved at 0.86 V, with a total $FE_{formate}$ of over 90%. However, setting aside effects from the $CO_2RR$ side, interference in the anodic FOR from the Cannizzaro reaction in a strongly alkaline solution creates

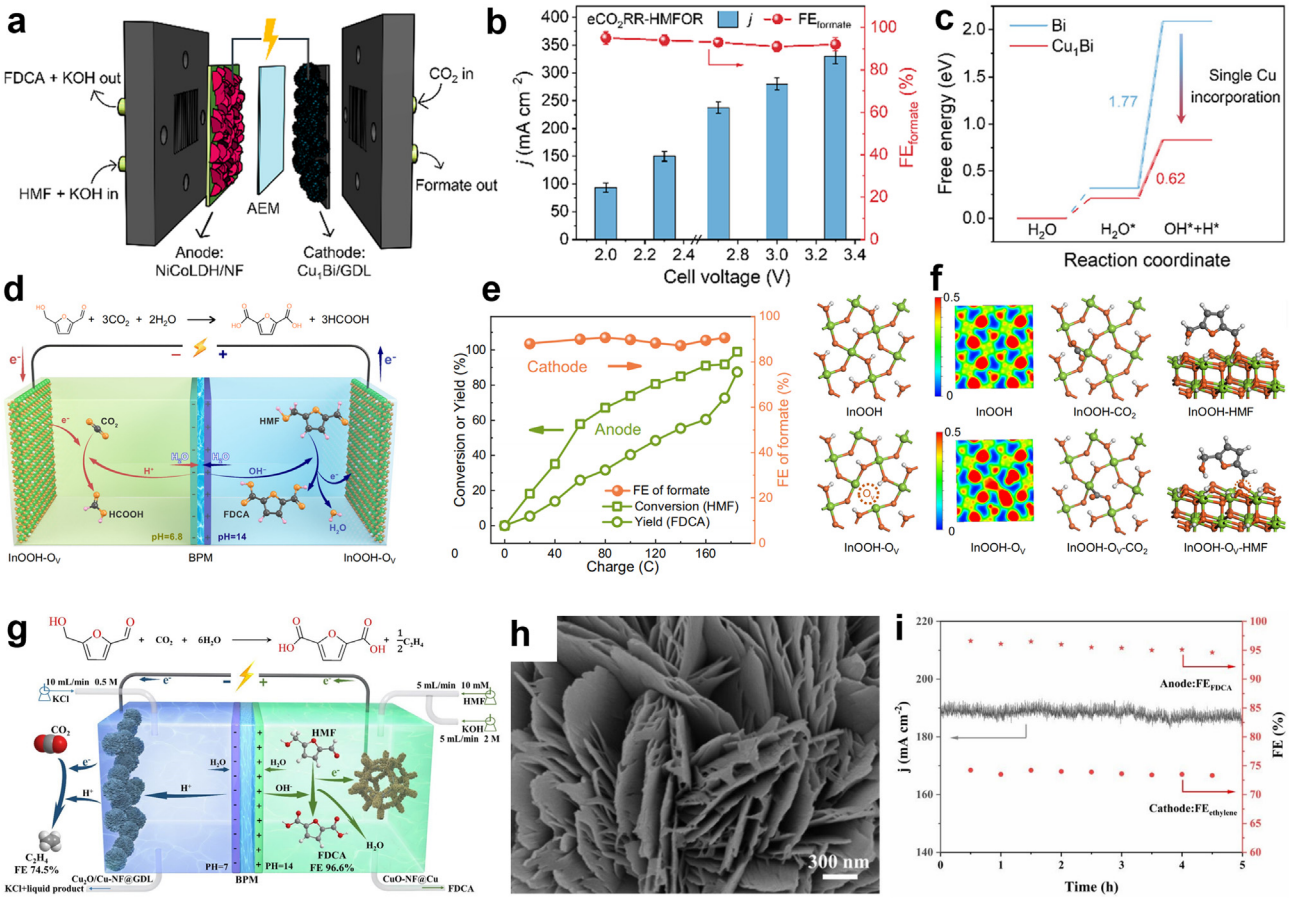


**Fig. 12.** (a) Schematic of the coupled $CO_2$RR-HMFOR system in the MEA setup. (b) Current density and $FE_{formate}$ as a function of cell voltage. (c) Gibbs free energy diagrams for the $H_2O$ dissociation process on Bi and $Cu_1Bi$ surfaces. Reproduced from Ref. [131], with permission from the Royal Society of Chemistry, Copyright 2023. (d) Integrated electrolysis cell coupling $CO_2$RR with HMFOR. (e) HMF conversion, FDCA yield, and $FE_{formate}$ in the integrated cell. (f) Diagrams (top view) of built models of InOOH and InOOH-$O_V$ and their corresponding electron localization function (ELF), and the adsorption configurations of $CO_2$ and HMF. Reproduced from Ref. [53] with permission from Springer Nature, Copyright 2023. (g) Schematic illustration of $CO_2$RR||HMFOR in a flow cell; (h) high-magnification SEM of CuO–NF@Cu; (i) stability test of the $CO_2$RR||HMFOR coupled reaction under a cell voltage of 2.75 V. Reproduced from Ref. [132] with permission from the Royal Society of Chemistry, Copyright 2023.

difficulties for analyzing products, and the low formate yield at the anode also reduces the economic benefits of conducting the FOR in $CO_2$ hybrid electrolysis.

*4.1.2.3. Coupling the $CO_2$RR with other organic oxidation reactions.* Some novel, infrequent oxidation reactions in the $CO_2$ hybrid electrolysis system have been reported, confirming the flexible and diverse application of the $CO_2$ hybrid electrolysis system in dual electrosynthesis [46,103,134–136]. Generally, these less investigated hybrid systems are conceptual and verified by the targeted design of catalysts for one side or both sides. Electrocatalysts for the $CO_2$RR were also the focus of these works. A pioneering hybrid system coupling the $CO_2$RR with the oxidative polymerization of Levodopa (L-DOPA) was proposed by Ma et al. [103], who carried this out using a well-designed bifunctional electrocatalyst comprising twelve-azido-group-bearing nickel phthalocyanine ($N_3$NiPc) anchored on CNT ($N_3$NiPc-CNT). The $N_3$NiPc-CNT presented excellent $CO_2$RR performance with nearly unity selectivity for CO production in a wide potential range, and impressive activity, which was attributed to the synergistic effects from the single-molecule active centers, good electronic conductivity, and amine groups formed *in situ* on the catalyst, which offered extra active sites for adsorbing $CO_2$. The $N_3$NiPc-CNT also presented superior activity for promoting the oxidative polymerization of L-DOPA to a porous 3D polymer nano-framework at a low potential. When $N_3$NiPc-CNT was assembled in a two-electrode electrolyzer, only 1.05 V was required to reach 10 mA $cm^{-2}$, simultaneously obtaining the porous 3D polymer nano-framework in the anode and 100% selectivity for CO production in the cathode.

Elsewhere, Zhang et al. innovatively integrated the $CO_2$RR with the electrooxidation of octylamine to octanenitrile, yielding an eco-friendly way to synthesize an important intermediate for the fields of medicine and pesticides. In their research, $In_2O_3$ was chosen as the model catalyst for the $CO_2$RR to elucidate potential reconstruction behaviors (Figs. 13a and b) [134]. The study validated that crystalline $In_2O_3$ underwent *in situ* evolution, transforming into a heterostructure composed of crystalline In and amorphous $In_2O_{3-x}$ (In/$In_2O_{3-x}$) (Fig. 13c). Within this heterostructure, the rectification of electron-rich In by the Schottky effect played a pivotal role, contributing to a favorable performance that featured an impressive $FE_{formate}$ of ~89.2% (Fig. 13d). Subsequently, the devised hybrid system employed the meticulously examined In/$In_2O_{3-x}$ catalyst for the $CO_2$RR and a $Ni_2P$ nanosheets array for the octylamine oxidation reaction (OOR) (Fig. 13e). This configuration yielded formate in the cathode and octanenitrile with a FE of 98% in the anode at a cell voltage ~200 mV lower than in conventional $CO_2$ electrolysis (Fig. 13f). In another study, the electrochemical semi-dehydrogenation of tetrahydroisoquinoline (THIQs) into dihydroisoquinoline (DHIQs)—which is a friendly way to produce highly valuable DHIQs in the pharmaceutical industry—was used to promote $CO_2$ electrolysis. A 3D Bi-based MOF (V12) modified on Bi foil via electrodeposition (V12e) was prepared for the $CO_2$RR, delivering a current density of 11.78 mA $cm^{-2}$ with a high $FE_{formate}$ of 93.2% at −0.9 $V_{RHE}$ (Fig. 13g) [136]. The good $CO_2$RR

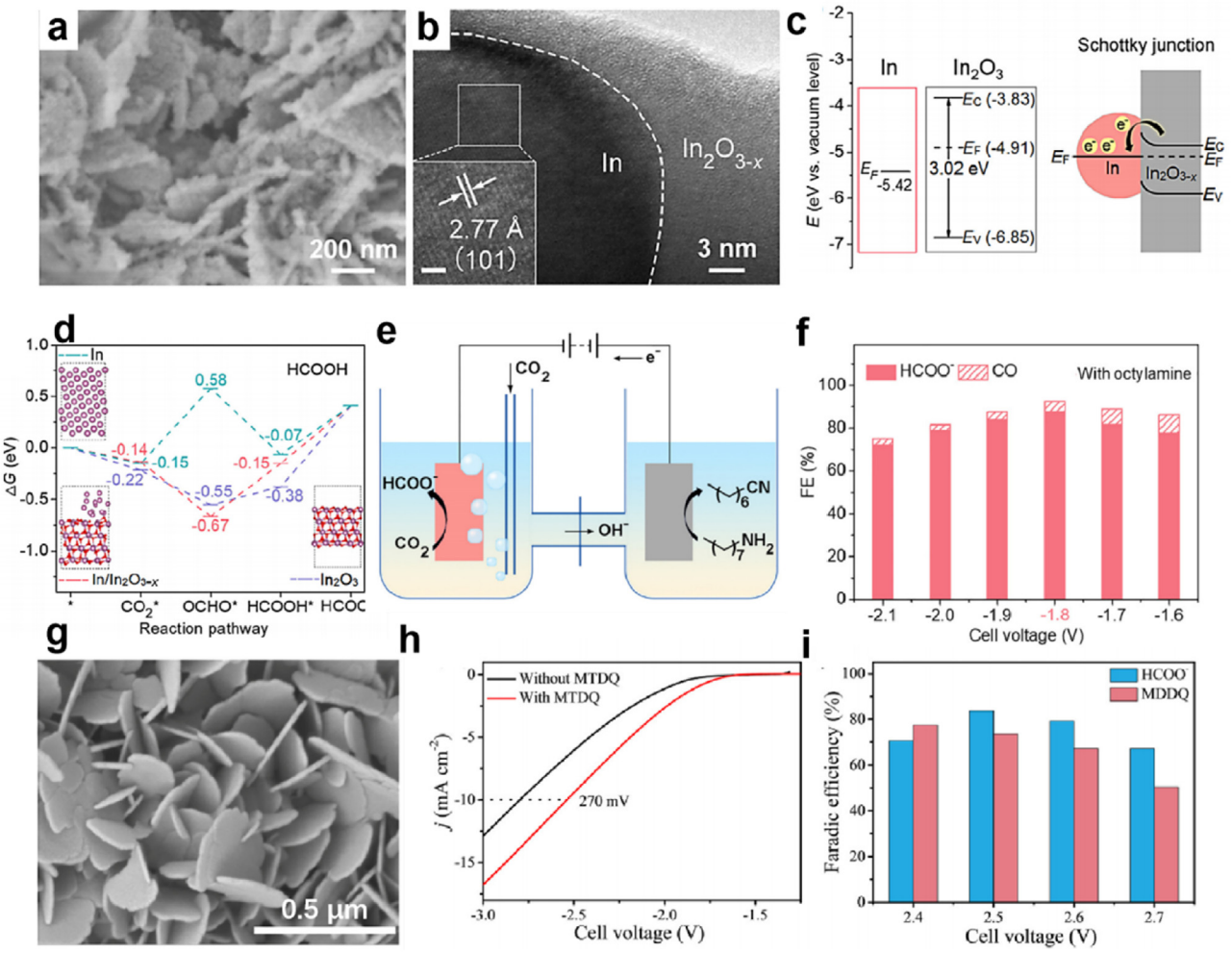


**Fig. 13.** (a) SEM and (b) HRTEM images of In/$In_2O_{3-x}$. (c) Band structures of metallic In and $In_2O_3$, and a schematic illustration of In/$In_2O_{3-x}$ Schottky junction (EF, Fermi level; EV, valence band; EC, conduction band). (d) Calculated Gibbs free energy diagrams for producing formate over In, In/$In_2O_{3-x}$, and $In_2O_3$ (pink ball: In atom; red ball: O atom). (e) Schematic illustration of integrating $CO_2$RR with OOR in an In/$In_2O_{3-x}$||$Ni_2P$ electrolyzer. (f) FEs at various cell voltages of the two-electrode electrolyzer with octylamine in the anodic chamber. Reproduced from Ref. [134] with permission from Elsevier, Copyright 2020. (g) SEM image of V12e; (h) LSV curves; (i) $FE_{formate}$ and FE of MDDQ of V12e||CAT-1@NF in 0.5 M $KHCO_3$; MDDQ: 1-methyl-3,4-dihydroisoquinoline. Reproduced from Ref. [136] with permission from Elsevier, Copyright 2021.

performance was attributed to the improved charge transfer rate and introduced structural defects caused by electrodeposition. The hybrid electrolysis system was driven by a prepared V12e electrode for the $CO_2$RR and a Ni-MOF-modified Ni foam (CAT-1@NF) for the anodic semi-dehydrogenation reaction of a model tetrahydroisoquinoline, i.e., 1-methyl-1,2,3,4-tetrahydroisoquinoline (MTDQ); a cell voltage of 2.52 V was required to reach 10 mA $cm^{-2}$, 270 mV lower than the conventional $CO_2$ electrolysis system, and product FEs of over 70% in both sides were attained in a potential range of 2.4–2.6 V (Figs. 13h and i). In short, the above innovative conceptual $CO_2$ hybrid electrolysis systems can serve as a rich source of ideas for further enhancing such hybrid systems by flexibly matching reaction pairs.

### *4.2. Coupling the CO reduction reaction with alternative oxidation reactions*

Converting $CO_2$ into multicarbon ($C_{2+}$) products via the $CO_2$RR not only facilitates the storage of renewable energy within chemical bonds but also offers a means to replace fossil-based chemical feedstocks [48, 57]. However, the strong alkaline environment commonly used to promote C–C bond coupling poses several challenges: low $CO_2$ utilization, poor stability caused by the formation of carbonate, and pH drift [141, 142]. With the rapid maturity of the $CO_2$ to CO conversion process, using the carbon monoxide reduction reaction (CORR) as the downstream reaction in tandem with the $CO_2$RR has unique advantages over direct $CO_2$ reduction, bypassing issues arising from $CO_2$ directly reacting with hydroxide. Similar to the $CO_2$RR, the anodic OER in CO electrolysis consumes a large amount of electric energy in the overall CO electrolysis process. Replacing the OER with these value-added alternative reactions in CO electrolysis can promote the production efficiency of $C_{2+}$ products and yield valuable products at the anode (Table 3) [57,140]. Capitalizing on the unique advantages of low cost, abundant availability, and the generation of value-added oxidized products, glycerol oxidation was integrated with the CORR (CORR||GOR) under strong alkaline anodic conditions within a MEA cell [140]. In this configured MEA cell, Cu nanoparticles with sizes less than 50 nm and coated on the GDL functioned as the cathode for converting $CO_2$ into $C_{2+}$ products (i.e., $C_2H_4$, $C_2H_6O$, $C_3H_8O$) (Fig. 14a), while Pt nanoparticles with sizes smaller than 5 nm and supported on a hydrophilic carbon cloth substrate (Pt-CC) acted as the anode for converting glycerol into $C_3$ products (i.e., lactic acid and glyceric acid) (Fig. 14b). The assembled MEA presented excellent selectivity on both sides of the cell, achieving a cathodic $FE_{C2+}$ of 71% and an anodic $FE_{C3}$ of 75% at 180 mA $cm^{-2}$ and 1.34 V, which reduced the cell voltage by over 1 V within the tested current density range and saved 55% energy compared to conventional CO electrolysis for producing $C_2H_4$ (Fig. 14c). The hierarchically structured hydrophilic Pt-CC anode

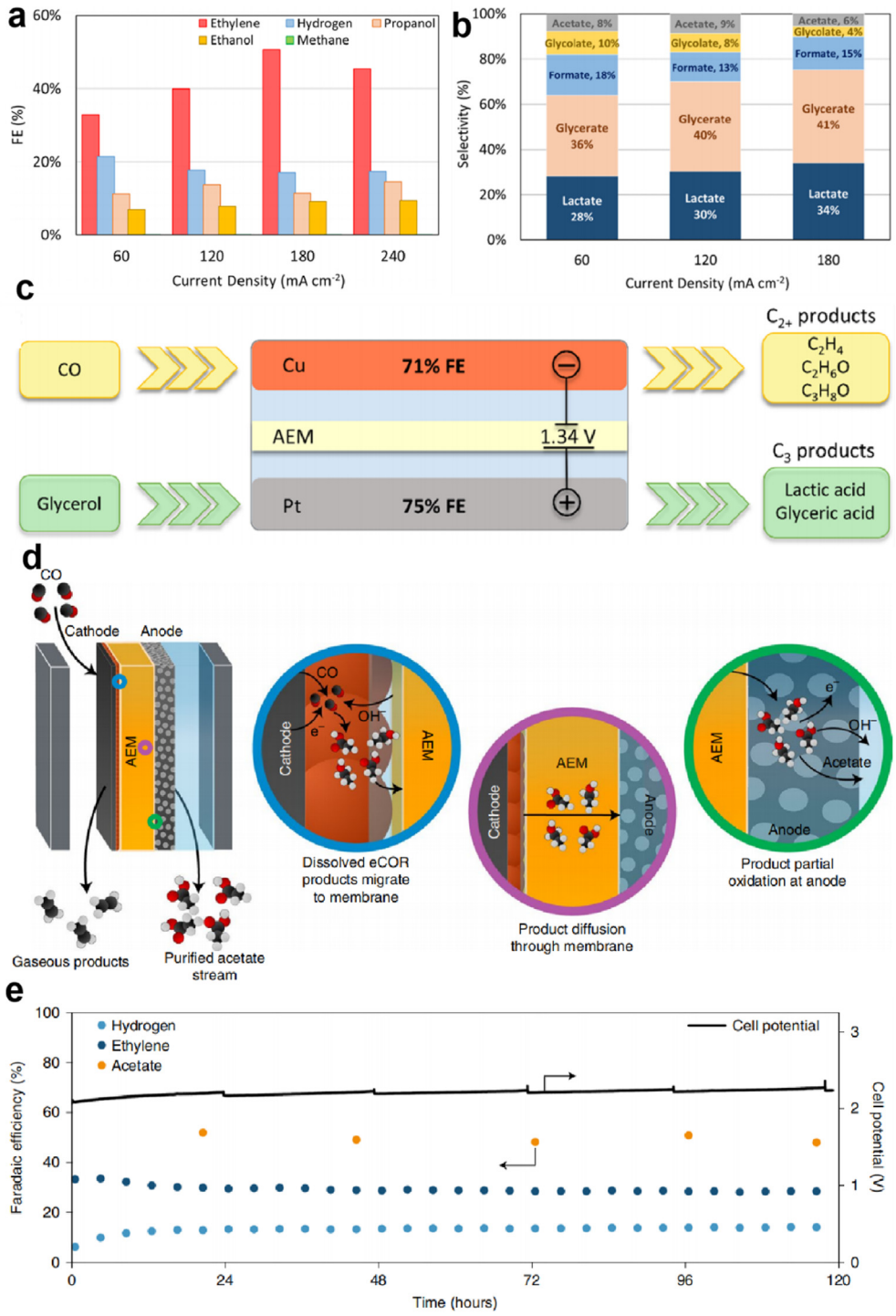


**Fig. 14.** (a) Selectivity of the cathodic products for a CORR||GOR system at different current densities in anolyte containing 2.0 M KOH + 4.0 M glycerol solution. (b) Selectivity of anodic products at different current densities in CORR||GOR system using Pt-CC electrode. (c) Schematic of the CORR||GOR system inputs and outputs for simultaneous production of $C_2$ and $C_3$ streams. Reproduced from Ref. [140] with permission from the American Chemical Society, Copyright 2021. (d) Schematic of the CO electrolyzer design in a MEA configuration using a permeable AEM to produce a concentrated acetate stream in the anolyte chamber. (e) Performance of COR system. Reproduced from Ref. [57] with permission from Springer Nature, Copyright 2022.

played a pivotal role in expediting the kinetics of the GOR by mitigating both mass and charge transfer resistances. This work provides a useful reference for the practical application prospects of the CORR||GOR coupled system.

OER alternatives are not limited to the oxidation of externally introduced compounds; the products formed in the cathode can be transported to the anode for the oxidation reaction [57,143]. Jiao et al. constructed an internally coupled CO electrolysis system in which a commercial Cu-based GDL and a Ni–Fe mixed oxide electrodeposited on Ni foam ($NiFeO_x$/Ni foam) served as the cathode and anode, respectively, and an alkaline-stable anion exchange membrane was used to allow the transport of cathode-produced ethanol to the anode for a partial oxidation reaction to produce acetate (Fig. 14d) [57]. The assembled MEA electrolyzer with an internal tandem process efficiently converted CO into $C_2H_4$ and ethanol at

the cathode, and then the ethanol generated was transported into the anode and internally converted into acetate. The cell sustained stable electrolysis for 120 h of continuous operation at a current density of 200 mA $cm^{-2}$ and a cell voltage below 2.3 V. Throughout this period, it consistently generated a 1.9 M acetate product stream in the anodic chamber, boasting a purity of 97.7% in 3 M KOH anolyte (Fig. 14e). The acetate concentration was further elevated to 7.6 M with a purity of over 99% in 7 M KOH anolyte. Technoeconomic analysis revealed that maintaining a highly concentrated liquid product stream, with no less than 5 M acetate, is crucial for minimizing the energy consumption associated with product separation. Therefore, this work provides insightful guidance for achieving economically advantageous $CO_2$ and CO electrolysis, particularly with respect to membrane and anodic electrocatalysts. The aforementioned CO hybrid electrolysis methods have laid the groundwork for research into the energy-efficient electrosynthesis of multicarbon chemicals.

### 4.3. Coupling the 2e⁻ORR with OER-alternative oxidation reactions

The electrochemical 2e⁻ORR ($E^{\theta}$ = 0.69 $V_{RHE}$) provides a more renewable and greener alternative pathway to produce $H_2O_2$ compared with the energy-intensive and contaminative anthraquinone (AQ) process [49,144,145]. Furthermore, this $H_2O_2$ electrosynthesis method facilitates carbon-free, small-scale, and continuous production of $H_2O_2$, enabling its on-site application in sterilization and waste degradation, and as a redox mediator for synthesizing other chemicals [146,147]. Owing to the unfavorable thermodynamics compared with the 4e⁻ORR, numerous research studies have been devoted to developing highly active and selective electrocatalysts for the 2e⁻ORR. Those to date have mainly focused on metal-free carbon-based materials, single-atom catalysts, alloys, oxides, and hybrids of carbon and metal nanocatalysts [144–146,148,149]. Facilitated by optimized catalysts, $H_2O_2$ production via the 2e⁻ORR has reached a high selectivity of over 90% at a current density exceeding 100 mA $cm^{-2}$. Typically, the sacrificial OER is paired with the 2e⁻ORR in the $H_2O_2$ synthesis process, suggesting the potential to further upgrade economic benefits by replacing the OER with other value-added oxidative reactions. Among these alternatives to the OER, the 2e⁻WOR with $H_2O_2$ production [49,148,149] emerges as an ideal option for pairing with the 2e⁻ORR (2e⁻ORR||2e⁻WOR) because such a paired cell can theoretically double the $H_2O_2$ yield without necessitating external oxidative reactants. Nevertheless, the relatively high theoretical oxidation potential and competitive $4e^-$ and $1e^-$ pathways make it a formidable challenge to explore highly selective and active electrocatalysts for the 2e⁻WOR. Researchers in this field are thus actively exploring efficient electrocatalysts for the 2e⁻ORR||2e⁻WOR electrolysis system, and numerous catalysts or even bifunctional catalysts have been investigated for the 2e⁻ORR or 2e⁻WOR, greatly enhancing the efficiency of the $H_2O_2$ production process [49,145,148–153]. For instance, a nickel single-atom-doped $TiO_2$ ($Ni_xTi_{1-x}O_{2-y}$, $0.08 < x < 0.13$) designed for the 2e⁻WOR [49] presented excellent activity and selectivity toward $H_2O_2$ production. The optimized $Ni_{0.13}Ti_{0.87}O_{2-y}$ achieved a current density exceeding 300 mA $cm^{-2}$ and an FE of over 70% at 3.0 $V_{RHE}$ (Fig. 15a) in an electrolyte comprising 0.5 M $KHCO_3$ and 3.5 M $K_2CO_3$. The superior selectivity of $Ni_{0.13}Ti_{0.87}O_{2-y}$ with an optimal Ni ratio was attributed to doped Ni atoms that enabled lower *OH adsorption energy ($\Delta G_{*OH}$) and regulated it for proper $H_2O_2$ formation (Fig. 15b). A flow cell device coupling the 2e⁻WOR catalyzed by $Ni_{0.13}Ti_{0.87}O_{2-y}$ at the anode with the 2e⁻ORR catalyzed by oxidized carbon nanotubes (O-CNT) at the cathode was assembled for $H_2O_2$ electrosynthesis. The paired electrolyzer attained an overall $FE_{H_2O_2}$ of 146% (71% for the 2e⁻WOR and 75% for the 2e⁻ORR) at 240 mA and 3 V, demonstrating consistent performance over seven cycles (Figs. 15c and d). The economic evaluation indicated the optimized paired cell achieved an $H_2O_2$ production cost of $0.309/kg and required lower energy than the typical anthraquinone process, affirming the promising prospects of this strategy.

In some other works, metal oxides were designed as bifunctional electrocatalysts for efficient $H_2O_2$ electrosynthesis paired systems via regulating crystal facets [149] and introducing defects [148]. A plasma-induced defective $TiO_{2-x}$ with rich oxygen vacancies (OVs) [148] demonstrated improved current density and selectivity compared to pristine $TiO_2$ on both sides, with a peak $FE_{H_2O_2}$ of nearly 55% at 2.1 V for the 2e⁻WOR and over 90% across the tested potential range of 0.2–0.6 V for the 2e⁻ORR. The improved 2e⁻ORR performance was attributed to the OVs located within the inner atomic layer, while the enhanced 2e⁻WOR performance was linked to surface lattice distortion. Equipped with these bifunctional electrodes, the two-electrode electrolyzer attained a current density of 40 mA at a cell voltage of only 2 V, yielding an overall $FE_{H_2O_2}$ of 134% and a production rate of approximately 22.5 mmol $L^{-1}$ (Figs. 15e and f). This work provides valuable insights for designing novel catalysts in 2e⁻ORR||2e⁻WOR systems, encouraging further optimization of $H_2O_2$ electrosynthesis.

Apart from the significant advancements in double $H_2O_2$ production systems, the co-production of $H_2O_2$ alongside other valuable chemicals such as NaClO [152], $I_2$ [151], and formate [145,150] was achieved in 2e⁻ORR-involved hybrid electrolysis systems. These co-produced substances were utilized on site for degradation processes and the synthesis of additional chemicals. Remarkably, an electrolysis system coupling the 2e⁻ORR with PET plastic upcycling (2e⁻ORR||PET upcycling) achieved an industrial-scale current density of 400 mA $cm^{-2}$ at an ultralow cell potential of 0.927 V with co-production of $H_2O_2$ and formate (Figs. 15g and h) [145]. In the 2e⁻ORR||PET upcycling electrolysis system, a Ni–Mn bimetal catalyst achieved by selenizing a Ni–Mn bimetallic organic framework supported on Ni foam ($Ni_1Mn_1$-MOF-Se/NF) efficiently catalyzed the oxidation of ethylene glycol derived from PET decomposition; the NiOOH formed *in situ* and the synergistic effect of Mn and Se contributed to superior performance, while at the cathode, B, N co-doped onion carbon (B/N-onion carbon) selectively catalyzed $O_2$ conversion into $H_2O_2$ with a peak $FE_{H_2O_2}$ of 97.5% at 0.4 $V_{RHE}$, where the introduced B and N benefited the formation and stabilization of crucial OOH* intermediates for $H_2O_2$ production. Furthermore, the $H_2O_2$ generated within the electrolyte underwent additional refinement through the implementation of two subsequent pathways aimed at converting $H_2O_2$ into sodium perborate and dibenzoyl peroxide. Technoeconomic analysis revealed the energy-efficient and profitable advantages of the 2e⁻ORR||PET upcycling configuration over both coupling the HER with PET upcycling and using the conventional approach of coupling the ORR with the OER (Fig. 15i). This study presented a useful strategy for the energy-saving pairing of $H_2O_2$ electrosynthesis and downstream application.

The above research has generated a blueprint for the energy-saving and environmentally friendly production of $H_2O_2$, along with its on-site application. The potential of future $H_2O_2$ electrosynthesis holds promise for industrial implementation. Nevertheless, these coupling strategies are currently at the conceptual stage, presenting challenges when it comes to achieving reasonable stability and conversion efficiency with the coupled configurations (Table 4). The separation and purification of the thermodynamically unstable $H_2O_2$ also present obstacles. Attention at the present research stage needs to be directed towards applying $H_2O_2$ on site, screening the anodic oxidation reactions, and optimizing the catalytic performance of catalysts, especially for OER alternatives, to ensure the long-term stability of the electrolysis system. Efforts should also be focused on optimizing economic feasibility and scaling up $H_2O_2$ production.

### 4.4. Coupling the NRR with OER-alternative reactions

Ammonia ($NH_3$) is a crucial nitrogen resource that plays an essential role in both nature and human society, particularly in the industrial and agricultural sectors. Industrial $NH_3$ production is achieved via the Haber–Bosch process, but it suffers from high energy consumption, a considerable carbon footprint, and harsh operating conditions [154,155]. Consequently, there is a growing interest in developing the electrosynthesis of $NH_3$ through the nitrogen or nitrate reduction reaction (NRR ($N_2$RR and $NO_3^-$RR)), due to the promising prospects for

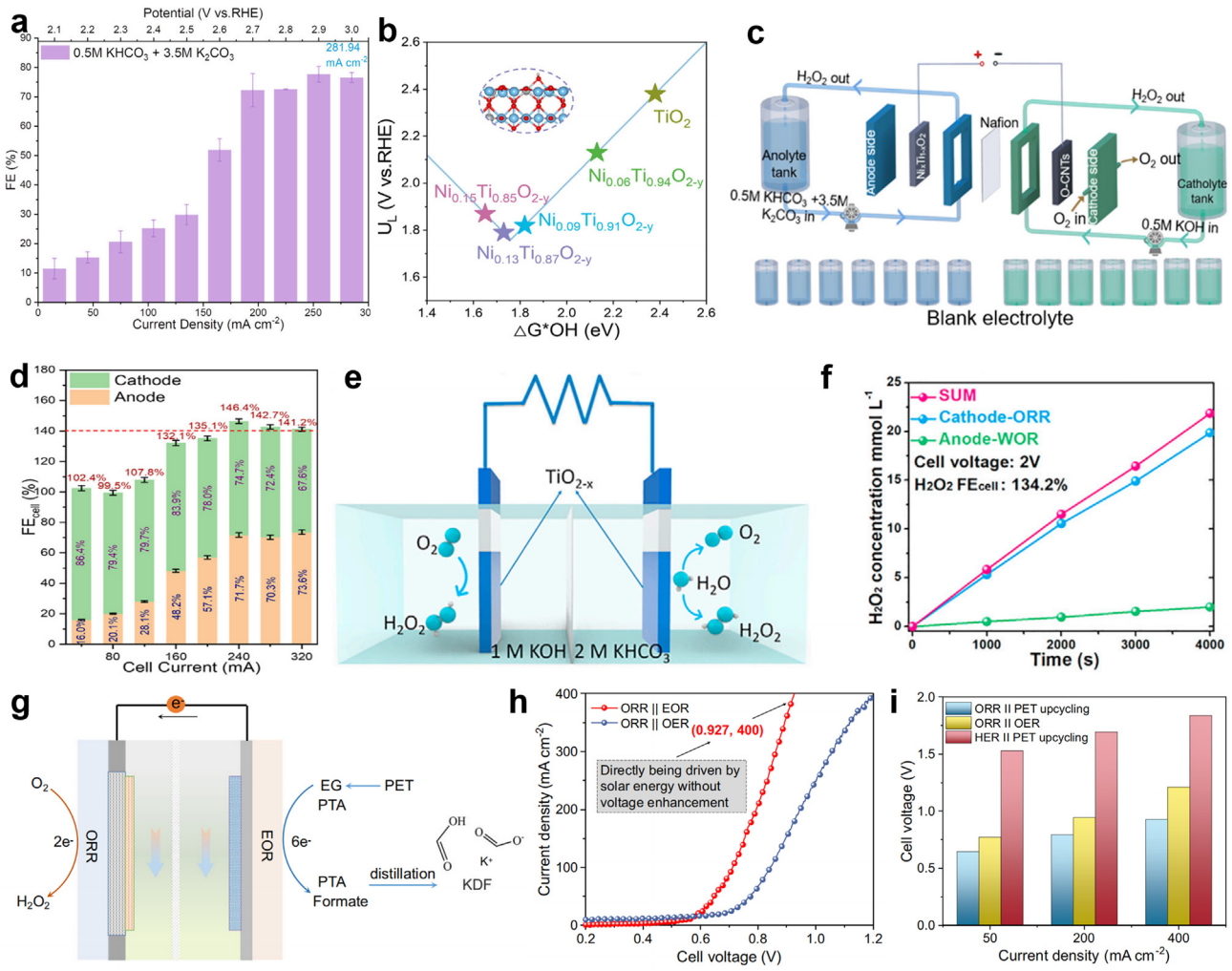


**Fig. 15.** (a) Potential and current-dependent FE for $H_2O_2$ production. (b) OH desorption potential and $U_L$ values vs. calculated $_{\Delta}G_{*OH}$ on the $Ni_xTi_{1-x}O_{2-y}$ catalysts. $U_L$ is defined as the limiting potential at which the electrochemical reaction spontaneously occurs. (c) Schematic illustration of electrochemical $H_2O_2$ production through coupling $2e^-$ORR and $2e^-$WOR in one full flow cell device. (d) FE values for $H_2O_2$ synthesis in the full cell. Reproduced with permission from Ref. [49], Copyright 2023, Cell Press. (e) Schematic illustration of electrochemical $2e^-$ORR||$2e^-$WOR coupling cell for $H_2O_2$ generation. (f) $H_2O_2$ yield rates in the electrode cell. Reproduced with permission from Ref. [148], Copyright 2023, Cell Press. (g) Schematic illustration of the electrosynthesis system $2e^-$ORR||PET upcycling. (h) Comparison of the polarization curves between the ORR||EOR system and the ORR||OER system (with iR compensation, compensating resistance: 5.6 ± 0.3 Ω). (i) Potential-dependent and current-dependent $FE_{H_2O_2}$. Reproduced from Ref. [145] with permission from Springer Nature, Copyright 2023.

sustainable production [11,14]. It is similar to the aforementioned reduction reactions, except for the significant requirement for both activity and selectivity in cathodic catalysts; the conventionally paired OER at the anode similarly hinders the overall reaction rate and substantially elevates the energy consumption for NRR electrolysis, thereby resulting in increased economic costs. In recent years, with continual improvement in the cathodic $NH_3$ production rate, there has been increasing attention upon reducing the overall cell voltage for the NRR by incorporating OER alternatives. Consequently, several hybrid electrolysis systems involving the NRR have emerged, achieving both energy-saving and dual-value-added production. In the following section, recent advances in hybrid electrolysis systems coupling the NRR with OER alternatives will be outlined to provide comprehensive strategies aimed at promoting more economically and energy-efficient $NH_3$ production.

#### 4.4.1. *Coupling the $N_2$RR with OER-alternative reactions*

When it comes to the $N_2$RR, achieving high selectivity and activity for $NH_3$ production is highly challenging owing to the unfavorable kinetic and energetic barrier of the N≡N triple bond. Thus, the cathodic reaction and its corresponding catalysts remain the focus points in reported $N_2$RR hybrid systems, where the OER alternatives have included the commonly used AOR [84,156,157], the HMFOR [158], and the oxidation of sodium gluconate [159] (Table 5). Initially, Bai et al. [156] pioneered a GOR-assisted nitrogen reduction system via employing bimetallic RhCu ultrathin nanoflake nanoaggregates (RhCu-BUNNs) as bifunctional catalysts, with $NH_3$ produced at the cathode and glyceraldehyde at the anode. The enhanced $N_2$RR performance of RhCu-BUNNs was assigned to the introduced Cu, which effectively weakened the competitive HER and reduced the energy required in the *NN reductive process. The assembled hybrid electrolyzer required a cell voltage of only 0.9 V to achieve a current density of 10 mA $cm^{-2}$, far lower than its glycerol-free counterpart (1.84 V). Afterwards, the MOR was also integrated with $N_2$RR electrolysis ($N_2$RR||MOR), facilitating cathodic $NH_3$ and anodic formate production [84,157]. For the proposed hybrid system, Chang et al. prepared Bi nanosheets with partial surface oxidation ($Bi/Bi_2O_2CO_3$ NS) for the $N_2$RR, achieving a superior $NH_3$ yield of 3.18 ± 0.26 μg $h^{-1}$ $cm^{-2}$ and a $FE_{NH_3}$ of 14.59% ± 1.41% at −0.2 $V_{RHE}$. Additionally, Ni–Co double hydroxide grown on ultrathin Bi NS (NiCo DH-Bi NS) was tailored for driving the MOR with formate production (Fig. 16a) [84]. Theoretical

**Table 4**
Coupling the 2e⁻ORR with OER-alternative oxidation reactions.

| Catalysts (cathode/anode) | Catholyte\|anolyte | Products (cathode (FE)/ anode (FE)) | Cell potential (V) | Current density (mA $cm^{-2}$) | Cell type | Tested long-term stability (h) | Ref. |
|---|---|---|---|---|---|---|---|
| $TiO_{2-x}$\|\|$TiO_{2-x}$ | $O_2$-saturated 1 M KOH\|\|2 M $KHCO_3$ | $H_2O_2$(NG)/ $H_2O_2$(NG) | 2 | 40 (mA) | H-type cell | 12 | [148] |
| $CeO_2$ NCs\|\|$CeO_2$ NCs | $O_2$-saturated 1 M KOH\|\|1 M KOH | $H_2O_2$(92%)/ $H_2O_2$(92%) | ~2.2 | 30 | Hydrophobic breathable membrane separated H-type cell | NG | [149] |
| O-CNT\|\|$Ni_{0.13}Ti_{0.87}O_{2-y}$ | $O_2$-saturated 0.5 M KOH\|\| 0.5 M $KHCO_3$ and 3.5 M $K_2CO_3$ | $H_2O_2$(79.4%)/ $H_2O_2$(20.1 %) | 2 | 80 (mA) | PEM-separated H-type cell | NG | [49] |
| O-GF\|\|Pt plate | 0.1 M NaOH\|\|3.5 wt% NaCl | $H_2O_2$(NG)/ NaClO(NG) | 3.2 | NG | PEM-separated H-type cell | 36 | [152] |
| B/N-onion carbon \|\|$Ni_1Mn_1$-MOF-Se/NF | 1 M NaOH\|\|1 M KOH + 0.5 M EG | $H_2O_2$ (NG)/formate (NG) | 0.7 | ~50 | PEM-separated flow cell | 10 | [145] |

NG: Not given.

**Table 5**
Coupling the NRR with OER-alternative oxidation reactions.

| Catalysts (cathode/ anode) | Catholyte\|anolyte | Products (cathode (FE)/anode (FE)) | Cell potential (V) | Current density (mA $cm^{-2}$) | Cell type | Tested long-term stability (h) | Ref. |
|---|---|---|---|---|---|---|---|
| RhCu-BUNNs\|\|RhCu-BUNNs | $N_2$-saturated 0.1 M KOH\|\| Ar-saturated 0.1 M KOH with glycerol | $NH_3$ (NG)/ glyceraldehyde (NG) | 0.9 | 10 | H-type cell | 12 | [156] |
| CoPPi\|\|CoPPi | $N_2$-saturated 0.1 M KOH\|\| 1 M KOH with 1 M methanol | $NH_3$(NG)/formic acid (NG) | 2.0 | 10 | H-type cell | 2 | [157] |
| Bi/$Bi_2O_2CO_3$ NS\|\|NiCo DH–Bi NS | $N_2$-saturated 0.1 M $Na_2SO_4$\|\|1.0 M KOH with 3.0 M methanol | $NH_3$(near 100%)/formic acid (NG) | 2.2 | 2.5 | H-type cell | 30 | [84] |
| Ru(III)-PEI@MWCNTs\|\| Ru(III)-PEI@MWCNTs | $N_2$-saturated 0.1 M KOH\|\| 0.1 M KOH with 1 mM HMF | $NH_3$(NG)/FDCA (94 %) | 1.34 | 0.5 | H-type cell | 27 | [158] |
| JUC-1000/CC\|\|JUC-1000/CC | $N_2$-saturated 1.0 M $Na_2SO_4$\|\|1.0 M $Na_2SO_4$ with 1.0 M sodium gluconate | $NH_3$(11.9%)/glucaric acid (NG) | 0.4 | NG | H-type cell | 12 | [159] |
| R-NiCu-OH\|\|R–NiCuO | 0.1 M $KNO_3$ + 1 M KOH\|\| 1 M KOH + 0.1 M glycerol | $NH_3$ (71.9%)/formic acid (NG) | 1.8 | 300 | Flow cell | NG | [62] |
| $Cu_2O$\|\|$Cu_2O$ | 1 M KOH + 100 ppm $NO_3^-$ \|\|1 M KOH + 1 M HCHO | $NH_3$ (99.77%)/HCOOH (NG) | −0.19 | 10 | H-type cell | 20 | [47] |
| $Co_3O_4$@NiO HNTs\|\| $Co_3O_4$@NiO HNTs | 0.5 M $Na_2SO_4$ with 200 ppm $NO_3^-$\|\|1 M KOH with 0.5 mmol of THIQs | $NH_3$(54.97%)/DHIQ (NG) | NG | NG | H-type cell | NG | [166] |
| LC-CoOOH/CF\|\|Pd NTs/NF | 1 M KOH with 200 ppm $KNO_3$\|\|PET hydrolysate | $NH_3$(94.47%)/GA (~80%) | 1.2 | ~20 | H-type cell | 7 | [165] |
| CoRu-MOF/NF\|\|CoRu-MOF/NF | 1 M KOH with 200 ppm $KNO_3$\|\|PET hydrolysate | $NH_3$(96.43%)/formate (97.93%) | 2.3 | NG | H-type cell | NG | [161] |
| DMAB–Co-MOF/NF\|\| DMAB–Co-MOF/NF | 1 M KOH with 200 ppm $KNO_3$\|\|1 M KOH 4 M $Na_2S$ | $NH_3$(~85%)/S(NG) | 1.062 | 50 | H-type cell | NG | [164] |
| Cu–NiO UTNSs\|\|Cu–NiO UTNSs | 0.5 M $Na_2SO_4$ + 200 ppm $NaNO_3$\|\|0.5 M $Na_2SO_4$ + 0.5 M $Na_2S$ | $NH_3$(90.6%)/$S_x^{2-}$ (NG) | 0.2 | > 10 | H-type cell | 20 | [167] |

NG: Not given.

calculations and electrochemical *in situ* tests confirmed that the Bi atom adjacent to the oxygen vacancy serves as the potential active site, with $N_2$ being reduced via the distal protonation pathway over the Bi/$Bi_2O_2CO_3$ NS (Fig. 16b). When assembled with the two electrodes, the cell voltage of the $N_2$RR||MOR electrolyzer was 251 mV less than that of a $N_2$RR|| OER electrolyzer at 10 mA $cm^{-2}$, achieving an $NH_3$ yield of 2.787 μg $h^{-1}$ $cm^{-2}$ at 2.2 V while maintaining good cycling stability (Fig. 16c). Another recent work designed a bifunctional catalyst for $N_2$RR||MOR coupled electrolysis [157]. Cobalt pyrophosphate micro-flowers ($CoP_2O_7$) achieved a peak $FE_{NH_3}$ of 43.37% and an $NH_3$ yield of 159.6 μg $h^{-1}$ $mg_{cat}^{-1}$ at −0.2 $V_{RHE}$ for the $N_2$RR and simultaneously showed activity for the MOR, with a $FE_{formate}$ of 59.2% and a formate yield of 2.78 μg $h^{-1}$ $mg_{cat}^{-1}$ at 1.29 $V_{RHE}$. The $N_2$RR activity of $CoP_2O_7$ was attributed to the cationic charge distribution over metal species, which was conducive to $N_2$ adsorption and the anionic $P_2O_7^{4-}$ groups that promoted hydrogenating adsorbed N species for $NH_3$ generation. The $N_2$RR||MOR coupled system driven by the bifunctional catalyst obtained a yield rate of 95.2 μg $h^{-1}$ $mg_{cat}^{-1}$ for $NH_3$ and 2.53 μmol $h^{-1}$ $mg_{cat}^{-1}$ for formic acid, surpassing the results of an OER-involved system, where only 48.53 μg $h^{-1}$ $mg^{-1}$ of $NH_3$ was obtained.

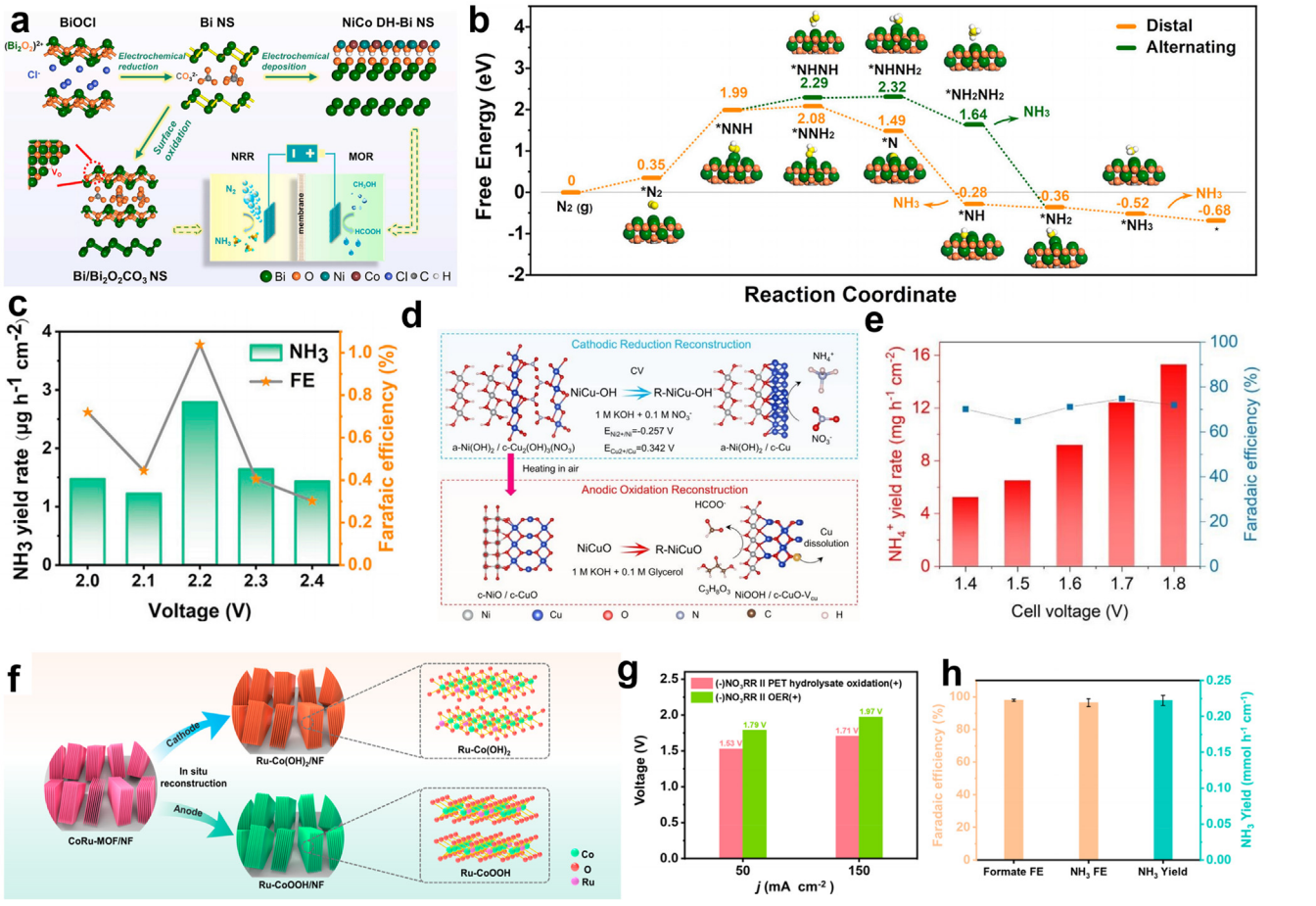


**Fig. 16.** (a) Schematic illustration of an electrode catalyst synthesis and nitrogen–methanol co-electrolysis system. (b) Free-energy diagrams for $N_2$ reduction through distal and alternating mechanisms, as well as the corresponding structures of the reaction intermediates. (c) $NH_3$ yields and FEs of the $N_2$RR||MOR electrolyzer at different applied potentials. Reproduced with permission from Ref. [84], Copyright 2022, Cell Press. (d) Schematic illustration showing the reconstruction of the NiCu–OH nanocomposite to form the cathodic and anodic catalysts. (e) Dependence of $NH_4^+$ yield and FE on cell voltage in a custom-designed flow refinery. Reproduced with permission from Ref. [62], Copyright 2022, Royal Society of Chemistry. (f) Synthetic scheme of Ru–$Co(OH)_2$/NF and Ru–CoOOH/NF. (g) Voltage at different current densities for the $NO_3$RR||PET upcycling and $NO_3$RR||OER systems. (h) $FE_{Formate}$, $FE_{NH_3}$, and yield rates over the CoRu-MOF/NF pre-catalyst at 2.3 V. Reproduced with permission from Ref. [161], Copyright 2023, American Chemical Society.

Elsewhere, the feasibility of integrating HMF oxidation with the $N_2$RR ($N_2$RR||HMFOR) was demonstrated using a bifunctional Ru(III) polyethyleneimine (Ru(III)-PEI) catalyst supported on carboxyl-modified carbon nanotubes (Ru(III)-PEI@MWCNTs) [158]. The Ru(III)-PEI@MWCNTs enabled the electrochemical conversion of $N_2$ into $NH_3$, with a yield rate of 188.90 μg $mg_{cat}^{-1}$ $h^{-1}$ and a $FE_{NH_3}$ of 30.93%; it also displayed activity for the HMFOR (0.5 mA $cm^{-2}$ at 1.34 V), with mainly FDCA produced. The Ru(III)–N coordination bond in the prepared catalysts was responsible for the $N_2$RR activity. The constructed $N_2$RR||HMFOR delivered 0.5 mA $cm^{-2}$ at a cell voltage of 1.34 V, with an anodic $FE_{FDCA}$ of 94%. The rather low current density obtained in this study suggests the complexity of the $N_2$RR-involved hybrid system, demanding further investigation to improve its performance. In another study, a novel conceptual hybrid system coupling $N_2$RR with the electrochemical oxidation of sodium gluconate (ECSG) ($N_2$RR||ECSG) was demonstrated using a bifunctional self-supported electrode ($Cu^{II}$-MOF on carbon cloth (JUC-1000/CC)), yielding $NH_3$ alongside the highly valuable glucaric acid [159]. The assembled $N_2$RR||ECSG exhibited an $NH_3$ yield rate of 24.7 mg $mg_{cat}^{-1}$ $h^{-1}$ and a $FE_{glucaric\ acid}$ of 96.96% at 0.4 V. Based on the systems summarized above, it can be concluded that these $N_2$RR hybrid systems were only able to yield $NH_3$ and anodic products at a very low current density, far below 10 mA $cm^{-2}$. Further, it has proven difficult to meet the optimal current density for $N_2$RR-involved systems, and the reaction rate of anodic reactions was greatly limited by the low conversion efficiency of the $N_2$RR, resulting from its very sluggish kinetics, the low solubility of $N_2$, and the competitive HER.

#### 4.4.2. *Coupling the $NO_3^-$RR with OER-alternative reactions*

Compared with the $N_2$RR, $NH_3$ electrosynthesis via the nitrate reduction reaction ($NO_3^-$RR, $E^0$ = 0.69 $V_{RHE}$) is a considerably easier pathway due to the far lower dissociation energy of the N=O bond (204 kJ $mol^{-1}$) in nitrate than that of the N≡N bond (941 kJ $mol^{-1}$) in nitrogen, as well as the high solubility of nitrate [160,161]. Moreover, nitrate is a plentiful nitrogen source and widely present in industrial and agricultural wastewater. Being able to extract it and utilize it again as a resource is crucial for wastewater denitrification and restoring the imbalanced nitrogen cycle. Hence, upgrading nitrate into $NH_3$ via the electrochemical $NO_3^-$RR has emerged as a prominent area of research, gaining significant traction and making rapid advances in the last three years [11,160]. Extensively engineered Cu- and Co-based nanoelectrocatalysts have been meticulously crafted to facilitate the conversion of nitrate into $NH_3$ through a variety of synthetic methodologies. These endeavors aim to augment both the number of active sites and the intrinsic activity of each site, thereby enhancing overall catalytic efficiency. The corresponding catalytic mechanisms during the $NO_3^-$RR process have also been investigated in depth using a combination of *in situ* and *ex situ* characterization techniques, theoretical calculations, and isotope experiments, which have resulted in useful guidance for designing electrocatalysts to promote $NH_3$ electrosynthesis [162]. Remarkably, near-unity nitrate conversion efficiency and a $FE_{NH_3}$ of over 90% at an industrial current density of 1 A $cm^{-2}$ were achieved using well-designed electrocatalysts for the $NO_3^-$RR [163].

Given that the $NO_3^-$RR has been investigated extensively, we now need to promote its practical application through further enhancing the economic benefits and lowering the required energy of nitrate electrolysis by replacing the anodic OER with these value-added oxidative reactions. In this context, a series of hybrid electrolysis systems were proposed by coupling the $NO_3^-$RR with widely used oxidation reactions that include the GOR [62], FMOR [47], SOR [164], PET upcycling [161, 165], and the semi-dehydrogenation of tetrahydroisoquinolines [166], resulting in dual-value-added production and high overall electrochemical efficiency. Some of the most recently proposed systems have demonstrated outstanding performance, underscoring their potential for practical application. In the proposed GOR-coupled electrolysis system, a NiCu bimetallic hydroxide (NiCu–OH) composed of crystalline $Cu_2(OH)_3(NO_3)$ and amorphous $Ni(OH)_2$ (a-$Ni(OH)_2$/$Cu_2(OH)_3(NO_3)$) was prepared as the pre-catalyst for both the cathode and the anode. During the $NO_3^-$RR process, the NiCu–OH evolved into a complex of crystalline metallic Cu and a-$Ni(OH)_2$ (a-$Ni(OH)_2$/c-Cu), undergoing *in situ* electrochemical reconstruction and thereby presenting high selectivity and activity for converting nitrate into $NH_4^+$. Meanwhile, the NiCu–OH reconstructed into active NiOOH for catalyzing the GOR into producing formate via annealing in the air, forming metal oxide (NiCuO) followed by *in situ* electrooxidation (Fig. 16d) [62]. A series of *in situ* and *ex situ* experiments confirmed the superior $NO_3^-$RR performance of a-$Ni(OH)_2$/c-Cu, which was attributed to the cooperative effect between a-$Ni(OH)_2$ and c-Cu. Here, the a-$Ni(OH)_2$ was active in forming stable adsorbed elemental hydrogen ($H_{ad}$), which subsequently facilitated the formation of N–H species with crucial adsorbed nitrogen intermediates on the c-Cu surface. A flow electrolyzer assembled with the catalysts demonstrated a 285 mV in reduction in cell voltage at 100 mA $cm^{-2}$ when glycerol was added to the electrolyte. Moreover, it achieved an industrial current density of 300 mA $cm^{-2}$ at ~1.8 V, with an anodic $NH_4^+$ yield rate of 15.3 mg $h^{-1}$ $cm^{-2}$ and a FE of 71.9% (Fig. 16e).

In a recent attempt by Xiao et al. [47], the FOR was for the first time integrated into the electrosynthesis of $NH_3$ via nitrate electrolysis ($NO_3^-$RR||FOR) driven by a bifunctional $Cu_2O$ catalyst. The $Cu_2O$ presented excellent $NO_3^-$RR performance owing to the $Cu_2O$/Cu heterojunctions formed *in situ*. The anodic oxidation involved a tandem reaction pathway wherein cubic $Cu_2O$ underwent electrochemical oxidation to form orthorhombic $Cu(OH)_2$, followed by HCHO chemically reducing $Cu(OH)_2$ into $Cu_2O$ to produce formate and $H_2$, and the $Cu_2O$ newly formed *in situ* acted as active sites for the FOR. This coupled system demonstrated a remarkably low cell voltage of −0.19 V to deliver 10 mA $cm^{-2}$ with the efficient production of formate and $NH_3$ (unity nitrate conversion efficiency and a $FE_{NH_3}$ of over 99%).

Ren et al. also conducted an array of investigations into hybrid electrolysis systems for the $NO_3^-$RR, coupled with PET upcycling ($NO_3^-$RR||PET upcycling) and sulfion recycling ($NO_3^-$RR||SOR) [161, 164,165]. In their studies, a range of Co-based nanomaterials were meticulously engineered to enhance the efficiency of the $NO_3^-$RR or serve as bifunctional catalysts. For the $NO_3^-$RR||PET upcycling electrolysis system in one of their works, Ru-incorporated Co-based MOF nanosheets grown on Ni foam (CoRu-MOF/NF) served as the bifunctional pre-catalyst for a hybrid system, which underwent electrochemical *in situ* reconstruction into Ru–$Co(OH)_2$/NF for the $NO_3^-$RR in the cathode and Ru–CoOOH/NF for EG oxidation in the anode [161]. The reconstructed Ru–$Co(OH)_2$/NF achieved impressive $NO_3^-$RR performance, with an $NH_3$ yield rate of 0.244 mmol $h^{-1}$ $cm^{-2}$ and a $FE_{NH_3}$ of 94.3%. The integrated Ru efficiently promoted the hydrogenation step for $NH_3$ production by optimizing the adsorption–desorption properties of the Ru–$Co(OH)_2$/NF electrode and enhancing the activation of H species for N–H species formation. Meanwhile, the reconstructed Ru–CoOOH/NF effectively catalyzed EG conversion into formate with a FE of 96.53% at 1.33 $V_{RHE}$. The incorporated Ru facilitated EG oxidation by forming more hydroxylated species (Ru–OH), thus serving as the electron–proton conductor (Fig. 16f). Enabled by the two reconstructed electrodes, the assembled electrolysis system delivered current densities of 50 and 150 mA $cm^{-2}$ at 1.53 V and 1.71 V, respectively, 260 mV less than a $NO_3^-$RR||OER system (Fig. 16g). Moreover, the system exhibited a high $NH_3$ yield rate of 0.222 mmol $h^{-1}$ $cm^{-2}$, along with notable selectivity, boasting a $FE_{formate}$ of 97.93% and a $FE_{NH_3}$ of 96.43% at 2.3 V (Fig. 16h). For the $NO_3^-$RR||SOR electrolysis system catalyzed by the highly active Co-based catalysts reconstructed *in situ*, co-production $NH_3$ and S was initiated at a mere 0.27 V, and a current density of 50 mA $cm^{-2}$ was achieved at 1.062 V, 1.597 V less than that of the $NO_3^-$RR||OER system [164]. The fabricated pre-catalysts, specifically dimethylamineborane (DMAB)-treated Co-MOF (DMAB–Co-MOF/NF), underwent *in situ* reconstruction into amorphous B–Co–S/NF for the SOR and heterogeneous CoOOH/$Co(OH)_2$/NF for the $NO_3^-$RR during the electrocatalytic process. This transformation resulted in the development of a thin nanosheet structure and a redox synergy between $Co^{2+}$ and $Co^{3+}$, thereby enhancing the performance of the $NO_3^-$RR, with $FE_{NH_3}$ of 94.16% at −0.2 $V_{RHE}$. Additionally, the *in situ* formation of abundant defects and unsaturated sites, and the incorporation of elemental B, contributed significantly to the SOR performance, realizing 100 mA $cm^{-2}$ at only 0.268 $V_{RHE}$. Based on the above findings (Table 4), the majority of electrocatalysts employed in these $NO_3^-$RR integrated hybrid systems were pre-catalysts, often undergoing *in situ* reconstruction during catalytic processes, which paves the way for novel methods of developing efficient catalysts for such hybrid systems. Furthermore, these studies have corroborated that the conversion of $NO_3^-$ into $NH_3$ is adaptable and versatile, and is capable of synergizing with various value-added oxidation reactions, thus enhancing the feasibility of practical applications. With the growing focus on $NO_3^-$RR-involved hybrid systems, and looking beyond the development of cost-effective and efficient catalysts, future research endeavors should prioritize ultra-long stability tests and product separation methodologies.

### 4.5. Other hybrid systems

In addition to the frequently observed reduction reactions of inorganic molecules and compounds during electrolysis, certain uncommon reductive reactions in mild aqueous environments have been proposed to integrate with OER alternatives, aiming to achieve dual-value-added production and optimize energy utilization and electron economy [68, 168]. Among these, the predominant emphasis lies on upgrading organics through electrochemically induced reductive hydrogenation, coupled with oxidation processes [68,169]. Centering on the upgrading of the HMF biomass molecule, an array of paired electrolysis systems that coupled organics upgrading in the cathode with the HMFOR in the anode have been developed for the green synthesis of two valuable organic compounds. Given that HMF can also be upgraded to 2,5-dihydroxymethylfuran (DHMF) via electrocatalytic hydrogenation, a paired electrolysis system integrating HMF reduction in the cathode and HMF oxidation in the anode has garnered significant interest. A series of related studies were dedicated to developing highly active and selective electrocatalysts for both reactions within the HMF-paired electrolysis system, leading to greatly enhanced electrosynthesis performance [170–174].

In a recent study using a HMF-paired electrolysis system, Guo et al. designed highly active catalysts comprising Ag nanoparticles supported on $SnO_2$ nanosheet arrays (Ag/$SnO_2$) for cathodic HMF reduction [173]. The elaborate Ag/$SnO_2$ electrocatalyst catalyzed HMF hydrogenation into DHMF with a FE of over 95% in a potential range of −0.62 to −1.12 $V_{RHE}$ with commendable cycling stability and a maximum productivity of over 1200 μmol $cm^{-2}$ $h^{-1}$, better than that of a Ag-free counterpart (Fig. 17a). The HMF reduction into DHMF over Ag/$SnO_2$ in the tested potential window was revealed to proceed through the more favorable hydrogen addition mechanism (the Langmuir–Hinshelwood (L-H) mechanism), whereby the $H^+/H_2O$ was first reduced into active H* species absorbed on the catalyst surface (Volmer reaction), and the H* species then hydrogenated with the adsorbed HMF, forming DHMF. As

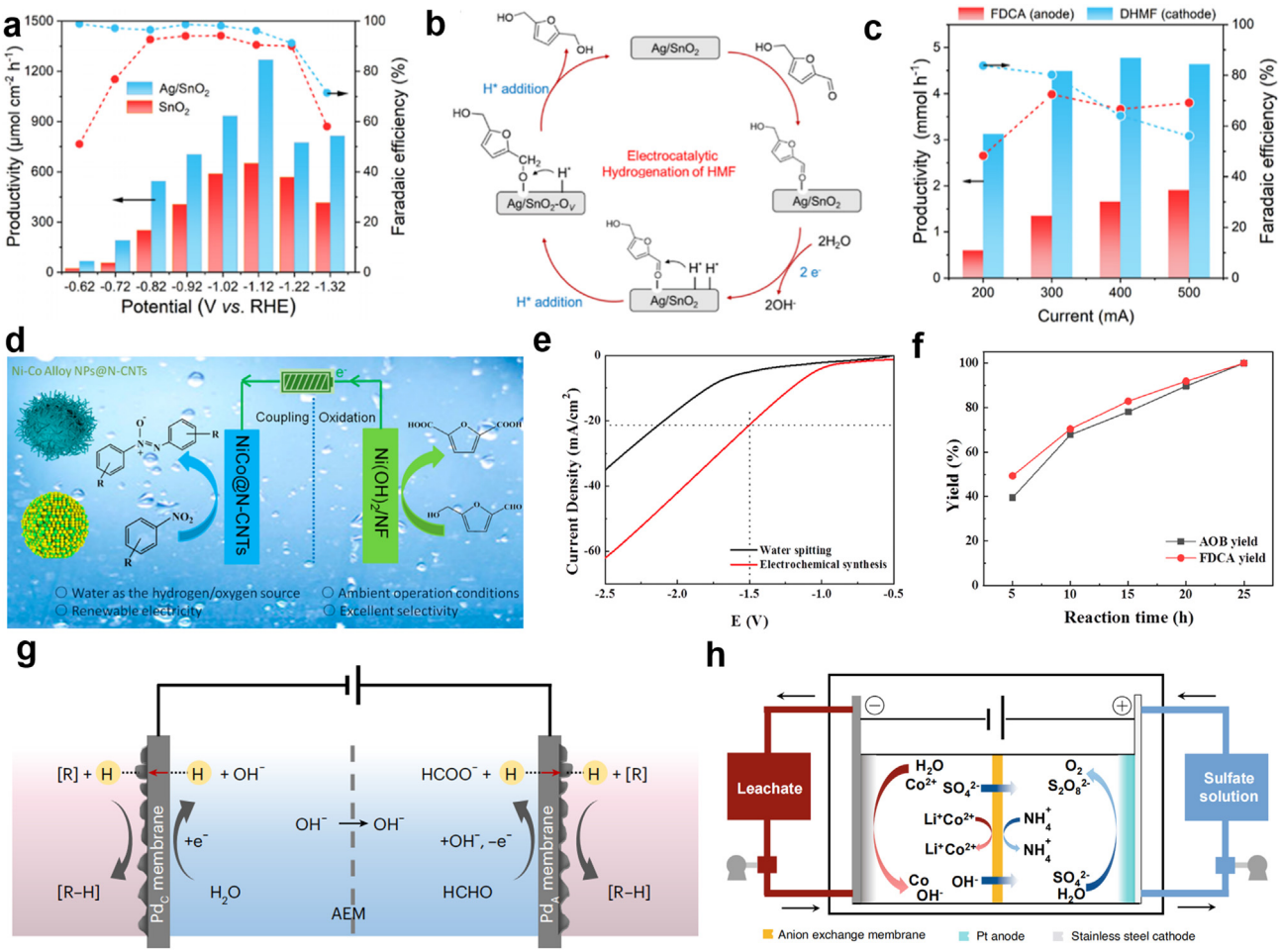


**Fig. 17.** (a) Productivity and $FE_{DHMF}$ over $Ag/SnO_2$ and $SnO_2$ under different potentials in 0.5 M $KHCO_3$ with 50 mM HMF for 1 h. (b) Proposed L-H mechanism of HMF hydrogenation over $Ag/SnO_2$. (c) Current-dependent productivity and $FE_{DHMF}$ and $FE_{FDCA}$ in the HMF-ER||HMF-EO system. Reproduced with permission from Ref. [173], Copyright 2023, American Chemical Society. (d) Schematic illustration of the two-electrode electrolyzer comprising a NiCo@N-CNTs cathode and a $Ni(OH)_2$/NF anode. (e) LSV curves of the NiCo@N-CNTs||$Ni(OH)_2$/NF electrolyzer. (f) The AOB and FDCA yields in the integrated cell. Reproduced with permission from Ref. [179], Copyright 2023, American Chemical Society. (g) The proposed electrocatalytic dual hydrogenation strategy involves the use of a four-compartment assembly. Reproduced from Ref. [68] with permission from Springer Nature, Copyright 2023. (h) Schematic diagram showing the mechanisms of the reaction for the paired system integrating recycling Co with persulfate production. Reproduced with permission from Ref. [168], Copyright 2021, Elsevier.

the co-catalyst, the Ag nanoparticles not only enhanced the Volmer reaction for H* generation but also facilitated the formation of oxygen vacancies on $SnO_2$ under reaction conditions (Fig. 17b). These vacancies functioned as electrophilic sites facilitating the selective adsorption and hydrogenation of the carbonyl bond (C=O) in HMF to form DHMF. Then the overall HMF flow electrolysis system, with both reaction surface areas measuring 9 $cm^2$, was set up by employing $Ag/SnO_2$ as the cathode for HMF electrochemical reduction and a CoFeP nanosheet array grown on Ni foam (CoFeP/NF) catalyst as the anode for HMF electrochemical oxidation (HMF-ER||HMF-OR). The system attained 4.48 mmol DHMF with a FE of 80.2% and 1.35 mmol FDCA with a FE of 72.4% after 1 h of constant electrolysis at 300 mA (Fig. 17c). Moreover, the calculated electric energy consumption within 1 h of constant electrolysis at 200 mA showed a 43% decrease in energy usage over the HMF-ER||HMF-OR system compared to the HMF-ER||OER system. The technoeconomic analysis revealed that the overall HMF electrolysis system attained a far higher profit of around $3150/ton of DHMF than the HMF-ER||OER system ($425/ton of DHMF), suggesting good economy.

In addition, other organics reduction reactions, such as the hydrogenation of p-nitrophenol to p-aminophenol [175–177] or of nitrobenzene to aniline [178], and the reduction of nitrobenzene to azoxy-benzene [179], have been used to pair with HMF oxidation in aqueous electrolysis system, and non-noble electrocatalysts were designed to drive these hybrid systems, achieving nearly 100% conversion efficiency and over 90% product FEs in both sides. For instance, Gong et al. [179] combined the nitrobenzene (NB) reduction reaction and the HMF oxidation reaction in a two-electrode electrolyzer, achieving the co-production of valuable azoxy-benzene (AOB) and FDCA, and successfully enhancing the energy utilization efficiency of the system (Fig. 17d). A facile reductive pyrolysis approach was used to fabricate an electrocatalyst consisting of NiCo alloy NPs confined on the tip of N-doped carbon nanotubes (NiCo@N-CNTs) from a bimetal–MOF precursor, which exhibited superior electrocatalytic activity with nearly 100% conversion efficiency and > 97% FE toward azoxy-benzene formation. The CNT-confined structure ensured the stability of the active NiCo alloy during the reductive process and thus resulted in superior nitrobenzene reduction performance. Moreover, the excellent catalytic performance of NiCo@N-CNTs was confirmed to be generalizable to other nitroarene derivatives. A two-electrode electrolyzer equipped with the NiCo@N-CNTs as the cathode and $Ni(OH)_2$ grown on nickel foam ($Ni(OH)_2$/NF) as the anode required a low cell voltage of only 1.5 V to reach 21 mA $cm^{-2}$ (Fig. 17e), as well as 100% yields for both AOB and FDCA (Fig. 17f).

Aside from HMFOR-involved systems, other novel hybrid electrolysis systems for producing important industrial organic chemicals keep coming out, including pairing the reduction of nitroarene reduction into

azoxybenzene with aliphatic amines oxidation into nitriles [180]; azo-aromatics production via pairing the reductive coupling of nitro-aromatics and the oxidative coupling of aromatic amines in one single-chamber cell [181]; coupling the dichlorination of 1,2-dichloroethane to ethylene with the aromatic chlorination reaction [182]; integrating lignin model compounds oxidation with the 2-furaldehyde reduction [183]; coupling formaldehyde oxidation with the hydrogenation of unsaturated dicarboxylic acids [68] and furfuryl hydrogenation into furfuryl alcohol [169]; and co-conversions of polybutylene succinate (PBS) waste plastics and biomass-derived maleic acid [184], to name a few. In a recent distinctive work, the dual hydrogenation of maleic acid to succinic acid in chambers outside of the electrochemical cell was achieved by pairing the low-potential oxidation of formaldehyde with maleic acid hydrogenation, using Pd membrane electrodes as electrocatalysts at both sides (Fig. 17g) [68]. The Pd membrane electrode had a unique and efficient hydrogen adsorption ability that allowed the active H* produced on the surface to permeate through the membrane electrode to the opposite side for hydrogenation reactions. In the anodic chamber, the formaldehyde was oxidized into formate and active H* species for maleic acid hydrogenation. The four-compartment electrolyzer design avoided separating products from complex electrolytes, and gram-scale production of succinic acid was achieved. Remarkably, the onset potential for the assembled electrolyzer was only 0.4 V, and a $FE_{succinic\ acid}$ of 184% was obtained at a current of 10 mA, far superior to the system without formaldehyde oxidation. Moreover, the proposed system can be extended to the hydrogenation of maleic acid analogues. This work provides a promising strategy for organic hydrogenation reactions.

Aside from these novel hybrid systems for dual organic electrosynthesis, Lv et al. [168] first reported the application of paired electrolysis in the waste recycling field by combining the electrochemical reduction of $Co^{2+}$ with the oxidation of sulfate (Fig. 17h). In their paired electrolysis system, simultaneously producing 1 kg Co metal and 2.08 kg $Na_2S_2O_8$ consumed only 9.39 kWh of electricity, while a single electrolysis system consumed about 30% more energy than the paired electrolysis system. Furthermore, the cathodic current efficiency of paired electrolysis was advanced by about 4% compared with the single electrolysis system, and high-purity cobalt metal (> 99.9%) was deposited at the cathode from the leachate of the spent lithium-ion batteries (LIBs). This work holds promising application prospects for recycling valuable metals in waste LIBs and degrading wastewater, with low energy consumption.

From the above analysis, it is evident that the landscape of other coupling hybrid systems is becoming increasingly diverse and intricate as the range of paired reactions expands (Table 6). This proliferation not only offers greater opportunities for electrosynthesis but also presents heightened challenges for stabilizing and analyzing products during the preliminary experimental phase. Furthermore, while novel hybrid systems continue to emerge, research endeavors in this realm ought not solely to prioritize the discovery and electrochemical evaluation of new hybrids. Rather, there is a pressing need for objective assessments of their practical applicability to furnish valuable guidance for subsequent studies and curtail superfluous research investment.

## 5. Summary and outlook

Optimizing the economic value and conversion efficiency in aqueous electrochemical synthesis systems is pivotal for advancing the practical application of electrolytic synthesis. OER alternatives with greater economic benefits and lower thermodynamic oxidation potentials have been extensively employed in electrolysis systems, with the goal of achieving energy-saving and dual-value electrolytic synthesis in aqueous solutions. This review has primarily summarized the key factors of electrolytic devices, the advanced methods developed for investigating catalytic mechanisms, and the latest progress in research on OER alternatives

**Table 6**
Coupling other reduction reaction with OER-alternative oxidation reactions.

| Catalysts (cathode/anode) | Catholyte\|anolyte | Products (cathode (FE)/anode (FE)) | Cell potential (V) | Current density (mA $cm^{-2}$) | Cell type | Tested long-term stability (h) | Ref. |
|---|---|---|---|---|---|---|---|
| Ag/C\|\|carbon felt | 20 mM HMF\|\|1 mM 4-acetamido-TEMPO +10 mM HMF | 2,5-bis(hydroxymethyl)furan (91%)/FDCA (96%) | −1.3 | NG | H-type cell | NG | [170] |
| OD-Ag\|\|Carbon cloth | 0.5 M borate buffer (pH = 9.2) + 20 mM HMF\|\|0.5 M borate buffer (pH = 9.2) + 10 mM HMF + 7.5 mM TEMPO | 2,5-bis(hydroxymethyl)furan (80.9%)/FDCA (83.4%) | ~2.0 | 10 mA | Flow cell | NG | [172] |
| Ag/$SnO_2$\|\|CoFeP | 0.5 M $KHCO_3$ + 50 mM HMF\|\|1 M KOH + 50 mM HMF | 2,5-Dihydroxymethylfuran (80.2% @300 mA)/FDCA (72.4 % @300 mA) | 2.39 | 500 | Flow cell | NG | [173] |
| $Co_3O_4$/Ni\|\|$Co_3O_4$/Ni | 0.1 M phosphate (pH = 7.0) + 10 mM HMF\|\|0.1 M KOH + 10 mM HMF | 2,5-Dihydroxymethylfuran (NG)/2,5-furandicarboxylic acid (NG) | −0.489 | NG | H-type cell | NG | [174] |
| Pd/VN\|\|VN | 0.2 M $HClO_4$ + 10 mM HMF\|\|1 M KOH + 10 mM HMF | DHMTHF (NG)/FDCA (NG) | 2.837 | 100 mA | MEA-involved flow cell | NG | [171] |
| $Cu_{60}Ni_{40}$\|\|CuNi NTs | 1 M KOH + nitrobenzene\|\|1 M KOH + HMF | Aniline (NG)/FDCA (NG) | 1.40 | 20 | H-type cell | NG | [178] |
| NiCo@N-CNTs\|\|Ni(OH)$_2$/NF | 1 M KOH + 25 mM nitrobenzene\|\|1 M KOH +25 mM HMF | Azoxy-benzene (NG)/FDCA (NG) | 1.5 | 21 | H-type cell | 25 h | [179] |
| $NiB_x$\|\|$NiB_x$/$NiO_x$ | 1 M KOH + p-nitrophenol\|\|1 M KOH + HMF | p-aminophenol (NG)/FDCA (NG) | 1.5 | 50 | H-type cell | NG | [175] |
| $Ni_3$Fe-MOF-OH\|\|$Ni_3$Fe-MOF-OH | 1 M KOH + 20 mM TEMPO + 0.2 M nitrobenzene + 0.25 M aniline | Azoxybenzene (71%)/dimesityldiazene (65%) | 1.4 | NG | Single-chamber cell | NG | [181] |
| $Cu_7Ag_3$/CF\|\|$Cu_3Ag_7$/CF | 1 M KOH + 0.05 M furfural\|\|1 M KOH + 0.6 M HCHO | Furfuryl alcohol (96.0%)/formate (100%) | 0.5 | 500 | Flow cell | 50 | [169] |
| NiFe-400\|\|NiCo-mono | 1 M KOH +10 mM p-nitrophenol\|\|1 M KOH + 10 mM HMF | p-aminophenol (> 98%)/FDCA (> 92%) | −1.5 | NG | H-type cell | 10 | [177] |
| $Pd_{NP}$/Pd\|\|$Pd_{NP}$/Pd | 50 mM maleic acid/Ar-saturated 1 M KOH/Ar-saturated 1 M KOH + 0.6 M HCHO\|\|50 mM maleic acid | Succinic acid (95%)/succinic acid (89%) | NG | 10 mA | Four-chamber cell | NG | [68] |
| $Cr^{3+}$-Ni(OH)$_2$/NF\|\|PdCu/NF | 1 M KOH + 0.05 M 1,4-Butanediol + maleic acid | Succinic acid/succinic acid (total 181.5%) | ~2.2 | 111 | Single-chamber cell | 110 | [184] |

coupled with electrolytic synthesis for dual-value-added products beyond water electrolysis. Currently, research on such integrated systems is still in its early stages, with many newly proposed electrolytic systems primarily focusing on catalyst studies and conducting basic conceptual verifications of proposed hybrid electrolysis systems. In these studies, the electrolytic synthesis systems, through the coupling of OER-alternative reactions, have achieved the overall preliminary goals of electrolytic voltage reduction, and cathodic and anodic reaction value enhancement. Yet despite the significant output in this research field, practical dual-value production goals remain distant. With a focus on practical applications, challenges exist for the rational matching of reaction pairs, the construction of electrocatalysts, electrolyzer design (including electrolyte selection, membrane selection, electrolyzer structural design, etc.), and comprehensive performance evaluation of electrolyzers (Fig. 18).

(1) In terms of matching reaction pairs, the alignment of reaction pairs must adhere to the principles of economic feasibility, as irrational pairings could escalate costs related to electrolyzer maintenance, product purification, and collection. Though various types of OER-alternative reactions are being employed in matching electrolysis, the impact of reactants and products on electrode catalytic performance, crossover of products in both sides, current density matching for both reactions, and the economic feasibility of product separation are often overlooked. Further, the performance of OER alternative reactions is predominantly tested using commercially purified small molecules. But this practice may not align well with economic objectives and could diverge from real-world applications in which raw materials are used. Consequently, it is imperative to conduct tests with these raw small-molecule reactants to evaluate their potential for practical application in the future. Investigating other economically viable novel oxidation replacement reactions is also a future direction for exploration. In all, finding rationally matched reaction pairs entails not only meeting the criteria for enhancing product value and reducing electrolysis potential but also taking into consideration the economic viability from a practical application standpoint.

(2) Regarding catalyst construction, the synthesis of highly active, stable, and selective catalysts is essential for achieving efficient dual-value product generation, due to issues related to product selectivity in both cathodic and anodic reactions. While researchers have made significant progress in catalyst development, challenges persist:

(a) Much catalyst development research remains confined to simplistic modification studies that achieve limited substantial improvements in catalytic performance.
(b) The majority of the reported catalysts for OER alternatives still derive from OER-related catalysts, making it challenging to avoid OER competition reactions during high-current electrolysis. Precise control over the composition and structure of target catalysts is crucial to effectively suppress OER reactions under high-current conditions.
(c) Although the theoretical potentials of organic oxidation reactions (OORs) are considerably lower than those of the OER, the overpotentials associated with the OORs of reported non-noble catalysts (exceeding 1.0 V) greatly surpass that of the OER reaction (~0.2–0.4 V) in alkaline media. Therefore, the quest for cost-effective catalysts capable of significantly reducing the overpotentials of these OORs is an especially challenging but crucial endeavor.
(d) We lack comprehensive studies on the catalytic mechanisms for more complex anodic replacement reactions, making it difficult to provide targeted guidance for the development of related catalysts. Apart from theoretical calculation methods, the combination of *in situ* techniques like vibration spectra, imaging, and X-ray-based characterizations is needed to reveal the dynamic changes in catalysts and catalytic mechanisms of these anodic reactions.
(e) Most studies on OER alternatives are focused on the electrochemical performance of catalysts in alkaline or acidic media. Efficient catalysts in milder neutral electrolyte media deserve attention.
(f) The preparation cost, large-scale production feasibility, and economic practicality of catalysts are often overlooked. Researchers

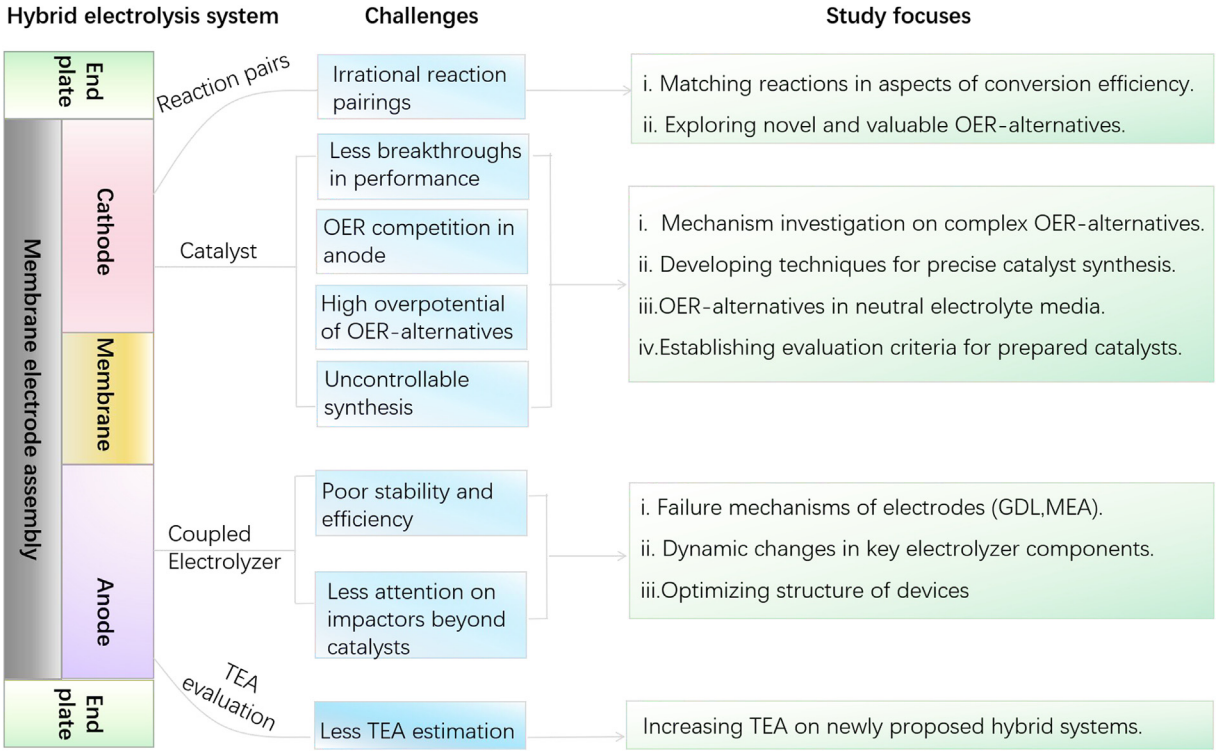


**Fig. 18.** Summary of the challenges and foci for future studies of hybrid electrolysis systems.

need to leverage existing knowledge and employ advanced synthesis and characterization techniques to evaluate the feasibility of large-scale production, help simplify synthesis processes, and exercise precise control over active sites, thereby achieving efficient catalysis and significantly reducing the costs associated with trial-and-error experimentation. Additionally, it is essential to establish evaluation criteria for the performance and economic viability of catalysts, especially for OER alternatives, to guide the direction of catalyst design.

(3) As for electrolyzer systems, the flow-type dual-cell electrolyzer has received increasing attention owing to its practicability. However, the durability of the crucial GDL electrodes commonly used in hybrid electrolysis systems involving gas reactants (e.g., $CO_2$, $N_2$, and $O_2$) is less than satisfactory, as the built gas–liquid–solid reaction interfaces easily suffer from flooding owing to changes in the GDL electrodes' hydrophilicity and hydrophobicity after undergoing a few hours of electrolysis. Consequently, the stability and electrolysis efficiency are far from sufficient to meet practical application requirements. To meet practical application needs, it is crucial to optimize the structure of cathode gas diffusion electrodes, elucidate the failure mechanisms of electrolysis structures, and construct a stable gas diffusion electrode reaction interface. Furthermore, when it comes to the comprehensive performance evaluation of electrolyzers, few studies focus on optimizing the overall operational conditions of the entire electrolysis system to enhance conversion rates and process stability. The impact of changes in key electrolyzer components (electrolyte, isolation membrane, electrolyzer structural design) on electrolysis is an important yet often overlooked aspect in coupled electrolysis systems. For the electrolyte, it is crucial to clarify the influence of ion species and the dynamic variation in ion concentration during long-term stability tests to provide guidance for electrolyte selection. However, in most studies, the given concentration and species of electrolytes have been used directly for these hybrid systems without additional optimization. Repeatedly refreshing electrolytes is a commonly used method to eliminate interference from the electrolytes during long-term tests, but it leads to significant resource waste. Instead, if meticulous investigations of electrolyte changes and precise monitoring were conducted, the degradation caused by electrolytes could be eliminated online by periodically adding the consumed substances. With respect to membrane selection, the type used depends on the electrolyte, but the changes it undergoes during long-term electrolysis have rarely been reported. Thus, variation in the ion transfer function of the membrane during the practical electrolysis process should be monitored by assessing the concentration changes of ions in both chambers, as well as by observing any alterations in the membrane's structure and components. In terms of the structural design of the electrolyzer, the internal fine structure, such as the runner plate design for gas and liquid, the chamber configuration, and current collection techniques can also significantly impact the overall performance. However, these aspects have not yet been studied in these hybrid electrolysis systems and warrant attention in future studies. Additionally, there is a scarcity of reported analyses on key performance parameters assessing the practicality of coupled electrolysis systems, including conversion efficiency, long-term stability, degradation rates, and energy consumption comparisons between conventional electrolysis systems and coupled electrolysis systems. Rigorous qualitative and quantitative analysis is needed for assessing product selectivity, yield, and conversion efficiency in coupled electrolysis systems.

(4) Lastly, technoeconomic analysis (TEA) is a crucial reference indicator to determine the economic feasibility of achieving system performance parameters for the commercialization and industrialization of dual-value electrolysis production technologies. Thus, a TEA is particularly necessary for any new hybrid system proposed in the future.

In summary, despite the notable achievements in this field at the laboratory stage, the practical implementation of these proposed hybrid systems still faces significant hurdles and remains quite distant from a successful transition to large-scale manufacturing via electrosynthesis routes. Future commercialization efforts require collaboration among researchers, industry stakeholders, and regulatory authorities to overcome barriers and fully exploit the capabilities of electrochemical approaches to achieve sustainable and efficient dual-value-added production. It is hoped that this review will offer valuable guidance for researchers addressing these challenges.

## CRediT authorship contribution statement

**Genxiang Wang:** Writing – original draft, Project administration, Methodology, Investigation, Funding acquisition. **Ao Chen:** Writing – original draft. **Yao Chen:** Writing – original draft. **Fen Qiao:** Writing – review & editing. **Junfeng Wang:** Writing – review & editing. **Nianjun Yang:** Writing – review & editing, Supervision, Conceptualization. **Hao Zhang:** Writing – review & editing, Supervision, Conceptualization. **Zhenhai Wen:** Writing – review & editing, Supervision, Funding acquisition, Conceptualization.

## Declaration of competing interest

The authors declare that they have no known competing financial interests or personal relationships that could have appeared to influence the work reported in this paper.

## Acknowledgments

This work was financially supported by the National Natural Science Foundation of China (No. 22209183, 22225902, U22A20436, 52436005), the National key Research & Development Program of China (2022YFE0115900, 2021YFA1501500), the CAS-Commonwealth Scientific and Industrial Research Organization (CSIRO) Joint Research Projects (121835KYSB20200039), Advanced Talents of Jiangsu University, China (Grant No. 23JDG027), and Natural Science Foundation of Fujian Province (2021J05100).

## References

[1] P. De Luna, C. Hahn, D. Higgins, S.A. Jaffer, T.F. Jaramillo, E.H. Sargent, What would it take for renewably powered electrosynthesis to displace petrochemical processes? Science 364 (2019) eaav3506.
[2] Statistical Review of World Energy, 72nd edition, Energy Institute, 2023.
[3] Renewables 2023, International Energy Agency, 2023.
[4] World Energy Investment 2023, International Energy Agency, 2023.
[5] J. Yount, D.G. Piercey, Electrochemical synthesis of high-nitrogen materials and energetic materials, Chem. Rev. 122 (2022) 8809–8840.
[6] M. Yan, Y. Kawamata, P.S. Baran, Synthetic organic electrochemical methods since 2000: on the verge of a renaissance, Chem. Rev. 117 (2017) 13230–13319.
[7] T. Smolinka, H. Bergmann, J. Garche, M. Kusnezoff, The history of water electrolysis from its beginnings to the present, in: Electrochemical Power Sources: Fundamentals, Systems, and Applications. Hygrogen Production by Water Electrolysis. Chaper 4, Elsevier B. V, 2022, pp. 83–164.
[8] I. Moussallem, J. Jörissen, U. Kunz, S. Pinnow, T. Turek, Chlor-alkali electrolysis with oxygen depolarized cathodes: history, present status and future prospects, J. Appl. Electrochem. 38 (2008) 1177–1194.
[9] R. Li, K. Xiang, Z. Peng, Y. Zou, S. Wang, Recent advances on electrolysis for simultaneous generation of valuable chemicals at both anode and cathode, Adv. Energy Mater. 11 (2021) 2102292.
[10] A.D. Handoko, F. Wei, Jenndy, B.S. Yeo, Z.W. Seh, Understanding heterogeneous electrocatalytic carbon dioxide reduction through operando techniques, Nat. Catal. 1 (2018) 922–934.
[11] D. Liu, L. Qiao, S. Peng, H. Bai, C. Liu, W.F. Ip, K.H. Lo, H. Liu, K.W. Ng, S. Wang, X. Yang, H. Pan, Recent advances in electrocatalysts for efficient nitrate reduction to ammonia, Adv. Funct. Mater. 33 (2023) 2303480.

[12] G. Wang, J. Chen, Y. Ding, P. Cai, L. Yi, Y. Li, C. Tu, Y. Hou, Z. Wen, L. Dai, Electrocatalysis for $CO_2$ conversion: from fundamentals to value-added products, Chem. Soc. Rev. 50 (2021) 4993–5061.

[13] A.J. Shih, M.C.O. Monteiro, F. Dattila, D. Pavesi, M. Philips, A.H.M. da Silva, R.E. Vos, K. Ojha, S. Park, O. van der Heijden, G. Marcandalli, A. Goyal, M. Villalba, X. Chen, G.T.K.K. Gunasooriya, I. McCrum, R. Mom, N. López, M.T.M. Koper, Water electrolysis, Nat. Rev. Method. Prim. 2 (2022) 84.

[14] Y. Ren, C. Yu, X. Tan, H. Huang, Q. Wei, J. Qiu, Strategies to suppress hydrogen evolution for highly selective electrocatalytic nitrogen reduction: challenges and perspectives, Energy Environ. Sci. 14 (2021) 1176–1193.

[15] N. Sbei, T. Hardwick, N. Ahmed, Green chemistry: electrochemical organic transformations via paired electrolysis, ACS Sustain. Chem. Eng. 9 (2021) 6148–6169.

[16] B. You, Y. Sun, Innovative strategies for electrocatalytic water splitting, Acc. Chem. Res. 51 (2018) 1571–1580.

[17] B. You, X. Liu, N. Jiang, Y. Sun, A general strategy for decoupled hydrogen production from water splitting by integrating oxidative biomass valorization, J. Am. Chem. Soc. 138 (2016) 13639–13646.

[18] Y. Wang, S. Lu, M. Yang, Z. Zhang, J. Zhang, Recent advances in anode catalysts for waste valorization through hybrid water electrolysis: towards sustainability beyond hydrogen production, Mater. Today Sustain. 25 (2024) 100630.

[19] H. Sun, X. Xu, L. Fei, W. Zhou, Z. Shao, Electrochemical oxidation of small molecules for energy-saving hydrogen production, Adv. Energy Mater. 14 (2024) 2401242.

[20] Q. Qian, Y. Zhu, N. Ahmad, Y. Feng, H. Zhang, M. Cheng, H. Liu, C. Xiao, G. Zhang, Y. Xie, Recent advancements in electrochemical hydrogen production via hybrid water splitting, Adv. Mater. 36 (2023) 2306108.

[21] E.A. Moges, C.-Y. Chang, M.-C. Tsai, W.-N. Su, B.J. Hwang, Electrocatalysts for value-added electrolysis coupled with hydrogen evolution, EES Catal. 1 (2023) 413–433.

[22] C. Wu, J. Zhu, H. Wang, G. Wang, T. Chen, Y. Tan, Porous $Ni_{1-x}Cu_xO$ nanowire arrays as noble-metal-free high-performance catalysts for ammonia-borane electrooxidation, ACS Catal. 10 (2019) 721–735.

[23] X. Liu, W. Sun, J. Chen, Z. Wen, Controllable electrochemical liberation of hydrogen from sodium borohydride, Angew. Chem. Int. Ed. 63 (2024) e202317313.

[24] X. Tan, C. Yu, X. Song, C. Zhao, S. Cui, H. Xu, J. Chang, W. Guo, Z. Wang, Y. Xie, J. Qiu, Toward an understanding of the enhanced $CO_2$ electroreduction in NaCl electrolyte over CoPc molecule-implanted graphitic carbon nitride catalyst, Adv. Energy Mater. 11 (2021) 2100075.

[25] C. He, D. Pan, K. Chen, J. Chen, Q. Zhang, H. Zhang, Z. Zhang, Z. Wen, Energy-efficient co-production of benzoquinone and $H_2$ using waste phenol in a hybrid alkali/acid flow cell, Angew. Chem. Int. Ed. 63 (2024) e202407079.

[26] W. Pan, J. Yuan, P. Wang, J. Wang, Y. Zhao, G. Wang, H. Yu, Z. Wen, Efficient ultra-low voltage electrolysis of $CO_2$ coupling with hydrazine oxidation degradation, Appl. Catal. B Environ. Energy 351 (2024) 124011.

[27] Global Hydrogen Review 2023, International Energy Agency, 2023.

[28] S. Jiao, X. Fu, S. Wang, Y. Zhao, Perfecting electrocatalysts via imperfections: towards the large-scale deployment of water electrolysis technology, Energy Environ. Sci. 14 (2021) 1722–1770.

[29] B. You, G. Han, Y. Sun, Electrocatalytic and photocatalytic hydrogen evolution integrated with organic oxidation, Chem. Commun. 54 (2018) 5943–5955.

[30] G. Chen, X. Li, X. Feng, Upgrading organic compounds through the coupling of electrooxidation with hydrogen evolution, Angew. Chem. Int. Ed. 61 (2022) e202209014.

[31] T. Wang, X. Cao, L. Jiao, Progress in hydrogen production coupled with electrochemical oxidation of small molecules, Angew. Chem. Int. Ed. 61 (2022) e202213328.

[32] D. Yan, C. Mebrahtu, S. Wang, R. Palkovits, Innovative electrochemical strategies for hydrogen production: from electricity input to electricity output, Angew. Chem. Int. Ed. 62 (2023) e202214333.

[33] W. Zhou, S. Chen, X. Meng, J. Li, J. Gao, Energy-saving cathodic $H_2$ production enabled by non-oxygen evolution anodic reactions: a critical review on fundamental principles and applications, Int. J. Hydrogen Energy 48 (2023) 15748–15770.

[34] H. Yu, S. Zhu, Y. Hao, Y.-M. Chang, L. Li, J. Ma, H.-Y. Chen, M. Shao, S. Peng, Modulating local interfacial bonding environment of heterostructures for energy-saving hydrogen production at high current densities, Adv. Funct. Mater. 33 (2023) 2212811.

[35] Z. Li, X. He, Q. Qian, Y. Zhu, Y. Feng, W. Wan, G. Zhang, Active site implantation for $Ni(OH)_2$ nanowire network achieves superior hybrid seawater electrolysis at 1 A $cm^{-2}$ with record-low cell voltage, Adv. Funct. Mater. 33 (2023) 2304079.

[36] B. Zhu, B. Dong, F. Wang, Q. Yang, Y. He, C. Zhang, P. Jin, L. Feng, Unraveling a bifunctional mechanism for methanol-to-formate electro-oxidation on nickel-based hydroxides, Nat. Commun. 14 (2023) 1686.

[37] Y. Guo, X. Yang, X. Liu, X. Tong, N. Yang, Coupling methanol oxidation with hydrogen evolution on bifunctional Co-doped Rh electrocatalyst for efficient hydrogen generation, Adv. Funct. Mater. 33 (2022) 2209134.

[38] L. Fan, Y. Ji, G. Wang, J. Chen, K. Chen, X. Liu, Z. Wen, High entropy alloy electrocatalytic electrode toward alkaline glycerol valorization coupling with Acidic Hydrogen Production, J. Am. Chem. Soc. 144 (2022) 7224–7235.

[39] T. Kahlstorf, J.N. Hausmann, T. Sontheimer, P.W. Menezes, Challenges for hybrid water electrolysis to replace the oxygen evolution reaction on an industrial scale, Glob. Chall. 7 (2023) 2200242.

[40] H.Y. Wang, M.L. Sun, J.T. Ren, Z.Y. Yuan, Circumventing challenges: design of anodic electrocatalysts for hybrid water electrolysis systems, Adv. Energy Mater. 13 (2022) 2203568.

[41] Y. Li, X. Wei, L. Chen, J. Shi, Electrocatalytic hydrogen production trilogy, Angew. Chem. Int. Ed. 60 (2021) 19550–19571.

[42] Z.J. Chen, J. Dong, J. Wu, Q. Shao, N. Luo, M. Xu, Y. Sun, Y. Tang, J. Peng, H.M. Cheng, Acidic enol electrooxidation-coupled hydrogen production with ampere-level current density, Nat. Commun. 14 (2023) 4210.

[43] Y. Li, X. Wei, S. Han, L. Chen, J. Shi, $MnO_2$ electrocatalysts coordinating alcohol oxidation for ultra-durable hydrogen and chemical productions in acidic solutions, Angew. Chem. Int. Ed. 60 (2021) 21464–21472.

[44] L. Fan, Y. Ji, G. Wang, Z. Zhang, L. Yi, K. Chen, X. Liu, Z. Wen, Bifunctional Mn-doped $CoSe_2$ nanonetworks electrode for hybrid alkali/acid electrolytic $H_2$ generation and glycerol upgrading, J. Energy Chem. 72 (2022) 424–431.

[45] X. Teng, K. Shi, L. Chen, J. Shi, Coupling electrochemical sulfion oxidation with $CO_2$ reduction over highly dispersed p-Bi nanosheets and $CO_2$-assisted sulfur extraction, Angew. Chem. Int. Ed. 63 (2024) e202318585.

[46] K. Xie, A. Ozden, R.K. Miao, Y. Li, D. Sinton, E.H. Sargent, Eliminating the need for anodic gas separation in $CO_2$ electroreduction systems via liquid-to-liquid anodic upgrading, Nat. Commun. 13 (2022) 3070.

[47] L. Xiao, W. Dai, S. Mou, X. Wang, Q. Cheng, F. Dong, Coupling electrocatalytic cathodic nitrate reduction with anodic formaldehyde oxidation at ultra-low potential over $Cu_2O$, Energy Environ. Sci. 16 (2023) 2696–2704.

[48] X. Ding, J. Zhang, Y. Li, CO electroreduction: what can we learn from its parent reaction, $CO_2$ electroreduction? eScience 3 (2023) 100137.

[49] Z. Wang, X. Duan, M.G. Sendeku, W. Xu, S. Chen, B. Tian, W. Gao, F. Wang, Y. Kuang, X. Sun, Highly efficient paired $H_2O_2$ production through $2e^-$ water oxidation coupled with $2e^-$oxygen reduction, Chem Catal. 3 (2023) 100672.

[50] M.F. Lagadec, A. Grimaud, Water electrolysers with closed and open electrochemical systems, Nat. Mater. 19 (2020) 1140–1150.

[51] Z.W. Seh, J. Kibsgaard, C.F. Dickens, I. Chorkendorff, J.K. Norskov, T.F. Jaramillo, Combining theory and experiment in electrocatalysis: insights into materials design, Science 355 (2017) 146.

[52] J. Wu, X. Liu, Y. Hao, S. Wang, R. Wang, W. Du, S. Cha, X.Y. Ma, X. Yang, M. Gong, Ligand hybridization for electro-reforming waste glycerol into isolable oxalate and hydrogen, Angew. Chem. Int. Ed. 62 (2023) e202216083.

[53] F. Ye, S. Zhang, Q. Cheng, Y. Long, D. Liu, R. Paul, Y. Fang, Y. Su, L. Qu, L. Dai, C. Hu, The role of oxygen-vacancy in bifunctional indium oxyhydroxide catalysts for electrochemical coupling of biomass valorization with $CO_2$ conversion, Nat. Commun. 14 (2023) 2040.

[54] H. Sun, Z. Yan, F. Liu, W. Xu, F. Cheng, J. Chen, Self-supported transition-metal-based electrocatalysts for hydrogen and oxygen evolution, Adv. Mater. 32 (2020) 1806326.

[55] H.P. Yang, X.D. Wang, Q. Hu, X.Y. Chai, X.Z. Ren, Q.L. Zhang, J.H. Liu, C.X. He, Recent progress in self-supported catalysts for $CO_2$ electrochemical reduction, Small Methods 4 (2020) 1900826.

[56] D. Wakerley, S. Lamaison, J. Wicks, A. Clemens, J. Feaster, D. Corral, S.A. Jaffer, A. Sarkar, M. Fontecave, E.B. Duoss, S. Baker, E.H. Sargent, T.F. Jaramillo, C. Hahn, Gas diffusion electrodes, reactor designs and key metrics of low-temperature $CO_2$ electrolysers, Nat. Energy 7 (2022) 130–143.

[57] S. Overa, B.S. Crandall, B. Shrimant, D. Tian, B.H. Ko, H. Shin, C. Bae, F. Jiao, Enhancing acetate selectivity by coupling anodic oxidation to carbon monoxide electroreduction, Nat. Catal. 5 (2022) 738–745.

[58] Z. Zhou, X. Pan, L. Sun, Y. Xie, J. Zheng, L. Li, G. Zhao, Boosting hydrogen production via selective two-electron mild electrochemical oxidation of tetrahydroisoquinolines completely to dihydroisoquinolines, Angew. Chem., Int. Ed. 62 (2023) e202216347.

[59] C. Tang, R. Zhang, W. Lu, Z. Wang, D. Liu, S. Hao, G. Du, A.M. Asiri, X. Sun, Energy-saving electrolytic hydrogen generation: $Ni_2P$ nanoarray as a high-performance non-noble-metal electrocatalyst, Angew. Chem., Int. Ed. 129 (2017) 860–864.

[60] H. Zhu, S. Sun, J. Hao, Z. Zhuang, S. Zhang, T. Wang, Q. Kang, S. Lu, X. Wang, F. Lai, T. Liu, G. Gao, M. Du, D. Wang, A high-entropy atomic environment converts inactive to active sites for electrocatalysis, Energy Environ. Sci. 16 (2023) 619–628.

[61] Y. Ding, P. Cai, Z. Wen, Electrochemical neutralization energy: from concept to devices, Chem. Soc. Rev. 50 (2021) 1495–1511.

[62] S. Li, P. Ma, C. Gao, L. Liu, X. Wang, M. Shakouri, R. Chernikov, K. Wang, D. Liu, R. Ma, J. Wang, Reconstruction-induced NiCu-based catalysts towards paired electrochemical refining, Energy Environ. Sci. 15 (2022) 3004–3014.

[63] M. Li, T. Wang, W. Zhao, S. Wang, Y. Zou, A pair-electrosynthesis for formate at ultra-low voltage via coupling of $CO_2$ reduction and formaldehyde oxidation, Nano-Micro Lett. 14 (2022) 211.

[64] Y.R. Wang, H.M. Ding, S.N. Sun, J.W. Shi, Y.L. Yang, Q. Li, Y. Chen, S.L. Li, Y.Q. Lan, Light, heat and electricity integrated energy conversion system: photothermal-assisted co-electrolysis of $CO_2$ and methanol, Angew. Chem. Int. Ed. 61 (2022) e202212162.

[65] Z. Li, Y. Gao, X. Meng, B. Sun, K. Song, Z. Wang, Y. Liu, Z. Zheng, P. Wang, Y. Dai, H. Cheng, B. Huang, In-situ-derived self-selective electrocatalysts for solar formate production from simultaneous $CO_2$ reduction and methanol oxidation, Cell Rep. Phys. Sci. 3 (2022) 100972.

[66] M. Bevilacqua, J. Filippi, A. Lavacchi, A. Marchionni, H.A. Miller, W. Oberhauser, E. Vesselli, F. Vizza, Energy savings in the conversion of $CO_2$ to fuels using an electrolytic device, Energy Technol. 2 (2014) 522–525.

[67] C. Xia, P. Zhu, Q. Jiang, Y. Pan, W.T. Liang, E. Stavitsk, H.N. Alshareef, H.T. Wang, Continuous production of pure liquid fuel solutions via electrocatalytic $CO_2$ reduction using solid-electrolyte devices, Nat. Energy 4 (2019) 776–785.

[68] G. Han, G. Li, Y. Sun, Electrocatalytic dual hydrogenation of organic substrates with a faradaic efficiency approaching 200, Nat. Catal. 6 (2023) 224–233.

[69] E.R. Corson, R. Kas, R. Kostecki, J.J. Urban, W.A. Smith, B.D. McCloskey, R. Kortlever, *In situ* ATR-SEIRAS of carbon dioxide reduction at a plasmonic silver cathode, J. Am. Chem. Soc. 142 (2020) 11750–11762.

[70] W. Shan, R. Liu, H. Zhao, Z. He, Y. Lai, S. Li, G. He, J. Liu, *In situ* surface-enhanced Raman spectroscopic evidence on the origin of selectivity in $CO_2$ electrocatalytic reduction, ACS Nano 14 (2020) 11363–11372.

[71] M. Liu, J. Zhang, H. Su, Y. Jiang, W. Zhou, C. Yang, S. Bo, J. Pan, Q. Liu, *In situ* modulating coordination fields of single-atom cobalt catalyst for enhanced oxygen reduction reaction, Nat. Commun. 15 (2024) 1675.

[72] H. Mistry, Y.W. Choi, A. Bagger, F. Scholten, C.S. Bonifacio, I. Sinev, N.J. Divins, I. Zegkinoglou, H.S. Jeon, K. Kisslinger, E.A. Stach, J.C. Yang, J. Rossmeisl, B. Roldan Cuenya, Enhanced carbon dioxide electroreduction to carbon monoxide over defect-rich plasma-activated silver catalysts, Angew. Chem. Int. Ed. 56 (2017) 11394–11398.

[73] R.G. Mariano, K. McKelvey, H.S. White, M.W. Kanan, Selective increase in $CO_2$ electroreduction activity at grain-boundary surface terminations, Science 358 (2017) 1187–1191.

[74] Y.G. Kim, J.H. Baricuatro, A. Javier, J.M. Gregoire, M.P. Soriaga, The evolution of the polycrystalline copper surface, first to Cu(111) and then to Cu(100), at a fixed $CO_2$RR potential: a study by operando EC-STM, Langmuir 30 (2014) 15053–15056.

[75] G.H. Simon, C.S. Kley, B. Roldan Cuenya, Potential-dependent morphology of copper catalysts during $CO_2$ electroreduction revealed by *in situ* atomic force microscopy, Angew. Chem. Int. Ed. 60 (2021) 2561–2568.

[76] J.J. Velasco-Velez, R.V. Mom, L.E. Sandoval-Diaz, L.J. Falling, C.H. Chuang, D. Gao, T.E. Jones, Q. Zhu, R. Arrigo, B. Roldan Cuenya, A. Knop-Gericke, T. Lunkenbein, R. Schlogl, Revealing the active phase of copper during the electroreduction of $CO_2$ in aqueous electrolyte by correlating *in situ* X-ray spectroscopy and *in situ* electron microscopy, ACS Energy Lett. 5 (2020) 2106–2111.

[77] J. Vavra, T.H. Shen, D. Stoian, V. Tileli, R. Buonsanti, Real-time monitoring reveals dissolution/redeposition mechanism in copper nanocatalysts during the initial stages of the $CO_2$ reduction reaction, Angew. Chem. Int. Ed. 60 (2021) 1347–1354.

[78] H.-J.S. Hao Peng, Zhi-You Zhou, Lin-Fan Shen, Long Huang, Shuo-Hui Cao, Shi-Gang Sun, Design and fabrication of the electrolytic cell with silicon-based boron-doped diamond electrode and its feasibility for in-situ nuclear magnetic resonance study, J. Electrochem. 27 (2021) 332–338.

[79] Y.J. Tong, *In situ* electrochemical nuclear magnetic resonance spectroscopy for electrocatalysis: challenges and prospects, Curr. Opin. Electrochem. 4 (2017) 60–68.

[80] C. Roy, B. Sebok, S.B. Scott, E.M. Fiordaliso, J.E. Sørensen, A. Bodin, D.B. Trimarco, C.D. Damsgaard, P.C.K. Vesborg, O. Hansen, I.E.L. Stephens, J. Kibsgaard, I. Chorkendorff, Impact of nanoparticle size and lattice oxygen on water oxidation on $NiFeO_xH_y$, Nat. Catal. 1 (2018) 820–829.

[81] B. Hasa, M. Jouny, B.H. Ko, B. Xu, F. Jiao, Flow electrolyzer mass spectrometry with a gas-diffusion electrode design, Angew. Chem. Int. Ed. 60 (2021) 3277–3282.

[82] A.J. Wain, M.A. O'Connell, Advances in surface-enhanced vibrational spectroscopy at electrochemical interfaces, Adv. Phys. X 2 (2017) 188–209.

[83] Y. Kim, S. Park, S.-J. Shin, W. Choi, B.K. Min, H. Kim, W. Kim, Y.J. Hwang, Time-resolved observation of C-C coupling intermediates on Cu electrodes for selective electrochemical $CO_2$ reduction, Energy Environ. Sci. 13 (2020) 4301–4311.

[84] Z. Chang, F. Kong, M. Wang, S. Han, X. Cui, H. Tian, Y. Chen, G. Meng, C. Chen, Y. Liu, Y. Huang, J. Shi, Efficient ammonia electrosynthesis by coupling to concurrent methanol oxidation, Chem Catal. 2 (2022) 358–371.

[85] W. Chen, S. Luo, M. Sun, X. Wu, Y. Zhou, Y. Liao, M. Tang, X. Fan, B. Huang, Z. Quan, High-entropy intermetallic PtRhBiSnSb nanoplates for highly efficient alcohol oxidation electrocatalysis, Adv. Mater. 34 (2022) 2206276.

[86] X. Cao, D. Tan, B. Wulan, K.S. Hui, K.N. Hui, J. Zhang, *In situ* characterization for boosting electrocatalytic carbon dioxide reduction, Small Methods 5 (2021) e2100700.

[87] H. An, L. Wu, L.D.B. Mandemaker, S. Yang, J. de Ruiter, J.H.J. Wijten, J.C.L. Janssens, T. Hartman, W. van der Stam, B.M. Weckhuysen, Sub-second time-resolved surface-enhanced Raman spectroscopy reveals dynamic CO intermediates during electrochemical $CO_2$ reduction on copper, Angew. Chem. Int. Ed. 60 (2021) 16576–16584.

[88] Y. Zhang, S.-X. Guo, X. Zhang, A.M. Bond, J. Zhang, Mechanistic understanding of the electrocatalytic $CO_2$ reduction reaction—new developments based on advanced instrumental techniques, Nano Today 31 (2020) 100835.

[89] L. Wang, H. Jin, Z. Liu, S. Yang, G. He, H. Liu, X. Meng, C. Xu, Investigation on the preparation of 5-hydroxymethylfurfural through fructose dehydration using in-line FTIR and in-situ $^{13}C$ NMR, J. Catal. 432 (2024) 115450.

[90] Z. Ma, R. Pathegama Gamage, T. Rathnaweera, L. Kong, Review of application of molecular dynamic simulations in geological high-level radioactive waste disposal, Appl. Clay Sci. 168 (2019) 436–449.

[91] H. Tang, Y. Zhao, S. Shan, X. Yang, D. Liu, F. Cui, B. Xing, Theoretical insight into the adsorption of aromatic compounds on graphene oxide, Environ. Sci.: Nano 5 (2018) 2357–2367.

[92] F. Ma, Z. Li, R. Hu, Z. Wang, J. Wang, J. Li, Y. Nie, Z. Zheng, X. Jiang, Electrocatalytic waste-treating-waste strategy for concurrently upgrading of polyethylene terephthalate plastic and $CO_2$ into value-added formic acid, ACS Catal. 13 (2023) 14163–14172.

[93] W. Gu, M. Yang, Z. Chen, T. Cao, Y. Zhang, Y. Li, R. Zhang, New insights into enhanced electrochemical advanced oxidation mechanism of B-doped graphene aerogel: experiments, molecular dynamics simulations and DFT, J. Hazard Mater. 443 (2023) 130331.

[94] W.L. Jorgensen, D.S. Maxwell, J. Tirado-Rives, Development and testing of the OPLS all-atom force field on conformational energetics and properties of organic liquids, J. Am. Chem. Soc. 118 (1996) 11225–11236.

[95] J. Behler, First principles neural network potentials for reactive simulations of large molecular and condensed systems, Angew. Chem. Int. Ed. 56 (2017) 12828–12840.

[96] J.K. Nørskov, J. Rossmeisl, A. Logadottir, L. Lindqvist, J.R. Kitchin, T. Bligaard, H. Jónsson, Origin of the overpotential for oxygen reduction at a fuel-cell cathode, J. Phys. Chem. B 108 (2004) 17886–17892.

[97] F. Chen, Z.-C. Yao, Z.-H. Lyu, J. Fu, X. Zhang, J.-S. Hu, Recent advances in p-block metal chalcogenide electrocatalysts for high-efficiency $CO_2$ reduction, eScience 4 (2024) 100172.

[98] S. Verma, S. Lu, P.J.A. Kenis, Co-electrolysis of $CO_2$ and glycerol as a pathway to carbon chemicals with improved technoeconomics due to low electricity consumption, Nat. Energy 4 (2019) 466–474.

[99] W. Xi, P. Yang, M. Jiang, X. Wang, H. Zhou, J. Duan, M. Ratova, D. Wu, Electrochemical $CO_2$ reduction coupled with alternative oxidation reactions: electrocatalysts, electrolytes, and electrolyzers, Appl. Catal. B Environ. Energy 341 (2024) 123291.

[100] C. Kang, Y. Li, Y. Xu, C. Ding, H. Chen, J. Zeng, Y. Li, C. Li, J. He, Coupling $CO_2$-to-ethylene reduction with the chlor-alkaline process in seawater through *in situ*-formed Cu catalysts, J. Phys. Chem. Lett. 14 (2023) 2983–2989.

[101] X. Hu, G. Mei, X. Chen, J. Liu, B.Y. Xia, B. You, Simultaneous generation of $H_2O_2$ and formate by co-electrolysis of water and $CO_2$ over bifunctional $Zn/SnO_2$ nanodots, Angew. Chem. Int. Ed. 62 (2023) e202304050.

[102] X. Wei, Y. Li, L. Chen, J. Shi, Formic acid electro-synthesis by concurrent cathodic $CO_2$ reduction and anodic $CH_3OH$ oxidation, Angew. Chem. Int. Ed. 60 (2021) 3148–3155.

[103] D.-D. Ma, S.-G. Han, C. Cao, W. Wei, X. Li, B. Chen, X.-T. Wu, Q.-L. Zhu, Bifunctional single-molecular heterojunction enables completely selective $CO_2$-to-CO conversion integrated with oxidative 3D nano-polymerization, Energy Environ. Sci. 14 (2021) 1544–1552.

[104] J.-H. Guo, W.-Y. Sun, Integrating nickel-nitrogen doped carbon catalyzed $CO_2$ electroreduction with chlor-alkali process for CO, $Cl_2$ and $KHCO_3$ production with enhanced techno-economics, Appl. Catal. B Environ. 275 (2020) 119154.

[105] R. Ge, L.-Y. Dong, X. Hu, Y.-T. Wu, L. He, G.-P. Hao, A.-H. Lu, Intensified coupled electrolysis of $CO_2$ and brine over electrocatalysts with ordered mesoporous transport channels, Chem. Eng. J. 438 (2022) 135500.

[106] F. Quan, G. Zhan, H. Shang, Y. Huang, F. Jia, L. Zhang, Z. Ai, Highly efficient electrochemical conversion of $CO_2$ and NaCl to CO and NaClO, Green Chem. 21 (2019) 3256–3262.

[107] C. Kang, C. Ding, Y. Li, Y. Li, C. Li, J. He, Acidic chloride electrolyte mediates the high conversion ratio of $CO_2$-to-$C_2H_4$ and direct production of $Cl_2$, Sustain. Energy Fuels 8 (2024) 1730–1739.

[108] H. Chen, J. Zeng, Y. Li, C. Kang, C. Ding, Y. Li, C. Li, J. He, Coupling electrochemical $CO_2$ reduction to syngas with chloride-mediated dye degradation to $CO_2$ in a one-compartment cell, Sustain. Energy Fuels 7 (2023) 4533–4539.

[109] S. Mavrikis, M. Nieuwoudt, M. Göltz, S. Ehles, A. Körner, A. Hutzler, E. Fossy, A. Zervas, O. Brai, M. Wegener, F. Doerrfuss, P. Bouwman, S. Rosiwal, L. Wang, C. Ponce de León, Continuous production of ethylene and hydrogen peroxide from paired electrochemical carbon dioxide reduction and water oxidation, Adv. Energy Mater. 14 (2024) 2304247.

[110] W. Ma, H. Wang, W. Yu, X. Wang, Z. Xu, X. Zong, C. Li, Achieving simultaneous $CO_2$ and $H_2S$ conversion via a coupled solar-driven electrochemical approach on non-precious-metal catalysts, Angew. Chem. Int. Ed. 57 (2018) 3473–3477.

[111] E. Pérez-Gallent, S. Turk, R. Latsuzbaia, R. Bhardwaj, A. Anastasopol, F. Sastre-Calabuig, A.C. Garcia, E. Giling, E. Goetheer, Electroreduction of $CO_2$ to CO paired with 1,2-propanediol oxidation to lactic acid. Toward an economically feasible system, Ind. Eng. Chem. Res. 58 (2019) 6195–6202.

[112] G.X. Wang, J.X. Chen, K.K. Li, J.H. Huang, Y.C. Huang, Y.J. Liu, X. Hu, B.S. Zhao, L.C. Yi, T.W. Jones, Z.H. Wen, Cost-effective and durable electrocatalysts for co-electrolysis of $CO_2$ conversion and glycerol upgrading, Nano Energy 92 (2022) 106751.

[113] M.A. Khan, S.K. Nabil, T. Al-Attas, N.G. Yasri, S. Roy, M.M. Rahman, S. Larter, P.M. Ajayan, J. Hu, M.G. Kibria, Zero-crossover electrochemical $CO_2$ reduction to ethylene with co-production of valuable chemicals, Chem Catal. 2 (2022) 2077–2095.

[114] C. Cao, D.D. Ma, J. Jia, Q. Xu, X.T. Wu, Q.L. Zhu, Divergent paths, same goal: a pair-electrosynthesis tactic for cost-efficient and exclusive formate production by metal-organic-framework-derived 2D electrocatalysts, Adv. Mater. 33 (2021) 2008631.

[115] Y. Zhou, Z. Wang, W. Fang, R. Qi, Z. Wang, C. Xia, K. Lei, B. You, X. Yang, Y. Liu, W. Guo, Y. Su, S. Ding, B.Y. Xia, Modulating O-H activation of methanol oxidation on nickel-organic frameworks for overall $CO_2$ electrolysis, ACS Catal. 13 (2023) 2039–2046.

[116] M.S.E. Houache, R. Safari, U.O. Nwabara, T. Rafaïdeen, G.A. Botton, P.J.A. Kenis, S. Baranton, C. Coutanceau, E.A. Baranova, Selective electrooxidation of glycerol to formic acid over carbon supported $Ni_{1-x}M_x$ (M = Bi, Pd, and Au) nanocatalysts and coelectrolysis of $CO_2$, ACS Appl. Energy Mater. 3 (2020) 8725–8738.

[117] J.R.C. Junqueira, D. Das, A. Cathrin Brix, S. Dieckhofer, J. Weidner, X. Wang, J. Shi, W. Schuhmann, Simultaneous anodic and cathodic formate production in a paired electrolyzer by $CO_2$ reduction and glycerol oxidation, ChemSusChem 16 (2023) e202202349.
[118] K. Fernández-Caso, A. Peña-Rodríguez, J. Solla-Gullón, V. Montiel, G. Díaz-Sainz, M. Alvarez-Guerra, A. Irabien, Continuous carbon dioxide electroreduction to formate coupled with the single-pass glycerol oxidation to high value-added products, J. $CO_2$ Util. 70 (2023) 102431.
[119] Y. Zhang, J. Lan, F. Xie, M. Peng, J. Liu, T.S. Chan, Y. Tan, Aligned InS nanorods for efficient electrocatalytic carbon dioxide reduction, ACS Appl. Mater. Interfaces 14 (2022) 25257–25266.
[120] X. Li, Q. Chen, W. Sun, C. He, Z. Wen, Electron-efficient co-electrosynthesis of formates from $CO_2$ and methanol feedstocks, Angew. Chem. Int. Ed. (2024) e202412410.
[121] Y. Li, C.-Z. Huo, H.-J. Wang, Z.-X. Ye, P.-P. Luo, X.-X. Cao, T.-B. Lu, Coupling $CO_2$ reduction with $CH_3OH$ oxidation for efficient electrosynthesis of formate on hierarchical bifunctional CuSn alloy, Nano Energy 98 (2022) 107277.
[122] M. Zhang, J.P. Liao, R.H. Li, S.N. Sun, M. Lu, L.Z. Dong, P. Huang, S.L. Li, Y.P. Cai, Y.Q. Lan, Green synthesis of bifunctional phthalocyanine-porphyrin COFs in water for efficient electrocatalytic $CO_2$ reduction coupled with methanol oxidation, Natl. Sci. Rev. 10 (2023) nwad226.
[123] J. Wang, X. Li, M. Wang, T. Zhang, X. Chai, J. Lu, T. Wang, Y. Zhao, D. Ma, Electrocatalytic valorization of poly(ethylene terephthalate) plastic and $CO_2$ for simultaneous production of formic acid, ACS Catal. 12 (2022) 6722–6728.
[124] S.K. Kilaparthi, A. Addad, A. Barras, S. Szunerits, R. Boukherroub, Simultaneous upcycling of PET plastic waste and $CO_2$ reduction through co-electrolysis: a novel approach for integrating $CO_2$ reduction and PET hydrolysate oxidation, J. Mater. Chem. A 11 (2023) 26075–26085.
[125] L. Guo, X. Zhang, L. Gan, L. Pan, C. Shi, Z.F. Huang, X. Zhang, J.J. Zou, Advances in selective electrochemical oxidation of 5-hydroxymethylfurfural to produce high-value chemicals, Adv. Sci. 10 (2023) e2205540.
[126] Y. Xie, Z. Zhou, N. Yang, G. Zhao, An overall reaction integrated with highly selective oxidation of 5-hydroxymethylfurfural and efficient hydrogen evolution, Adv. Funct. Mater. 31 (2021) 2102886.
[127] Z.-W. Yang, J.-M. Chen, L.-Q. Qiu, W.-J. Xie, L.-N. He, Solar energy-driven electrolysis with molecular catalysts for the reduction of carbon dioxide coupled with the oxidation of 5-hydroxymethylfurfural, Catal. Sci. Technol. 12 (2022) 5495–5500.
[128] S. Choi, M. Balamurugan, K.G. Lee, K.H. Cho, S. Park, H. Seo, K.T. Nam, Mechanistic investigation of biomass oxidation using nickel oxide nanoparticles in a $CO_2$-saturated electrolyte for paired electrolysis, J. Phys. Chem. Lett. 11 (2020) 2941–2948.
[129] R. Lin, H. Yang, H. Zheng, M. Salehi, A. Farzi, P. Patel, X. Wang, J. Guo, K. Liu, Z. Gao, X. Li, A. Seifitokaldani, Efficient integration of carbon dioxide reduction and 5-hydroxymethylfurfural oxidation at high current density, RSC Sustain. 2 (2024) 445–458.
[130] J. Ren, Z. Li, C. Ning, S. Li, L. Zhang, H. Huang, L. Zheng, Y.S. Kang, M. Luo, Y. Zhao, High-efficient electrocatalytic $CO_2$ reduction to HCOOH coupling with 5-hydroxymethylfurfural oxidation using flow cell, AIChE J. (2024) e18562.
[131] S.-Q. Liu, M.-R. Gao, S. Wu, R. Feng, Y. Wang, L. Cui, Y. Guo, X.-Z. Fu, J.-L. Luo, A coupled electrocatalytic system with reduced energy input for $CO_2$ reduction and biomass valorization, Energy Environ. Sci. 16 (2023) 5305–5314.
[132] Z. Zhang, S. Liu, Z. Wu, X. Chen, J. Wang, Y. Gao, S. Wang, F. Tao, G. Lv, High efficiency coupled electrocatalytic $CO_2$ reduction to $C_2H_4$ with 5-hydroxymethylfurfural oxidation over Cu-based nanoflower electrocatalysts, Green Chem. 25 (2023) 5404–5415.
[133] X. Lv, J. Liu, T. Shao, M. Ye, S. Liu, Efficient and cost-effective electrocatalytic $CO_2$ to CO reduction over Sn-modified Cu nanowires by pairing with selective HCHO to HCOOH oxidation, Catal. Today 420 (2023) 114188.
[134] Y. Liang, W. Zhou, Y. Shi, C. Liu, B. Zhang, Unveiling *in situ* evolved $In/In_2O_{3-x}$ heterostructure as the active phase of $In_2O_3$ toward efficient electroreduction of $CO_2$ to formate, Sci. Bull. 65 (2020) 1547–1554.
[135] C. Guo, P. He, R. Cui, Q. Shen, N. Yang, G. Zhao, Electrochemical $CO_2$ reduction using electrons generated from photoelectrocatalytic phenol oxidation, Adv. Energy Mater. 9 (2019) 1900364.
[136] Z.-H. Zhu, Z.-L. Liang, S.-L. Hou, Y. Xie, Y. Ma, Y. Zhang, B. Zhao, Efficient $CO_2$ electroreduction coupled with semi-dehydrogenation of tetrahydroisoquinoline by MOFs modified electrodes, J. Energy Chem. 63 (2021) 328–335.
[137] Y.C. He, D.D. Ma, S.H. Zhou, M. Zhang, J.J. Tian, Q.L. Zhu, Integrated 3D open network of interconnected bismuthene arrays for energy-efficient and electrosynthesis-assisted electrocatalytic $CO_2$ reduction, Small 18 (2022) 2105246.
[138] S.N. Sun, L.Z. Dong, J.R. Li, J.W. Shi, J. Liu, Y.R. Wang, Q. Huang, Y.Q. Lan, Redox-active crystalline coordination catalyst for hybrid electrocatalytic methanol oxidation and $CO_2$ reduction, Angew. Chem. Int. Ed. 61 (2022) e202207282.
[139] Y. Xu, Y. Guo, Y. Sheng, Q. Zhou, H. Yu, K. Deng, Z. Wang, H. Wang, L. Wang, Controlled boron incorporation tuned two-phase interfaces and Lewis acid sites in bismuth nanosheets for driving $CO_2$ electroreduction to formate, J. Mater. Chem. A 11 (2023) 18434–18440.
[140] H. Yadegari, A. Ozden, T. Alkayyali, V. Soni, A. Thevenon, A. Rosas-Hernández, T. Agapie, J.C. Peters, E.H. Sargent, D. Sinton, Glycerol oxidation pairs with carbon monoxide reduction for low-voltage generation of $C_2$ and $C_3$ product streams, ACS Energy Lett. 6 (2021) 3538–3544.
[141] J.E. Huang, F. Li, A. Ozden, A. Sedighian Rasouli, F.P. Garcia de Arquer, S. Liu, S. Zhang, M. Luo, X. Wang, Y. Lum, Y. Xu, K. Bertens, R.K. Miao, C.T. Dinh, D. Sinton, E.H. Sargent, $CO_2$ electrolysis to multicarbon products in strong acid, Science 372 (2021) 1074–1078.
[142] W. Pan, P. Wang, L. Fan, K. Chen, L. Yi, J. Huang, P. Cai, X. Liu, Q. Chen, G. Wang, Z. Wen, Cu-Ni alloy decorating N-doped carbon nanosheets toward high-performance electrocatalysis of mildly acidic $CO_2$ reduction, Inorg. Chem. Front. 10 (2023) 2276–2284.
[143] T. Hibino, K. Kobayashi, M. Nagao, Z. Dongwen, C. Siyuan, Two-stage electrolysis of $H_2O$ and $CO_2$ to methanol: $CO_2$-to-methane reduction at the cathode and subsequent methane-to-methanol oxidation at the anode, J. Mater. Chem. A 10 (2022) 22718–22729.
[144] M. Dan, R. Zhong, S. Hu, H. Wu, Y. Zhou, Z.-Q. Liu, Strategies and challenges on selective electrochemical hydrogen peroxide production: catalyst and reaction medium design, Chem Catal. 2 (2022) 1919–1960.
[145] J. Qi, Y. Du, Q. Yang, N. Jiang, J. Li, Y. Ma, Y. Ma, X. Zhao, J. Qiu, Energy-saving and product-oriented hydrogen peroxide electrosynthesis enabled by electrochemistry pairing and product engineering, Nat. Commun. 14 (2023) 6263.
[146] H. Xu, S. Zhang, X. Zhang, M. Xu, M. Han, L.R. Zheng, Y. Zhang, G. Wang, H. Zhang, H. Zhao, Atomically dispersed iron regulating electronic structure of iron atom clusters for electrocatalytic $H_2O_2$ production and biomass upgrading, Angew. Chem. Int. Ed. 62 (2023) e202314414.
[147] M.A. Hoque, J.B. Gerken, S.S. Stahl, Synthetic dioxygenase reactivity by pairing electrochemical oxygen reduction and water oxidation, Science 383 (2024) 173–178.
[148] K. Dong, J. Liang, Y. Wang, Y. Ren, Z. Xu, H. Zhou, L. Li, Q. Liu, Y. Luo, T. Li, A.M. Asiri, Q. Li, D. Ma, X. Sun, Plasma-induced defective $TiO_{2-x}$ with oxygen vacancies: a high-active and robust bifunctional catalyst toward $H_2O_2$ electrosynthesis, Chem Catal. 1 (2021) 1437–1448.
[149] M. Cheng, Z. Li, T. Xu, Y. Mao, Y. Zhang, G. Zhang, Z. Yan, Efficient overall $2e^-$ oxygen electrolysis to $H_2O_2$ on $CeO_2$ nanocubes, Electrochim. Acta 430 (2022) 141091.
[150] S. Kumar, Y.-P. Fu, Dual morphology $ZnCo_2O_4$ coupled graphitic carbon nitride: an efficient electro-catalyst for electrochemical $H_2O_2$ production and methanol oxidation reaction, Electrochim. Acta 447 (2023) 142161.
[151] X. Li, L. Cong, H. Lin, F. Liu, X. Fu, H.-C. Xu, N. Lin, Linear paired electrolysis of furfural to furoic acid at both anode and cathode in a multiple redox mediated system, Green Energy Environ. 9 (2024) 104–113.
[152] D. Fu, Y. Zhu, T. Yu, J. Li, L. Chen, Y. Cui, Z. Liu, H. Wang, In-situ efficient electrosynthesis of $H_2O_2$-NaClO based on the media pH and catalyst mutual selection mechanism, J. Power Sources 553 (2023) 232306.
[153] Q. Zhang, C. Cao, S. Zhou, W. Wei, X. Chen, R. Xu, X.-T. Wu, Q.-L. Zhu, Bifunctional oxygen-defect bismuth catalyst toward concerted production of $H_2O_2$ with over 150% cell faradaic efficiency in continuously flowing paired-electrosynthesis system, Adv. Mater. 36 (2024) 2408341.
[154] L. Wang, M. Xia, H. Wang, K. Huang, C. Qian, C.T. Maravelias, G.A. Ozin, Greening ammonia toward the solar ammonia refinery, Joule 2 (2018) 1055–1074.
[155] D.E. Canfield, A.N. Glazer, P.G. Falkowski, The evolution and future of earth's nitrogen cycle, Science 330 (2010) 192–196.
[156] J. Bai, H. Huang, F.-M. Li, Y. Zhao, P. Chen, P.-J. Jin, S.-N. Li, H.-C. Yao, J.-H. Zeng, Y. Chen, Glycerol oxidation assisted electrocatalytic nitrogen reduction: ammonia and glyceraldehyde co-production on bimetallic RhCu ultrathin nanoflake nanoaggregates, J. Mater. Chem. A 7 (2019) 21149–21156.
[157] D. Gupta, A. Kafle, T.C. Nagaiah, Dinitrogen reduction coupled with methanol oxidation for low overpotential electrochemical $NH_3$ synthesis over cobalt pyrophosphate as bifunctional catalyst, Small 19 (2023) e2208272.
[158] G.-R. Xu, M. Batmunkh, S. Donne, H. Jin, J.-X. Jiang, Y. Chen, T. Ma, Ruthenium(iii) polyethyleneimine complexes for bifunctional ammonia production and biomass upgrading, J. Mater. Chem. A 7 (2019) 25433–25440.
[159] L. Zhao, X. Kuang, C. Chen, X. Sun, Z. Wang, Q. Wei, Boosting electrocatalytic nitrogen fixation via energy-efficient anodic oxidation of sodium gluconate, Chem. Commun. 55 (2019) 10170–10173.
[160] J. Liang, Q. Liu, A.A. Alshehri, X. Sun, Recent advances in nanostructured heterogeneous catalysts for N-cycle electrocatalysis, Nano Res. Energy 1 (2022) e9120010.
[161] T. Ren, Z. Yu, H. Yu, K. Deng, Z. Wang, X. Li, H. Wang, L. Wang, Y. Xu, Sustainable ammonia electrosynthesis from nitrate wastewater coupled to electrocatalytic upcycling of polyethylene terephthalate plastic waste, ACS Nano 17 (2023) 12422–12432.
[162] Y. Wang, C. Wang, M. Li, Y. Yu, B. Zhang, Nitrate electroreduction: mechanism insight, *in situ* characterization, performance evaluation, and challenges, Chem. Soc. Rev. 50 (2021) 6720–6733.
[163] F.-Y. Chen, Z.-Y. Wu, S. Gupta, D.J. Rivera, S.V. Lambeets, S. Pecaut, J.Y.T. Kim, P. Zhu, Y.Z. Finfrock, D.M. Meira, G. King, G. Gao, W. Xu, D.A. Cullen, H. Zhou, Y. Han, D.E. Perea, C.L. Muhich, H. Wang, Efficient conversion of low-concentration nitrate sources into ammonia on a Ru-dispersed Cu nanowire electrocatalyst, Nat. Nanotechnol. 17 (2022) 759.
[164] T. Ren, H. Wang, S. Xu, H. Yu, K. Deng, Z. Wang, H. Wang, L. Wang, Y. Xu, Coupling post-modification with reconstruction over Co-based metal-organic frameworks for electrochemical collective value-added recycling of nitrate and sulfion in wastewater, J. Mater. Chem. A 11 (2023) 24854–24860.
[165] T. Ren, Z. Duan, H. Wang, H. Yu, K. Deng, Z. Wang, H. Wang, L. Wang, Y. Xu, Electrochemical co-production of ammonia and biodegradable polymer monomer glycolic acid via the co-electrolysis of nitrate wastewater and waste plastic, ACS Catal. 13 (2023) 10394–10404.
[166] Y. Wang, C. Liu, B. Zhang, Y. Yu, Self-template synthesis of hierarchically structured $Co_3O_4$@NiO bifunctional electrodes for selective nitrate reduction and

tetrahydroisoquinolines semi-dehydrogenation, Sci. China Mater. 63 (2020) 2530–2538.
[167] X.H. Wang, Q.L. Hong, L.Y. Shao, Q.G. Zhai, Y.C. Jiang, X. Ai, Y. Chen, S.N. Li, Copper-nickel oxide nanosheets with atomic thickness for high-efficiency sulfur ion electrooxidation assisted nitrate electroreduction to ammonia, Adv. Funct. Mater. (2024) 2408834.
[168] W. Lv, D. Ruan, X. Zheng, L. Li, H. Cao, Z. Wang, Y. Zhang, Z. Sun, One-step recovery of valuable metals from spent lithium-ion batteries and synthesis of persulfate through paired electrolysis, Chem. Eng. J. 421 (2021) 129908.
[169] L. Zhao, Z. Lv, Y. Shi, S. Zhou, Y. Liu, J. Han, Q. Zhang, J. Lai, L. Wang, Simultaneous generation of furfuryl alcohol, formate, and $H_2$ by co-electrolysis of furfuryl and HCHO over bifunctional CuAg bimetallic electrocatalysts at ultra-low voltage, Energy Environ. Sci. 17 (2024) 770–779.
[170] X.H. Chadderdon, D.J. Chadderdon, T. Pfennig, B.H. Shanks, W. Li, Paired electrocatalytic hydrogenation and oxidation of 5-(hydroxymethyl)furfural for efficient production of biomass-derived monomers, Green Chem. 21 (2019) 6210–6219.
[171] S. Li, X. Sun, Z. Yao, X. Zhong, Y. Cao, Y. Liang, Z. Wei, S. Deng, G. Zhuang, X. Li, J. Wang, Biomass valorization via paired electrosynthesis over vanadium nitride-based electrocatalysts, Adv. Funct. Mater. 29 (2019) 1904780.
[172] H. Liu, T.-H. Lee, Y. Chen, E.W. Cochran, W. Li, Paired electrolysis of 5-(hydroxymethyl)furfural in flow cells with a high-performance oxide-derived silver cathode, Green Chem. 23 (2021) 5056–5063.
[173] X. Guo, H. Fu, J. Yang, L. Luo, H. Zhou, M. Xu, X. Kong, M. Shao, H. Duan, Z. Li, Promoting electrocatalytic hydrogenation of 5-hydroxymethylfurfural over a cooperative Ag/$SnO_2$ catalyst in a wide potential window, ACS Catal. 13 (2023) 13528–13539.
[174] X. Pan, S. Mei, W.-J. Liu, Self-supported ultrathin $Co_3O_4$ nanoarray enabling efficient paired electrolysis of 5-hydroxymethylfurfural for simultaneous dihydroxymethylfuran (DHMF) and furandicarboxylic acid (FDCA) production, Chin. Chem. Lett. 34 (2023) 108034.
[175] P. Zhang, X. Sheng, X. Chen, Z. Fang, J. Jiang, M. Wang, F. Li, L. Fan, Y. Ren, B. Zhang, B.J.J. Timmer, M.S.G. Ahlquist, L. Sun, Paired electrocatalytic oxygenation and hydrogenation of organic substrates with water as the oxygen and hydrogen source, Angew. Chem. Int. Ed. 58 (2019) 9155–9159.
[176] X. Pang, H. Bai, H. Zhao, W. Fan, W. Shi, Efficient electrocatalytic oxidation of 5-hydroxymethylfurfural coupled with 4-nitrophenol hydrogenation in a water system, ACS Catal. 12 (2022) 1545–1557.
[177] J. Ren, J. Wang, Z. Li, C. Ning, W. Cao, S. Li, G.I.N. Waterhouse, L. Zheng, D. O'Hare, Y. Zhao, Electrocatalytic hydrogenation coupling oxidation using water in a highly efficient paired cell enabled by an oxygen defect-rich layered double hydroxide, J. Mater. Chem. A 12 (2024) 4333–4342.
[178] Y. Zhao, T. Xu, X. Bai, Y. Jia, Y. Pan, X. Shi, H. Zheng, L. Zheng, Selective electrochemical hydrogenation of nitrobenzene to aniline coupled with efficient 5-hydroxymethylfurfural oxidation in aqueous electrolyte using a broccoli-like CuNi catalyst, Chem. Eng. J. 482 (2024) 149054.
[179] W. Gong, X. Mao, J. Zhang, Y. Lin, H. Zhang, A. Du, Y. Xiong, H. Zhao, Ni-Co alloy nanoparticles catalyze selective electrochemical coupling of nitroarenes into azoxybenzene compounds in aqueous electrolyte, ACS Nano 17 (2023) 3984–3995.
[180] X. Chong, C. Liu, Y. Huang, C. Huang, B. Zhang, Potential-tuned selective electrosynthesis of azoxy-, azo- and amino-aromatics over a CoP nanosheet cathode, Natl. Sci. Rev. 7 (2020) 285–295.
[181] W. Qiao, I. Waseem, G. Shang, D. Wang, Y. Li, F. Besenbacher, H. Niemantsverdriet, C. Yan, R. Su, Paired electrochemical N-N coupling employing a surface-hydroxylated $Ni_3$Fe-MOF-OH bifunctional electrocatalyst with enhanced adsorption of nitroarenes and anilines, ACS Catal. 11 (2021) 13510–13518.
[182] G. Gan, X. Li, S. Fan, Z. Yin, L. Wang, G. Chen, Ultrathin Fe-N-C single-atom catalysts with bifunctional active site for simultaneous production of ethylene and aromatic chlorides, Nano Energy 80 (2021) 105532.
[183] Y. Qi, B. Liu, X. Qiu, X. Zeng, Z. Luo, W. Wu, Y. Liu, L. Chen, X. Zu, H. Dong, X. Lin, Y. Qin, Simultaneous oxidative cleavage of lignin and reduction of furfural via efficient electrocatalysis by P-doped $CoMoO_4$, Adv. Mater. 35 (2023) e2208284.
[184] B. Zhou, K. Shi, X. Teng, Z. Li, L. Chen, J. Shi, Membrane-free electrocatalytic co-conversions of PBS waste plastics and maleic acid into high-purity succinic acid solid, Angew. Chem. Int. Ed. 63 (2024) e202411502.